UC San Diego
UC San Diego Electronic Theses and Dissertations

Title

Bright Coherent EUV and X-ray Light driven by UV and Visible Lasers and Attosecond-to-femtosecond Electron-Electron Correlation Spectroscopy and Recombination Physics

Permalink

https://escholarship.org/uc/item/0b02c2t4

Author

Wang, Siyang

Publication Date

2023

Peer reviewed|Thesis/dissertation

eScholarship.org Powered by the California Digital Library
University of California

UNIVERSITY OF CALIFORNIA SAN DIEGO

Bright Coherent EUV and X-ray Light driven by UV and Visible Lasers and Attosecond-to-femtosecond Electron-Electron Correlation Spectroscopy and Recombination Physics

A dissertation submitted in partial satisfaction of the
requirements for the degree Doctor of Philosophy

in

Physics

by

Siyang Wang

Committee in charge:

Professor Tenio Popmintchev, Chair
Professor Richard Averitt
Professor Eric E. Fullerton
Professor Oleg Shpyrko

2023

Copyright

Siyang Wang, 2023

All rights reserved.

The dissertation of Siyang Wang is approved, and it is acceptable in quality and form for publication on microfilm and electronically.

University of California San Diego

2023

DEDICATION

I dedicate my dissertation work to my wife who always supports me and encourages me at the most challenging time. I cannot persist without my wife.

I also dedicate this dissertation to my parents and my friends who offer me mental support and partial sponsorship.

I dedicate this work and give special thanks to our younger graduate student Jerry Yan for helping and discussing with me that truly save tons of my time and make me feel not lonely in research.

EPIGRAPH

Life is like riding a bicycle. To keep your balance, you must keep moving.

Albert Einstein

TABLE OF CONTENTS

Dissertation Approval Page iii

Dedication iv

Epigraph v

Table of Contents vi

List of Figures ix

List of Tables xiv

Acknowledgements xv

Vita xvi

Abstract of the Dissertation xvii

Chapter 1 Introduction - fully coherent High order Harmonics generation 1
  1.1 Discovery of High Harmonic Generation using 248 nm lasers 1
    1.1.1 Extreme Nonlinear Optics Regime 1
    1.1.2 Coherent and incoherent short-wavelength Extreme Ultraviolet and X-ray light source 4
  1.2 Advantages of High Harmonic EUV and X-ray light 7
    1.2.1 Full spatial coherence 7
    1.2.2 Temporal coherence 7
    1.2.3 Attosecond and femtosecond spectroscopic and imaging Applications 9

Chapter 2 Quantum and Extreme Nonlinear Optics Design of Coherent EUV and X-ray Light 12
  2.1 Microscopic physical understanding/ Physical Model 12
    2.1.1 Full Quantum model 12
    2.1.2 Semi-classical simple-man rescattering model 12
    2.1.3 Lewenstein model - Strong field approximation(SFA) 20
    2.1.4 SFA+: marriage of SFA and TDSE 22
    2.1.5 Generation of coherent X-ray using short and long wavelength driven laser 22
  2.2 Macroscopic Physical picture 23
    2.2.1 Phase Matching of High Harmonic Generation 23
    2.2.2 Phase Matching of High Harmonics using Ti: Sapphire laser driver 28
    2.2.3 Quasi-phase matching using periodic physical structures and all-optical light structures 28

2.2.4 Effective phase matching in the Soft and Hard X-ray regime in multiply charged plasma using Visible and UV driving lasers 32

Chapter 3 Advance technology: design of ultrafast infrared/visible/UV laser parameters for efficient X-ray generation 35
3.1 Self Phase Modulation of infrared laser pulses in revolver-type anti-resonant fiber for the first time. 35
3.2 Self Phase Modulation of visible laser pulses in the thin plate/periodic Kerr medium 37
3.2.1 Abstract 37
3.2.2 Introduction 39
3.3 Spectral Broadening in Low Nonlinearity Multi-Plate Geometry 40
3.4 High-Performance Laser Pulse Compression with Enhanced Spatial and Temporal Quality 43
3.5 Ultrabright High Harmonic Generation Using Short-Pulse Short-Wavelength UV-VIS Lasers 48
3.6 Conclusion 50

Chapter 4 Bright Coherent X-ray Generation Designs and High-Performance Spectrometer and Monochromator for EUV and X-ray Attosecond Pulses 51
4.1 Lego Hollow Waveguide Designs for Phase-Matching of Extreme High Harmonic Generation 51
4.2 Lego Design of X-ray Toroidal Mirror Focusing Optics 57
4.3 Lego Design of Conical Diffraction Grating Geometry - in Reflection Mode . . . 58
4.4 Lego Design of Transmission Diffraction Grating Geometry 60
4.5 Modular Beamline Design 62

Chapter 5 First Coherent EUV - Soft X-ray Light with Continuous Red and Blue Wavelength Tunability 64
5.1 Initial Idea 64
5.2 Abstract. 65
5.3 Introduction 65
5.4 Wavelength-tunable, ultrafast, coherent X-ray light. 66
5.5 Conclusion 73

Chapter 6 Extending Bright Coherent EUV High Harmonic Emission into the X-ray Regime Using 400 nm Driving Laser 77
6.1 Experimental Setup 77
6.2 Ultrabright harmonic signal in EUV Regime 79
6.3 Phase Matching Bahavior 81
6.4 Reaching Ultra-High Peak Intensity 82

Chapter 7 Surprise in Electron-Electron Correlations - Ionization and Recombination Effects 86

7.1 Discovery of Secondary High Harmonic Plateau 86
7.2 Attosecond Electron Double-Recombination in Helium 88
7.3 Attosecond Electron-Electron Correlations in Helium 90
7.4 Outlook 91

Appendix A Ionization potential of noble gases 97

Appendix B Atomic Unit Conversion 98

Appendix C Conical Grating Efficiency Simulation 99

Bibliography 101

LIST OF FIGURES

Figure 1.1. Perturbative versus non-perturbative nonlinear process 3

Figure 1.2. Top: Peak brightness of coherent HH X-ray sources compared with FEL and synchrotron sources. Bottom: Peak Power comparison.(The circles represent different driving laser photon energy from 0.32eV to 4.6eV). Graph from Dimitar Popmintchev. 6

Figure 1.3. **Double-slit diffraction at different HH energy** A) HH energy at 93eV driven by 270nm laser. B) HH energy at 45eV driven by 800nm laser. Graph from Dimitar Popmintchev. 8

Figure 1.4. Interferece fringes within a single harmonic in the far field. The fringes follow the patterns of harmonics. The image shows high harmonics with conical diffraction order which will be explained in Chapter 4 and 6. 9

Figure 2.1. Schematics of the semi-classical simple-man rescattering process.Graph from Tenio Popmintchev. 14

Figure 2.2. Top: ADK rate coupled with the population of neutral atoms and ions. Bottom: ADK rate in terms of time. 17

Figure 2.3. Population and ion species change over time. The total number of atom and ions remain constant. Top: log-scale. Bottom: linear scale. 18

Figure 2.4. Free electron's trajectory over time affected by the laser electric field($\lambda_L =$ 800nm) as a function of initial ionization phase $\phi_0 = \omega_L t_b$ where t_b is the 'born time' of the free-electron. 19

Figure 2.5. 1-D displacement vs. Kinetic Energy 20

Figure 2.6. A) Normalized HH intensity as a function of L with different L_{coh}/L_{abs} ratio. B) 2D normalized intensity map in normalized coordinates L_{coh}/L_{abs} and L/L_{abs}. Graph from Dimitar Popmintchev. 26

Figure 2.7. A) When the HHG is phase-matched, the HH signal grows linearly with the medium length theoretically. (B) Without phase-matching, the HH signal periodically oscillates on the scale of one coherence length. Graph from Tenio Popmintchev 29

Figure 2.8. All-optical grating-assisted quasi-phase matching approach 30

Figure 2.9. Mechanical solution, modulated waveguide. 31

Figure 2.10. Series of gasjets. 31

Figure 2.11. Counter-propagatig pulse train. 33

Figure 2.12. Index of refraction for HH phase-matching 34

Figure 3.1. SEM image of antiresonant fiber. 36

Figure 3.2. Single stage laser pulse compression using air-filled antiresonant fiber and prism pair compressor. 37

Figure 3.3. Spectral phase modulation of different laser pulse energy after propagation in an 11cm long antiresonant fiber. The Fourier transform-limited pulse duration of the broadest spectrum goes down to 56fs. The laser is initially with a pulse duration of 250 fs. 37

Figure 3.4. The SHG-FROG trace shows typical signs of compression. 38

Figure 3.5. Schematic of a single-stage spectral broadening and compression of ultrafast VIS 515 nm laser pulses using thin plates with low nonlinearity. 44

Figure 3.6. Spectral broadening through nonlinear spectral phase modulation after plates. Top: wavelength domain. Bottom: frequency domain. This is the first effective spectral broadening for visible laser light. 45

Figure 3.7. Fourier Transform Limited (FTL) pulse duration after each plate. Accumulated nonlinear phase and corresponding B-integral after each plate. Here we simulate the case of periodic soliton mode with $b = 1$. 46

Figure 3.8. FROG measurement of the compressed pulse. A and C: SHG-FROG measurement. B and D: SD-FROG measurement. For the first time, we were able to use this method to compress pulsed visible laser to be 4.5 times shorter. 47

Figure 3.9. Theoretical high harmonic cutoffs at the technologically relevant 13.5 nm EUV wavelength (91.7 eV) for a 515 nm driver with a 40 fs pulse duration for an experimentally feasible peak intensity of 1.0×10^{15} W/cm^2 (ionization of Ar ions in blue and neutral He gas in red). 49

Figure 4.1. Transmission(blue curve) for the HE$_{11}$ mode and effective mode index(red curve) of typical silicon-dioxide hollow core waveguide with radius of 200μm. Graph from Dimitar Popmintchev. 52

Figure 4.2. Melt or Vaporization dominated process. 53

Figure 4.3. The optical principle of helical drilling. 54

Figure 4.4. The ultrafast machining stage set-up. 55

Figure 4.5. Ultrafast drilling test on fiber. 56

Figure 4.6. Pre-drilled hollow core fiber for high harmonic gasjet design. 57

Figure 4.7. Left: The mounting of the toroidal mirror provides 5 degrees of freedom. Which enables the tuning of the refocusing image to be with minimum aberration. Right: the refocus of the fundamental light on the camera. . . . 58

Figure 4.8. Conical grating efficiency for the first and second diffraction order of grating with 500l/mm(Top) and 1200l/mm(Bottom). 59

Figure 4.9. Conical diffraction geometry. Spherical coordinates are used here. γ is defined by the angle between the incoming ray and the grating ruling. α and β are the azimuth angle of the incoming and diffracted light. 60

Figure 4.10. Nanostructure transmission gratings on a chip with different groove densities from 500l/mm to 10000l/mm. 61

Figure 4.11. Cross section of the transmission grating. 61

Figure 4.12. SEM image of nanostructure transmission gratings with 10k lines/mm. . . . 61

Figure 4.13. Modern compact modular beamline with reflective grating configuration. The full beamline is with a length of less than three meters. 63

Figure 5.1. Experimental setup of pulse compression and generation of tunable VIS driving laser light at 480-550 nm. 67

Figure 5.2. Ultrafast, tunable VIS driving laser light. Large range tunable second-harmonic spectra with central wavelengths in the 480 – 580 nm spectral range, optimized for high energy and record short second-harmonic pulse durations, ideal for efficient HHG generation. 69

Figure 5.3. Continuously wavelength-tunable EUV – X-ray high harmonics from He atoms, generated by a tunable VIS driving laser with wavelengths spanning the broad range of 480 - 550nm. Blue-shift and red-shift wavelength-tunable EUV harmonics. 70

Figure 5.4. **Second harmonic peak intensity optimization of the VIS driving laser light.** Neural network optimization of flat wavefront second harmonic beam showing an optimal spatio-temporal intensity distribution at the focus. 72

Figure 5.5. Predicted high harmonic full phase matching and effective phase matching emission as a function of the driving laser wavelength in the VIS and UV regions. 75

Figure 5.6. Continuously wavelength-tunable EUV – X-ray high harmonics from He atoms, generated by a tunable VIS driving laser with wavelengths spanning the broad range of 480-550 nm. 76

Figure 6.1. The 400nm laser driving High Harmonic Beamline Setup 78

Figure 6.2. Self-diffraction frequency-resolved optical gating(SD-FROG) measurement of the 400 nm driving laser. The pulse duration can be down to 28 fs. 79

Figure 6.3. **High Harmonic Spectrum from argon and helium** Top: HH spectrum from helium and argon with a linear scale.Bottom: HH spectrum from helium and argon with a log scale. The conventional cutoff is more t than 140 eV. The HH is optimized at 31st harmonics with 13 nm in Helium. . . . 80

Figure 6.4. **Calculated photon flux at the source.** The harmonic photon per harmonic is able to reach 10^{10} photons/eV/s for 15^{th} and 17^{th} harmonic with corresponding photon energy of 46.5eV and 52.7eV. 81

Figure 6.5. **HH gas pressure scan with Ar and Al filters.** The pressure scan shows that phase-matching favors low gas pressure. 82

Figure 6.6. **HH gas pressure scan with Ar.** High-resolution pressure scan with 1W and 2W of driving laser power. Using a combination of aluminum and zirconium filters. This shows a weak expected tendency that higher-order harmonic favors high pressure. 82

Figure 6.7. HH gas pressure scan with Ar and He 83

Figure 6.8. Driving laser power scan. 85

Figure 7.1. **Image of a conical pattern of HH spectrum** Top: Image from argon gas that shows a clear cutoff. The dashed arrow is the direction of higher harmonic order with higher harmonic photon energy. Bottom: Image from helium with an extended secondary plateau. 87

Figure 7.2. **Linear relationship with conventional single recombination cutoff and secondary cutoff.** Experimental data were consistent with the secondary cutoff predicted by the DER cutoff with the scaling of $5.5U_p$ 89

Figure 7.3. Classical trajectory and combined cutoff photon energy of DER process. . 90

Figure 7.4. **HH spectrum with the secondary cutoff from DER.** The conventional single electron cutoff is around 120 eV with harmonic order 43, and the secondary cutoff is around 250 eV that close to 81^{st} harmonic. 91

Figure 7.5. Experimental comparison of driving laser ellipticity scan of the driven laser in Helium(top) and Argon(bottom). 92

Figure 7.6. Experimental Ellipticity scan of the driven laser in hydrogen. There is no sign of a secondary plateau so far. 93

Figure 7.7. Theoretical TDSE time-frequency analysis and HH spectrum for laser intensity of 2×10^{15}W/cm^2 and 2.25×10^{15}W/cm^2. 94

Figure 7.8. Theoretical TDSE time-frequency analysis and HH spectrum for laser intensity of 2.5×10^{15}W/cm^2 and 2.75×10^{15}W/cm^2. 95

Figure 7.9. Theoretical TDSE time-frequency analysis and HH spectrum. The horizontal dashed line in A and the vertical dashed line in B show the cutoff from different ions and DER.(A and B): Laser intensity of 3×10^{15}W/cm^2. Graph from Alda de las Heras from Carlos Hernandez-Garcia group. 96

Figure C.1. Conical grating efficiency for 500 line/mm, 1200 line/mm, 3600 line/mm, and 4968 line/mm with 2 and 4 degrees of incident angle. 100

LIST OF TABLES

Table A.1. Ionization potentials of selected atoms and ions (From NIST). 97

Table B.1. Atomic unit in SI unit and its physical significance. 98

ACKNOWLEDGEMENTS

Chapter 3, partially, is currently being prepared for the publication of the material: High-performance compression of VIS 515 nm laser pulses for bright phase-matched EUV - X-ray high-order harmonic generation at kHz-MHz repetition rates, Siyang Wang, Jieyu Yan, Sirius Song, Alexander Atanassov, Zhihan Wu, Dimitar Popmintchev, Tenio Popmintchev. The dissertation author was the primary investigator and the author of this paper.

Chapter 5, in full, is currently being prepared for the publication of the material: Wavelength-Tuneable High-order Harmonics: A Novel Approach for Narrow Bandwidth, Coherent and Bright EUV - Soft X-ray Radiation with Controlled Spectrum. Dimitar Popmintchev, Siyang Wang, Jieyu Yan, Sirius Song, Ryan Clairmont, Zhihan Wu, Elizaveta Gangrskaia, Tenio Popmintchev.The dissertation author is the co-author of this paper.

Chapter 7, in full, is currently being prepared for the publication of the material: Surprise in Highly Correlated Two-Electron System: Extended Secondary Plateau in X-ray High Harmonic Generation from Helium Due to Double Electron Recombination. Siyang Wang, Jieyu Yan, Alba de las Heras, Sirius Song, Aleksander Prodanov, Zhihan Wu, Carlos Hernández-García, Luis Plaja, Dimitar Popmintchev, and Tenio Popmintchev. The dissertation author was the primary investigator and the author of this paper.

VITA

2015	B.S. in Engineering Physics, University of Illinois at Urbana Champaign
2023	Ph.D. in Physics, University of California San Diego

PUBLICATIONS

Siyang Wang, Jieyu Yan, Sirius Song, Alexander Atanassov, Zhihan Wu, Dimitar Popmintchev, Tenio Popmintchev. ”High-performance compression of VIS 515 nm laser pulses for bright phase-matched EUV - X-ray high-order harmonic generation at kHz-MHz repetition rates.”*(In Preparation)*

Siyang Wang, Jieyu Yan, Alba de las Heras, Sirius Song, Aleksander Prodanov, Zhihan Wu, Carlos Hernández-García, Luis Plaja, Dimitar Popmintchev, and Tenio Popmintchev. ”Surprise in Highly Correlated Two-Electron System: Extended Secondary Plateau in X-ray High Harmonic Generation from Helium Due to Double Electron Recombination.”*(In Preparation)*

Dimitar Popmincthev, **Siyang Wang**, Xiaoshi Zhang, Ventzislav Stoev, and Tenio Popmintchev. ”Analytical Lah-Laguerre optical formalism for perturbative chromatic dispersion.” *Opt. Express*, 30(22):40779–4080, (2020)

Dimitar Popmintchev, Aref Imani, Paolo Carpegiani, Joris Roman, **Siyang Wang**, Jieyu Yan, Sirius Song, Ryan Clairmont, Zhihan Wu, Valentina Shumakova, Elizaveta Gangrskaia, Edgar Kaksis, Tobias Flöry,1 Andrius Pugzlys, Andrius Baltuska, Tenio Popmintchev” Wavelength-Tuneable High-order Harmonics: A Novel Approach for Narrow Bandwidth, Coherent and Bright EUV - Soft X-ray Radiation with Controlled Spectrum.” *(In Preparation)*

ABSTRACT OF THE DISSERTATION

Bright Coherent EUV and X-ray Light driven by UV and Visible Lasers and Attosecond-to-femtosecond Electron-Electron Correlation Spectroscopy and Recombination Physics

by

Siyang Wang

Doctor of Philosophy in Physics

University of California San Diego, 2023

Professor Tenio Popmintchev, Chair

With the physics of coherently upconvert ultrafast driving laser photon, the high harmonic generation process enables a table-top laser source that is able to cover EUV to X-ray with a fully coherent attosecond burst. Its spectroscopic feature and extreme spatial and temporal resolution made it emerge as a novel tool for scientific research over the last three decades. The main limitation of this source to be is the brightness which is highly related to the phase-matching condition and the efficiency of optics after generation.

The first observation of high harmonic generation is with a UV excimer laser with 248 nm over 30 years ago. This thesis presents works performed with the modern engineering design

of high harmonic beamlines and a better understanding of phase-matching and physical models that were developed nearly thirty years. Chapter 3 is the selected experimental result of post-laser manipulation of laser parameters to a shorter pulse duration for more efficient high harmonic emission. Chapter 4 is a summary of our modern design of the beamline with hollow waveguide manufacturing and novel EUV to X-ray spectrometer design in both transmission and reflection mode with calculation and optimization where record-high efficiency spectrometer is designed and tested that can capture the most sensitive signal with physical significance that possibly ignored in the past. Chapter 5 presents an investigation of the feasibility of high harmonic spectrum tunability by shifting the spectrum of the driving laser in both directions to enable the spectroscopic study of metal resonance absorption edge. Finally, Chapters 6 and 7 present experimental results of the 400nm UV laser driving high harmonic with the robust parameter space for bright emission in the UV and X-ray regime for future application. The stable and robust harmonic emission is used as a platform for the spectroscopic study of the possible correlation effect between electrons and ions. For the first time, a double electron recombination process with an extended high harmonic cutoff in two-electron atoms has been experimentally observed which could pave the way for a better understanding of the few electron systems and contribute to further completing the theory of high harmonic generation.

Chapter 1

Introduction - fully coherent High order Harmonics generation

1.1 Discovery of High Harmonic Generation using 248 nm lasers

High Harmonic Generation is an extreme nonlinear process that coherently upconverted the ultrafast driving laser photon into radiation of photon with odd multiples of energy of driving laser photon. The first observation of HHG in noble gasses is generated using UV excimer KrF lasers($\lambda_{Laser} = 248$ nm) [1]. Where emission in a vacuum-ultraviolet regime was measured with the highest photon to be more than 100 eV. Later similar phenomenon was observed by using an Nd: YAG driving laser[2]. The behavior of the High Harmonic(HH) spectra was observed with new features where the harmonics were equally spaced and a broad range of them was with close intensities - now called as 'the plateau region'.

1.1.1 Extreme Nonlinear Optics Regime

Studies of nonlinear optics started when the second harmonic generation is observed not long after the invention of the laser. Franken and his colleagues observed a second harmonic generation in quartz from a laser[3]. Phase-matching as a theoretical interpretation of this phenomenon came out the very next year[4]. For decades of research and trial, efficient low-order harmonics can be generated by using birefringent nonlinear crystals. The whole process of low-order harmonics in a nonlinear crystal can be also simulated well. The nonlinear crystals can be also manufactured precisely. But there is still no choice of crystal that can efficiently yield harmonics with a wavelength shorter than 200 nm.

For low-order harmonics generation(second to fifth), the efficiency is closely related to the order of the harmonics. A relative ratio between successive orders of nonlinear susceptibilities roughly follows:

$$\frac{|\chi^{(n)}|}{|\chi^{(n11)}|} = \frac{1}{E_0} \tag{1.1}$$

Where $|E_0|$ is the magnitude of average electric field strength inside the specific atom. Most of the time it is with orders more than 10^{11}V/m. The electric polarization of successive order then roughly follows:

$$\frac{|P^{(n)}|}{|P^{(n-1)}|} \approx \frac{|E||\chi^{(n)}|}{|\chi^{(n-1)}|} \approx \frac{|E|}{|E_0|} \tag{1.2}$$

Where $|E|$ is the magnitude of the applied laser electric field. For most of the ordinary light sources without super high spectral brightness, this ratio is quite small. For such reason, direct third harmonic generation with crystal is rare compared to direct second harmonic generation. The low-order harmonics also follow an intensity power law such that the yield of n-th harmonics follows I^n where I is the laser intensity.

In Figure 1.1. The low-order harmonics still follow the intensity power law that can be explained by the perturbative expansion of the nonlinearities. The major mechanism is still the electron-cloud distortion that the interaction between the laser field and medium is non-resonant. While with the development of ultrafast laser techniques, high laser peak intensity is available to trigger different extreme nonlinear processes. The plateau behavior of the HH spectra can be explained by the non-perturbative theory where the equal intensities of high-order harmonics can be explained with a different theory of physics other than the electrical polarization.

With the development of laser techniques from gain switching to Q-switching to mode-locking incorporating cavity dumping or regenerative amplifiers, strong laser pulse with higher and higher peak intensity becomes possible. With each step of development in technique,

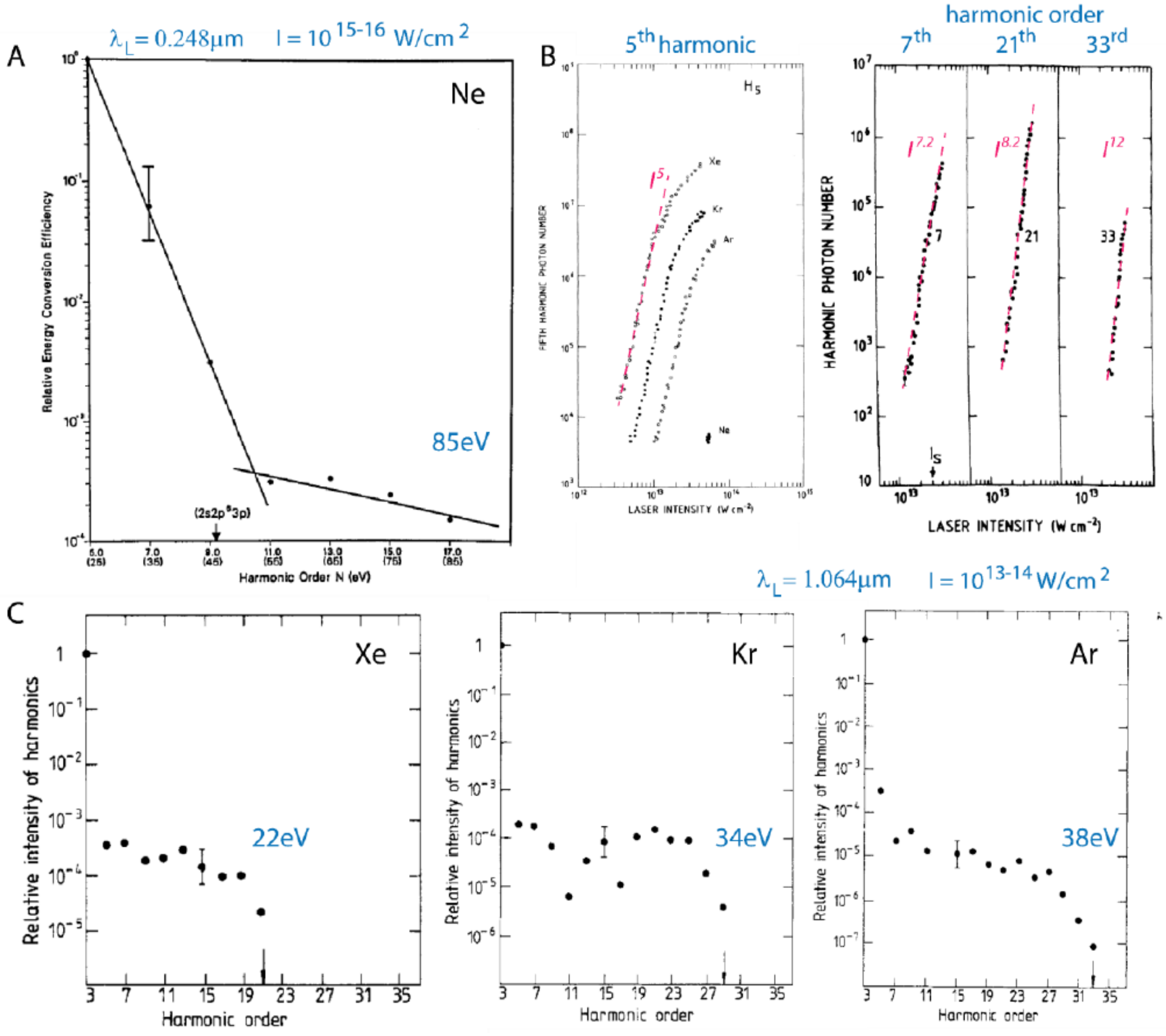

Figure 1.1. A. HHG from neon atom and ion species using 248 nm driving laser. B-C. HHG using 1064 nm driving laser with moderate intensity 10^{13-14}W/cm^s in Xe, Kr, and Ar. The power scaling of the harmonic yield demonstrates the intensity scale I^n is gradually not valid for the non-perturbative high-order harmonics. Adapted from [1, 2, 5]

new physics also comes. Interacting with an ultrafast intense laser field, the laser-induced breakdown of gases era started and has led to many new physical phenomena such as multiphoton ionization(MPI) and above-threshold ionization(ATI). The advancement of laser technology enabled the requirement of Keldysh parameter[6] to be less than unity[7]. From where tunnel ionization started to be observed and the format of the Keldysh formula got improved. With these understandings of the initial step of HHG. Quasi-classical theory[8, 9] in the early 90s can successfully reproduce a plateau region as observed. Rescattering theory by Kuchiev [10] and the 'simple men model' [11] was also widely accepted.

1.1.2 Coherent and incoherent short-wavelength Extreme Ultraviolet and X-ray light source

Extreme Ultraviolet(EUV) and X-ray light sources can be classified into two categories: Coherent and incoherent. Their generation process and application are vastly different.

A laser is an artificially-made coherent light source. Where coherence can be generally described that at two points in either space or time along the laser light propagates, the phase relationship between the two points is analytical. The coherence behavior makes the laser an extremely useful tool in scientific research and the industrial world. Microwave and infrared laser is well-developed. But the demand for the shorter-wavelength laser is never truly fulfilled. The optical community found it challenging to design a shorter wavelength laser.

EUV or soft X-ray lasers mostly can be only single-pass lasers since there is no good candidate EUV or soft X-ray mirror that can serve as an end cavity mirror. The pump laser scattering and possible plasma debris also limit the feasibility of building a multipass cavity. Also, the gain of a laser is related to the cross-section of the stimulated emission and the cross-section of absorption or the A and B Einstein coefficients. The stimulated cross-section $\sigma_{stim} \propto \frac{\lambda^3}{\Delta\lambda/\lambda}$. This means the efficient lasing requirement is hard to achieve with shorter and shorter lasing wavelengths. We can also understand this process as the radiative lifetime has an inverse relationship with the transition energy as the Heisenberg uncertainty principle suggested. And large pump power $P_{pump} \propto 1/\tau\lambda^3 \sim 1/\lambda^{3.5-5}$ is required to maintain this population inversion. The early trial had been made on creating population inversion in hydrogen-like Carbon ions with carbon fibers by induced by a high-power laser. Also, later on scientists tried collisionally pumped Neon-like[12] and Nickel-like[13] lasers. For Ne-like, the collisional excitation excites electrons from the 2p to 3p state, and population inversion is produced between the 3p to 3s state. For Ni-like, the electron is excited from 3d to 4d state, and the lasing is from the 4d to 4p transition. Such kind of lasers was able to output up to miliJoule level and picosecond pulse duration. These lasers can provide a moderate level of coherence and few mrad of beam divergence.

The coherence in the EUV and X-ray ranges is important for the scientific study on the ultrafast dynamic with sub-femtosecond($< 10^{-15}$s) time scale which is the typical timescale for the atomic level physical phenomenon. Also a promising way to be able to image with subnanometer($< 10^{-9}$m) spatial resolution since the rayleigh resolution somehow set the limitation of imaging by using optics.

$$d = \frac{1.22\lambda}{NA}$$

X-ray free electron lasers, synchrotron facilities, and table-top HHG sources are the major three coherent X-ray light sources. They have different coherence levels and different limitations based on their approaches that I will discuss further in the next few sections.

The peak brightness of the EUV-X-ray source is defined as the pulse energy, per unit volume in a six-dimensional space that includes both transverse and longitudinal directions. The comparison of brightness of different sources can be found in Fig 1.2.

$$P_{Bright} = \frac{Energy}{Phase\ Space} = \frac{N_{ph} 2.3556^2}{(2\pi)^3(\Delta E/E)\tau \underbrace{(\pi r_0^2)}_{\textbf{Area}} \underbrace{(2\pi(1-\cos\theta))}_{\Omega_{solid}}} \tag{1.3}$$

where θ is the half angle of divergence, r_0 is the beam radius.

Incoherent X-ray light sources are widely used in medical imaging of hidden body tissue since tissue, bones, and other parts of the body absorb or scatter X-ray differently. The origin of this type is Crookes tubes where Röntgen discovered X-ray by using it. The basic idea is to apply high voltage to accelerate the electron ionized from the residual air and then hit the anode with the high-velocity elections. Bremsstrahlung and X-ray fluorescence both contribute to the signal. Other incoherent sources also find their industrial application such as the laser-driven plasma source that can be made for EUV lithography. ASML made a technical breakthrough by

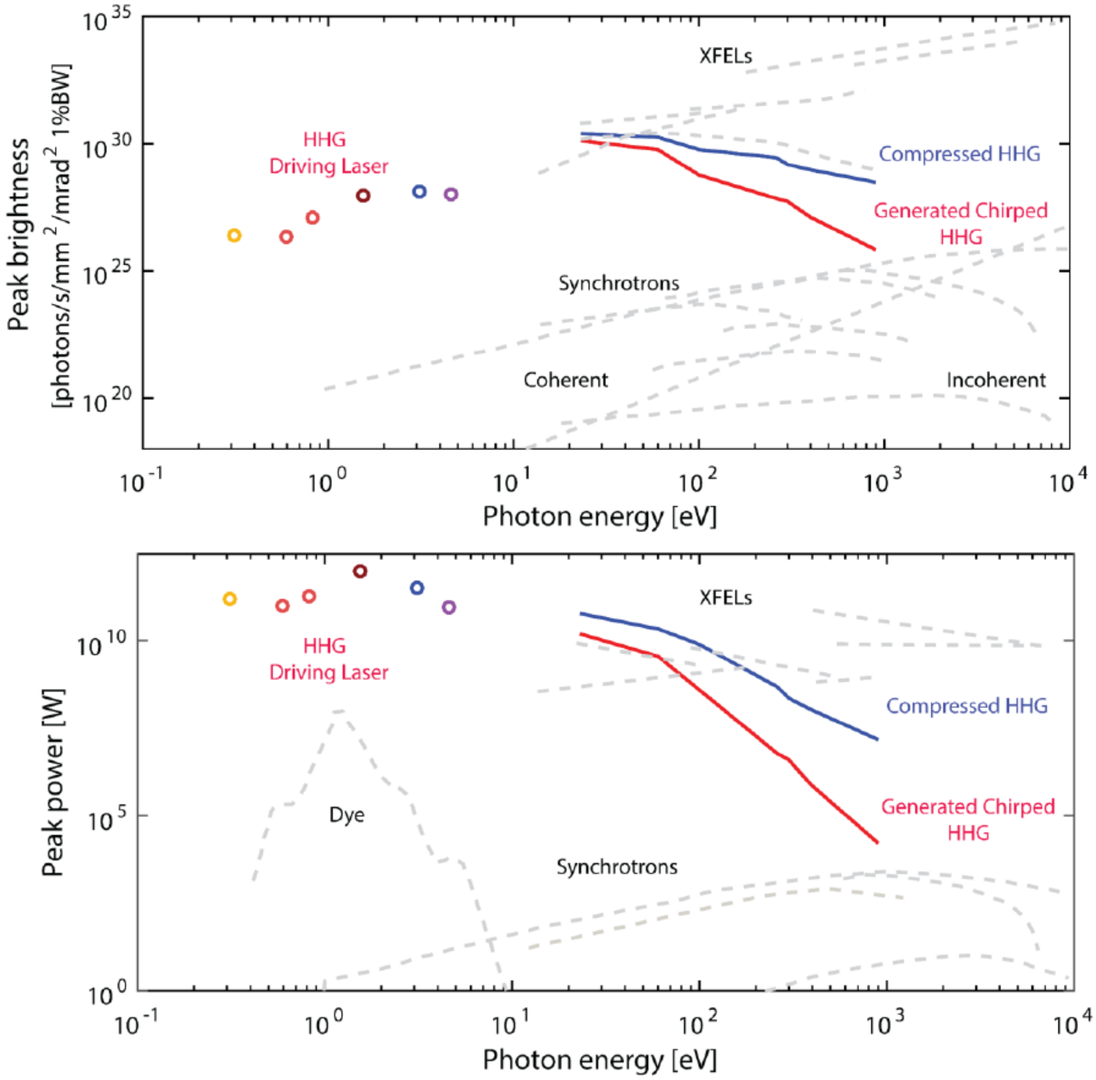

Figure 1.2. Top: Peak brightness of coherent HH X-ray sources compared with FEL and synchrotron sources. Bottom: Peak Power comparison.(The circles represent different driving laser photon energy from 0.32eV to 4.6eV). Graph from Dimitar Popmintchev.

using pre-pulse laser to manipulate the tin droplet shape that boosts the efficiency of 13.5nm narrowband EUV signal by around 5 times making the EUV lithography machine able to be used for high-volume manufacturing. The lack of coherence, especially spatial coherence, is needed in lithography to avoid interference.

1.2 Advantages of High Harmonic EUV and X-ray light

1.2.1 Full spatial coherence

For laser filed at two different spaces and times. We can use a mutual coherence function Γ to define its spatiotemporal coherence:

$$\Gamma(\mathbf{r_1},\mathbf{r_2},t_1,t_2) = \Gamma_{12}(t_1 - t_2) = \Gamma_{12}(\tau) = \langle E(\mathbf{r_1},t+\tau)E^*(\mathbf{r_2},t)\rangle \tag{1.4}$$

With this definition, $\Gamma_{11}(\tau)$ can be used to define the self-coherence at position 1. If no time difference then $\Gamma_{12}(0)$ can be used to define the spatial coherence. Double-slit interference is a quick method to check the spatial coherence of a light source.

Previous double-slit interference data and calculations of HHG by different driving lasers(Fig 1.3) show HHG light sources could be with excellent spatial coherence. With such spatial coherence, the diffraction pattern then is analytical and can be used to retrieve more spatial information. Also, the divergence of the HHG source is very small which behave more laser-like than other sources and be a good candidate for lensless imaging experiment.

1.2.2 Temporal coherence

HHG source potentially could have good temporal coherence since it is a phase-matching process. Research[14] matches well with the experimental result. The temporal coherence property can mostly transferred to the electron wavefunction when meets a relatively good phase-matching condition. Two different points of HHG can be with locked phase and interference within a single harmonic is easy to be observed in the far field as expected.

The emission of HH requires the electron wavepacket to be able to be back to the parent ion. There are two major trajectories that contribute to this recombination. In reality, the short trajectory is usually able to inherent better temporal coherence from the laser and get less affected by the chirp from the rapid variation of the laser phase. In some cases, different temporal

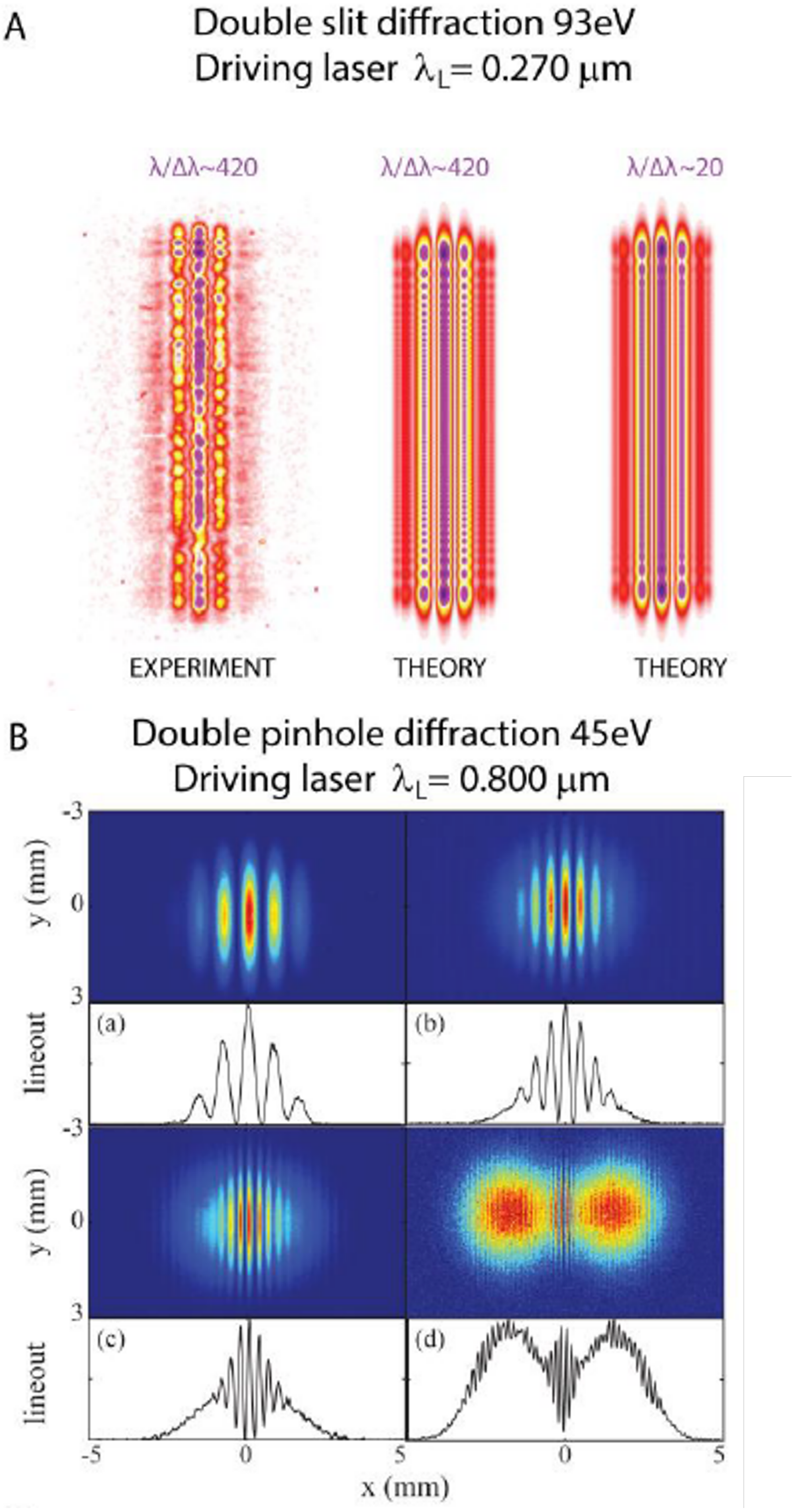

Figure 1.3. Double-slit diffraction at different HH energy A) HH energy at 93eV driven by 270nm laser. B) HH energy at 45eV driven by 800nm laser. Graph from Dimitar Popmintchev.

coherence behavior can be observed where the inner region of the harmonics shows clearer fringes (Fig 1.4) which shows better temporal coherence from the short-trajectory contribution.

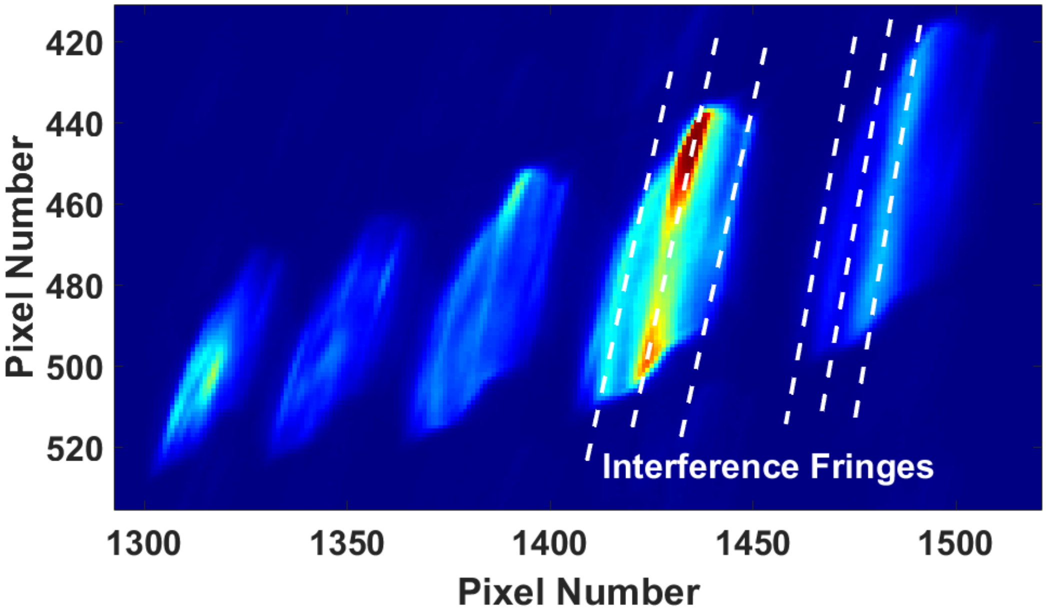

Figure 1.4. Interferece fringes within a single harmonic in the far field. The fringes follow the patterns of harmonics. The image shows high harmonics with conical diffraction order which will be explained in Chapter 4 and 6.

1.2.3 Attosecond and femtosecond spectroscopic and imaging Applications

The coherent nature of the EUV to X-ray sources mentioned above made them useful in spectroscopy and different pump-probe experiment.

High Harmonic signals as isolated subfemtosecond pulse covering EUV and X-ray range can serve as a probe to overcome the limitation of temporal resolution such that the subfemtosecond dynamics can be observed. The High Harmonic spectroscopy can be combined with the correlated measurement to reveal the dynamics of exotic behavior of ionization of different systems[15, 16, 17].

Many of the strong absorption features are around the atomic absorption edge. And many of the elements has their absorption edge in the EUV to X-ray range such as the K-edge of carbon, nitrogen, and oxygen at 284eV, 410eV, and 540eV respectively. There are also L, M, and N edges of many elements that overlap with the light source covers. Transient absorption spectroscopy took this advantage and becomes a novel technique to reveal the electron motion in atomic[18, 19], molecular[20], and solid-state[21, 22, 23] systems. The EUV absorption spectrum can be measured as a function of pump-prob delay and this technique could be time-resolved.

There are other subsets of EUV and X-ray absorption spectroscopy that has advantages in probing atomic structure and dynamics. The atomic types, their coordination number, the inter-atomic distance, and disorder can be retrieved from the extended X-ray absorption fine structure. The oxidation state and the symmetry of coordination chemistry can be probed with Near Edge Absorption Fine Structure.

Another novel application is imaging with near-wavelength or even sub-wavelength[24] resolution. Coherent diffraction imaging is different from conventional microscopy where no really good lenses can be found for the EUV to X-ray regime for this application. The Soft X-ray microscope uses Fresnel zone plate lens, but such microscope are mostly useful from thick wet specimens[25]. The resolution of Soft-X-ray microscope also get limited by the zone plate lens to be mostly more than 30nm. The combination of robust and powerful coherence light source such as HHG or X-ray free electron laser greatly boost the power of X-ray imaging[26].

There are many possible configuration of CDI such as plane -wave CDI, Bragg CDI, Ptychographyc CDI, and Fresnel CDI for being the transmissive configurations. Reflection CDI is also valid.The diffraction pattern got recorded by a ccd and the iterative phase retrival algorithm will iterate between real and reciprocal space untill the correct phase information is retrieved.

For coherent diffraction imaging(CDI), there are temporal and spatial coherence that limits:

$$L_{longitudinal} = \frac{\lambda E_{ph}}{\Delta E} \tag{1.5}$$

Which can be regarded as temporal coherence where E_{ph} is the photon energy.

$$L_{transverse} = \frac{\lambda R}{2D_s} \tag{1.6}$$

Which can be regarded as spatial coherence where D_s is the beam size and R is the distance from the source. The coherence is required to be at least twice as the smaple size that:

$$\frac{D}{d_{pixel}} = \frac{\lambda}{\Delta\lambda} = \frac{E_{ph}}{\Delta E} \tag{1.7}$$

Such that all phase information can be recorded. For High-Harmonic Sources, narrower spectral linewidth $\Delta\lambda/\lambda$ will gain the advantage of having a larger field of view and being able to achieve better resolution with a smaller number of scans[27]. UV-driven Harmonics, due to the broader temporal phase-matching window, usually able to achieve at least 3 times of spectral resolution than normally used 800nm driven HH.

Chapter 2

Quantum and Extreme Nonlinear Optics Design of Coherent EUV and X-ray Light

2.1 Microscopic physical understanding/ Physical Model

2.1.1 Full Quantum model

The theory of High Harmonic Generation is still under development. The full-Quantum Model of High Harmonic Generation proposed in recent years[28, 29] is able to predict spectrum and HH photon statistics affected by quantum effects. The major difference between the full-quantum model between the old ones is that the radiation emission and the driving laser field are treated classically instead of using a quantum formalism. The full-quantum model provides a full quantum-electrodynamical solution.

The development of a fully quantum model will be very helpful in revealing the quantum nature that happened during the process such as the entanglement between the photon and the emitting atoms.

2.1.2 Semi-classical simple-man rescattering model

The Seimi-classical model is with three steps. This is also called the three-step model as illustrated in Fig 2.1.The first and last steps are described using the quantum approach and the second step is purely classical.

1. Tunnel ionization where strong laser field ionizes electron from its parent atom.
2. The electron treated moves freely by the laser electric field. While it is moving, it also picks up kinetic energy from the laser field.
3. When satisfying a certain requirement, an energetic electron recombines with its parent ion, and a HH photon is emitted.

The first and last steps are described using the quantum approach and the second step is purely classical.

With the development of laser techniques from gain switching to Q-switching to mode-locking incorporating cavity dumping or regenerative amplifiers, strong laser pulse with higher and higher peak intensity becomes possible. With each step of development in technique, new physics also comes. Interacting with an ultrafast intense laser field, the laser-induced breakdown of gases era started and has led to many new physical phenomena such as multiphoton ionization(MPI), above-threshold ionization(ATI) then tunnel-ionization(TI).

Keldysh for the first time[6], proposed to treat different ionization regimes analytically, and he proposed a parameter known as the ”Keldysh parameter”:

$$\gamma = \frac{w}{\mathscr{E}}\sqrt{2E} \tag{2.1}$$

E is the ionization potential. $\mathscr{E}$ is the electric field strength of the laser pulse.

For tunnel ionization $\gamma \ll 1$. It actually proved experimentally[30] for $\gamma < 1/2$. When $\gamma \gg 1$, the multiphoton effect usually dominates. It can be also treated as:

$$\gamma = \frac{\text{tunnelling time}}{\text{half-laser cycle}} = \frac{\tau_T}{\frac{1}{2}\tau_L} \tag{2.2}$$

He also first proposed the ionization rate of the hydrogen atom in the quasi-static limit:

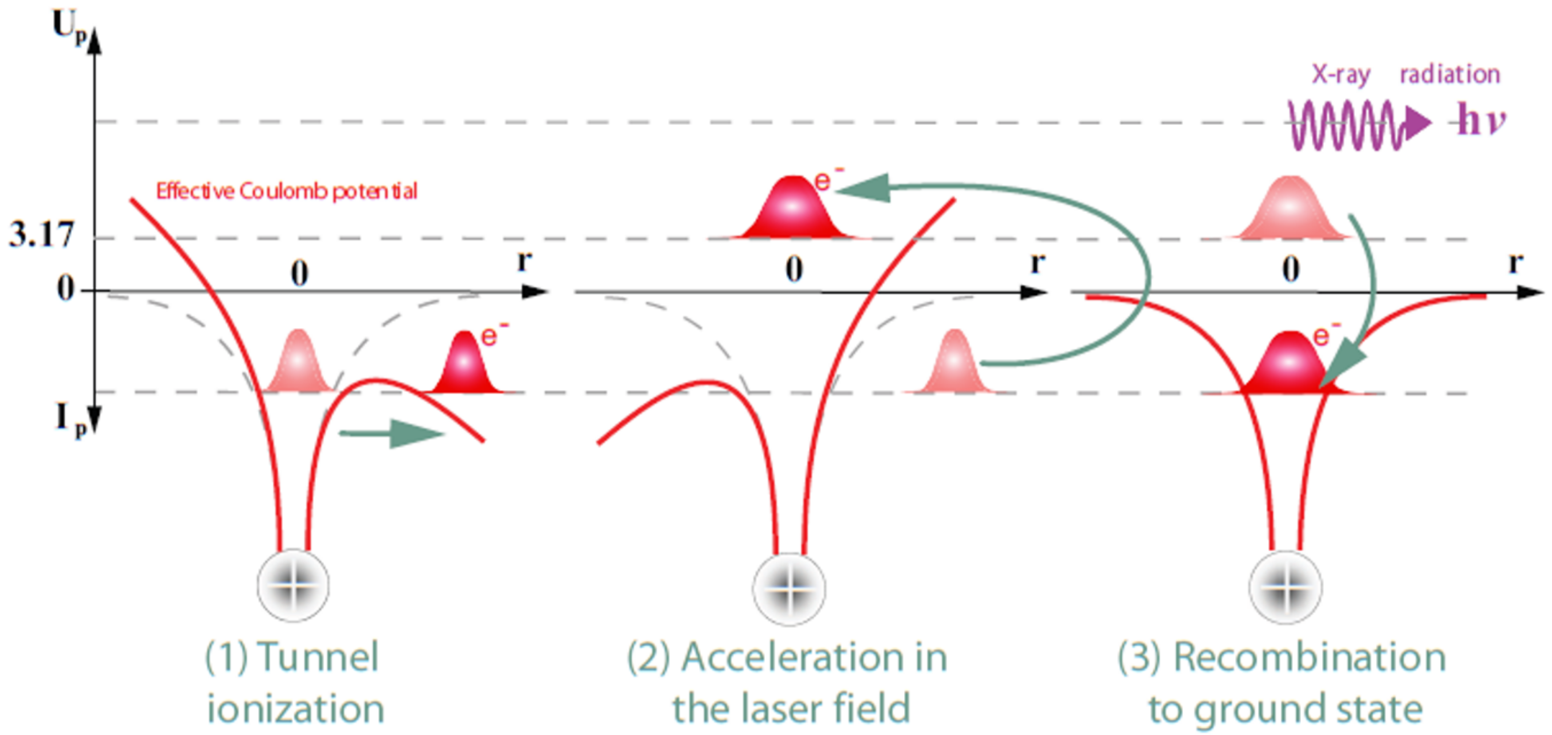

Figure 2.1. Schematics of the semi-classical simple-man rescattering process.Graph from Tenio Popmintchev.

$$\omega_{Keldysh} = \frac{\sqrt{6\pi}E}{4\hbar}\left(\frac{e\hbar\mathscr{E}}{m^{1/2}E^{3/2}}\right)^{1/2} \times \exp\left\{-\frac{4\sqrt{2m}E^{3/2}}{3e\hbar\mathscr{E}}\left(1-\frac{m\omega^2 E}{5e^2\mathscr{E}}\right)\right\} \tag{2.3}$$

If using the atomic unit:

$$\omega_{Keldysh} = \frac{\sqrt{6\pi}E}{4}\left(\frac{\mathscr{E}}{E^{3/2}}\right)^{1/2} \times \exp\left\{-\frac{4\sqrt{2}E^{3/2}}{3\mathscr{E}}\left(1-\frac{\omega^2 E}{5\mathscr{E}}\right)\right\} \tag{2.4}$$

Here ω is the laser angular frequency.

Later on, Perelomov[31] improved the rate of an arbitrary state of a hydrogen atom:

$$\omega = C_{n,l}^2\left(\frac{3\mathscr{E}}{\pi\mathscr{E}_0}\right)^{1/2} E\frac{(2l+1)(l+|m|)!}{2^{|m|}(|m|)!(l-|m|)!}\left(\frac{2\mathscr{E}_0}{\mathscr{E}}\right)^{2n-|m|-1} \times \exp\left\{\left(-\frac{2\mathscr{E}_0}{3\mathscr{E}}\right)\right\} \tag{2.5}$$

Where Z is the atomic residue charge. For a neutral atom Z=1.The factor $3\mathscr{E}/\pi\mathscr{E}_0$ is the result of averaging the rate over one driving laser cycle. The $\left(\frac{2\mathscr{E}_0}{\mathscr{E}}\right)^{2n^*-|m|-1}$ represents the long-range effect of the Coulomb potential. All equations in this section are written with atomic system units with ($\hbar = m_e = e = 1$, see Appendix C for more detail). Later on, Ammosov, Delone and Krainov generalized this analytical theory[32] and proposed the expression of the tunnel ionization probability, also known as the ADK ionization rate:

For $n^* \gg 1$, ionization rate:

$$\omega = C_{n^*l^*}^2\left(\frac{3\mathscr{E}}{\pi\mathscr{E}_0}\right)^{1/2} E\frac{(2l+1)(l+|m|)!}{2^{|m|}(|m|)!(l-|m|)!}\left(\frac{2\mathscr{E}_0}{\mathscr{E}}\right)^{2n^*-|m|-1} \times \exp\left\{\left(-\frac{2\mathscr{E}_0}{3\mathscr{E}}\right)\right\} \tag{2.6}$$

$$n^* = Z(2E)^{-1/2}, \mathscr{E}_0 = (2E)^{3/2} \tag{2.7}$$

ADK extends the scope by replacing n,l by the effective principal and angular momentum quantum number n^*, l^*. $l^* = n^* - 1$

If optimize by using the asymptotic form of the radial electron wavefunction in a Coulomb potential.

$$\omega = \left(\frac{3e}{\pi}\right)^{3/2} \frac{Z^2}{3n^{*3}} \frac{2l+1}{2n^*-1} \left[\frac{4eZ^3}{(2n^*-1)n^{*3}\mathscr{E}}\right]^{2n^*-3/2} \exp\left(-\frac{2Z^3}{3n^{*3}\mathscr{E}}\right) \tag{2.8}$$

e=0.71828, $F = \mathscr{E}$. This is valid down to $n^* \sim 1$.
Above one is for the case m=0 because the other terms with different m being negligible when $\mathscr{E}_0/\mathscr{E} \gg 1$.

Population and depletion rate of each ion as time progresses, ionize one electron at most in half laser cycle. The ADK rate follows the laser intensity profile. The ionization rate of a given ion is the ADK rate multiplied by the population of that ion. The population of the ion depends on the ionization rate of the previous ion and on its own ionization rate. Population between ions follow a series of differential equations.

$$dN_0(t) = -N_0\gamma_1 dt$$

$$dN_1(t) = N_0(t)\gamma_2 dt - N_1\gamma_2 dt$$

$$dN_2(t) = N_{1l}(t)\gamma_2 dt - N_2\gamma_2 dt$$

......

Where γ_i represents the ADK rate that ionizes to i^{th} ion. N_i represents the population of different ions. The total number of atoms/ions is constant to be unity. Fig 2.2 shows the typical calculation of the ionization rate and Fig 2.3 shows the ion population evolution of 400 nm driving laser with a 20 cycle pulse duration and with peak intensity 2.5×10^{15}W/cm^2.

The propagation step treats the electron as a free electron whose motion is only affected by the external laser field. Assume a sinusoidal laser field $E(t) = E_0 \cos\omega_L t$ and the initial

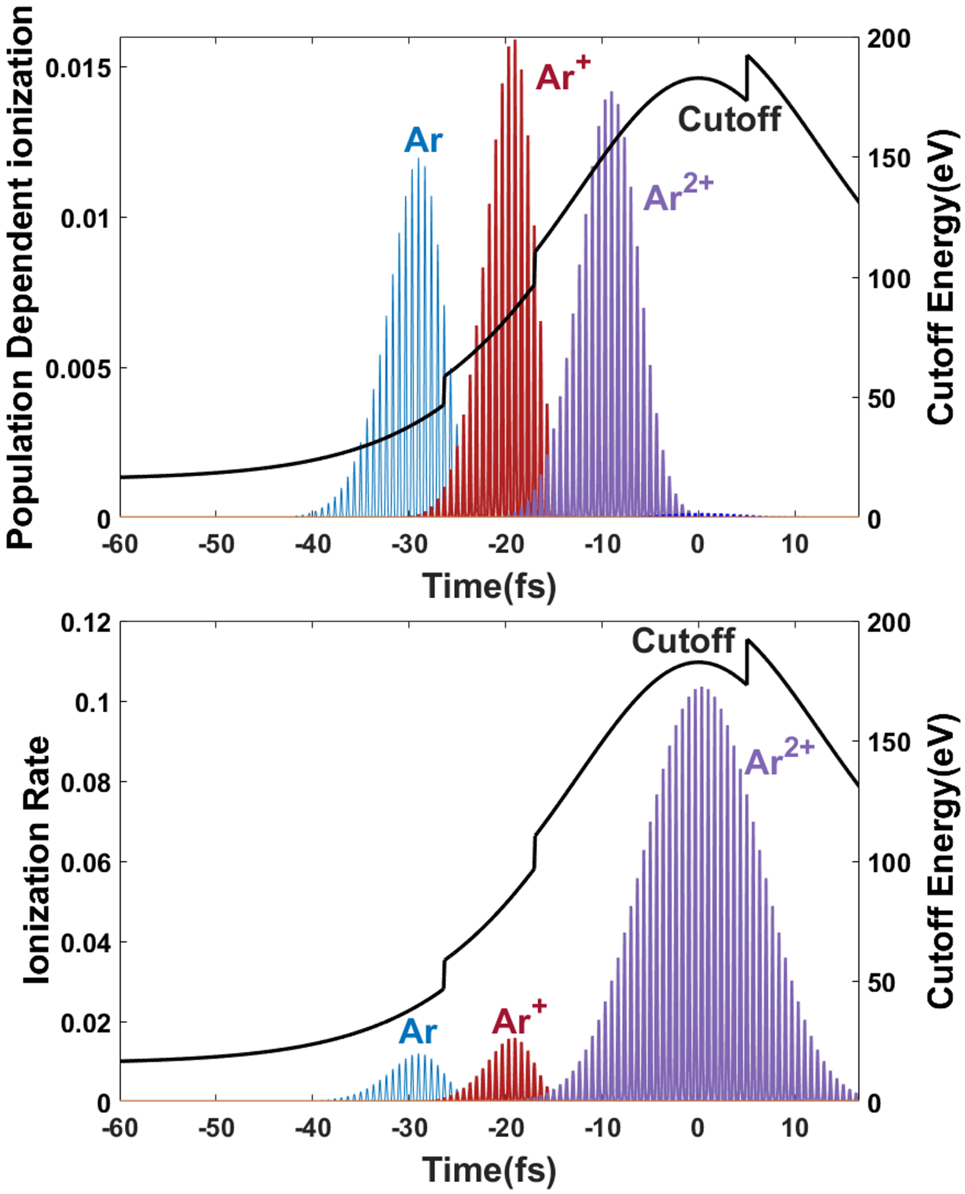

Figure 2.2. Top: ADK rate coupled with the population of neutral atoms and ions. Different ion species has their brightness emission at different time and with different HH photon energy. Bottom: ADK rate in terms of time. Shows time-wise when the ionization from certain ions could be the most efficient.

boundary condition to be both zero ($x_0 = 0, v_0 = 0$). The position and velocity at time t can be easily calculated:

$$v(t) = -\frac{E_0 e}{m\omega_L}\left(\sin\left(\omega_L t + \phi\right) - \sin\left(\phi\right)\right) \tag{2.9}$$

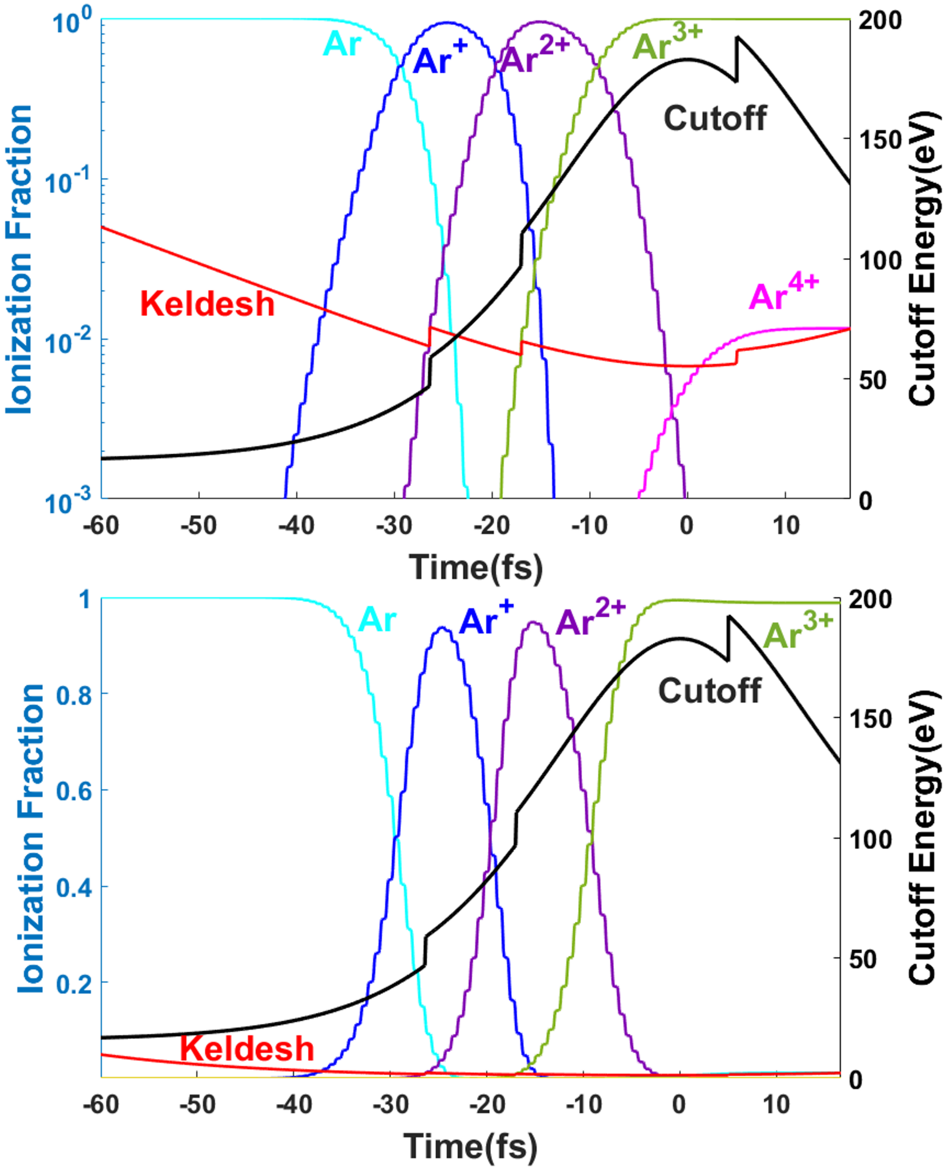

Figure 2.3. Population and ion species change over time. The total number of atom and ions remain constant. Top: log-scale. Bottom: linear scale.

$$x(t) = -\frac{E_0 e}{m\omega_L^2}(\cos(\omega_L t + \phi) - \cos(\phi) + \sin(\phi) t) \tag{2.10}$$

Where the phase ϕ can be understood as the electron gets ionized at different times $\omega t_0 = \phi$ Relativistic correction is usually not needed since the intensity needed for such velocity is usually with orders of 10^{17} W/cm^2. Free electron trajectory is shown in Fig 2.4.

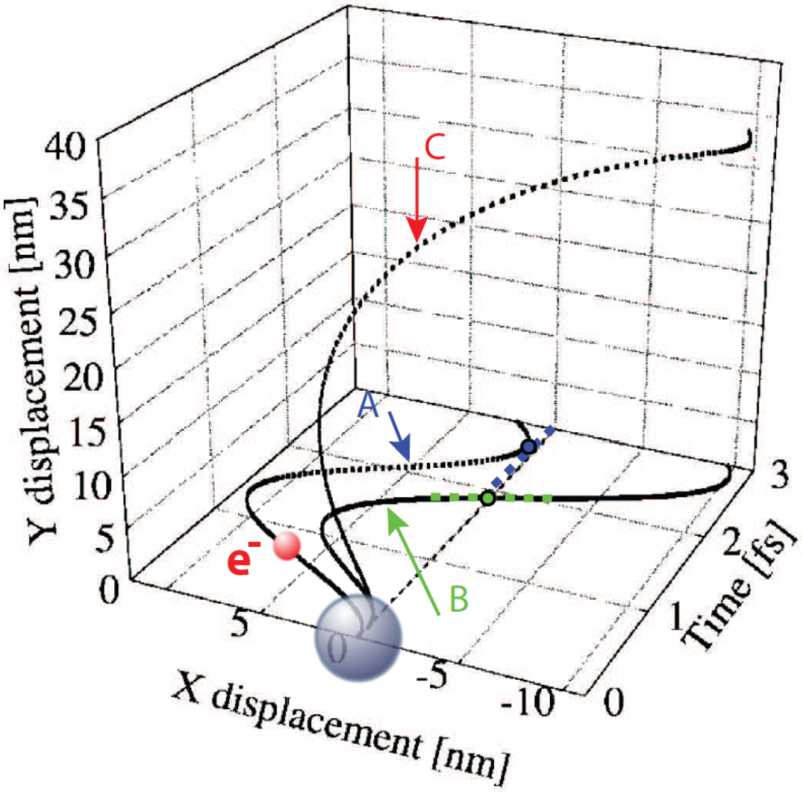

Figure 2.4. Free electron's trajectory over time affected by the laser electric field($\lambda_L = 800$nm) as a function of initial ionization phase $\phi_0 = \omega_L t_b$ where t_b is the 'born time' of the free-electron. For trajectories, A and B, the electron is able to travel back to its initial position but A is with almost no kinetic energy and B is with maximum energy, the HH photon energy emitted by these two case define the possible range of the HH emission. With a circularly polarized field(trajectory C), the electron can never goes back to its original position for any initial ionization phase. Adapted from[33]

Electrons can be ionized at any time during the half-laser cycle and accumulate kinetic energy from the laser field. However, only at time t when the free electron goes back to its parent ion x(t)=0 does the recombination possible to happen. The recombination process is treated quantum-mechanically so that the rescattering electron wavefunction spreads spatially and then shrinks and overlaps with the parent ion. A photon is able to be emitted with all the electron kinetic energy and the ionization potential of the ion.

It is not hard to find the most energetic recombination that happens when the $\phi_i = 17^\circ$ and the $\phi_r = 255^\circ$. Fig. 2.5 shows the recombination time and its corresponding accumulated kinetic energy. This is also called the HH cutoff of the simple man model.

$$h\nu_{cutoff} = 3.17U_P + I_P \tag{2.11}$$

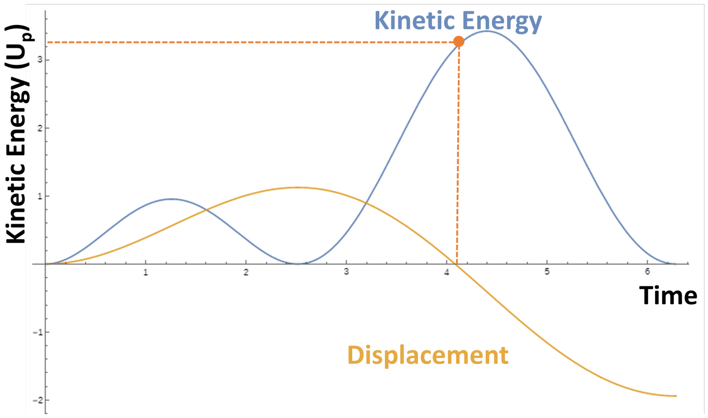

Figure 2.5. 1-D displacement vs. Kinetic Energy When displacement(yellow curve) becomes zero at $t > 0$. It may recombine with the parent ion. Then the kinetic energy(blue curve) it accumulates will be part of the energy of HH photon emitted. Here the ionization happens at around 18°, and the kinetic energy it accumulates is around $3.17U_p$.

Where U_P is the ponderomotive energy.

$$U_P = \frac{e^2E_0^2}{4m\omega_L^2} \tag{2.12}$$

For convenience, the ponderomotive energy can be calculated with $U_p[\mathrm{eV}] = 9.337 \times 10^{-14} I[\mathrm{W/cm^2}](\lambda[\mu\mathrm{m}]^2)$. Which has a good agreement with the experimental data.

2.1.3 Lewenstein model - Strong field approximation(SFA)

In 1994, Lewenstein proposed an analytical quantum theory of the HHG[34]. The laser-atom interaction is described by the time-dependent Schrödinger equation using the length gauge, assuming a linear polarized field in the z-direction,

$$i\frac{\partial}{\partial t}\psi(x,t) = \left[-\frac{1}{2}\nabla^2 + V(\mathbf{r}) + zE(t)\right]\psi(x,t). \tag{2.13}$$

The model also with three assumptions. Also called Strong-field approximation(SFA).

1. Only the ground state contribution is taken into account, all contributions from excited bound states are neglected
2. The continuum electron is treated as free without the effect of the atomic potential.
3. The depletion of the ground state is neglected.

With SFA, the time-dependent dipole moment $\langle\psi(\mathbf{r},t)|z|\psi(\mathbf{r},t)\rangle$ is given by,

$$\vec{\mu}(t) = i\int_0^t dt'^3 pE\cos(\omega t') \times \overbrace{\underbrace{\left(\vec{d}\left(\vec{p}-\vec{A}(t')\right)\right)}_{\mathbf{A}} \times \underbrace{\exp\left\{\left(iS\left(\vec{p},t,t'\right)\right)\right\}}_{\mathbf{B}} \times \underbrace{\left(\vec{d}*\left(\vec{p}-\vec{A}(t')\right)\right)}_{\mathbf{C}}}^{\textbf{Quantum three steps}} \tag{2.14}$$

Where $\mathbf{p}$ and $d(\mathbf{p})$ are the canonical momentum and the dipole transition element. $\mathbf{A}$(t) is the vector potential.

$$\mathbf{p} = \mathbf{v} + \mathbf{A}(t) \tag{2.15}$$

$$d(\mathbf{p}) = \langle\mathbf{p}|z|0\rangle \tag{2.16}$$

And S is the quasi-classical action,

$$S(\mathbf{p},t,t') = \int_{t'}^{t} dt''\left(\frac{[\mathbf{p}-\mathbf{A}(t'')]^2}{2} + I_P\right) \tag{2.17}$$

Which contains the phase advance of the continuum electron. Now, if we look back of (2.14), we can intuitively understand it as a quantum three-step model. Where A can be identified as ionization of the ground state at t', and B and C can be identified as propagation in the continuum within $t-t'$ and recombination with parent ion at time t.

If Foruier transform (2.14)

$$\mu(\omega_H) = i\int_{-\infty}^{\infty} dt \int_{-\infty}^{t} \int d^3\mathbf{p} d*(\mathbf{p}-\mathbf{A}(t)) \times \exp\left[i\omega_H t - iS(\mathbf{p},t,t')\right] \cdot E(t')d(\mathbf{p}-\mathbf{A}(t')) + c.c. \tag{2.18}$$

If treated the laser electric field as $E(t) = E_0 \cos\omega_0 t$. Fourier transforms the time-dependent dipole moment and applies the saddle-point analysis. The spectra cutoff can be derived as,

$$h\nu_{Cutoff} = 3.17U_P + f(\frac{I_P}{U_P})I_P \tag{2.19}$$

Where this $f(I_P/U_P)$ is a slowly varying function of the first order. $f(0) = 1.32$ or when $U_P \gg I_P$ and f(3)=1.25. This is a purely quantum correction from the continuum electron wavepacket affected by quantum effects such as tunneling and quantum diffusion.

2.1.4 SFA+: marriage of SFA and TDSE

As mentioned above, the standard approach of SFA is with a saddle point approximation to compute the harmonic spectra[34, 35]. The standard S-matrix SFA approach was applied to the description of photo-ionization[6] and to the HHG and discrepancies were found between real experiments and the exact numerical solution from the TDSE. Later on, Pérez Hernández et al. proposed a modification[36, 37] to the standard approach(we refer it as SFA+). The correction from the standard SFA is that SFA+ is also considers the contribution of the dipole acceleration from the effect of the field on the bound state for the rescattering process. With this correction, the compact SFA+ model has a converging result with TDSE calculation.

2.1.5 Generation of coherent X-ray using short and long wavelength driven laser

The rescattering of the electron wavepacket is laser wavelength dependent. By the cutoff equation from the above models with the ponderomotive energy to be proportional to the driving laser square, it is well accepted that the higher photon cutoff can be generated by using a driving laser with a longer wavelength λ_L[8]. However, it is suggested that the longer λ_L would result in a significantly lower single-atom yield. The more recent quantum calculation suggested the scaling to be $\lambda^{-5.5}$ for a fixed peak laser intensity and the same HH photon energy interval[38, 39, 40]. Part of the fast decreasing of HH yield can be understood by the quantum diffusion of the electron wavepacket. The time of the wavepacket diffusion scale with λ^{-3} such that longer λ_L will lead to longer diffusion time which makes the recombination harder.

Aside from HH yield. The group delay dispersion of HH(also known as atto-chirp) also behaves differently with short and long λ_L. HH signal is generated within half laser cycle and usually believed to be with pulse duration $\tau_{HH} \sim \tau_L/4$, which is able to give attosecond isolated pulse train. The atto-chirp will elongate the pulse duration which is undesirable for attosecond science. The long trajectory is with a negative chirp while the short trajectory is with a positive chirp. For both trajectories, the atto-chirp is reduced with the shorter time the wavepacket spend in the continuum, And with a larger phase-matched bandwidth(covered in the phase-matching section), the atto-chirp is further reduced. The temporal broadening of the HH pulse depends in the ratio of the atto-chirp to the pulse duration and it strongly favors intense short λ_L to approach even near transform-limited isolated attosecond pulse train.

2.2 Macroscopic Physical picture

2.2.1 Phase Matching of High Harmonic Generation

Phase-matching is a very important idea for nonlinear optics. Low-order harmonics, sum and difference frequency generation, parametric amplification and etc all require phase-matching to reach optimum efficiency. HHG finds no odd. To achieve optimal upconversion HH efficiency, the emission need to be treated in a macroscopic way that the emission from multiple atoms has to be synchronized in phase such that the product signal can build up coherently along the propagation in the media. The adiabatic phase-matching for the q^{th} order HH is given by:

$$\Delta k = k_q - qk_L \tag{2.20}$$

Where k_L is the laser wavenumber. Perfect phase-matching happens where $\Delta k = 0$. However, a mismatch always exists. The difference in the group velocities for the fundamental and output harmonics will cause destructive interference and a decrease in the HH signal strength. For HHG, the strong laser field needs to ionize atoms or molecules. Thus there are more sources that can affect the group velocity than simply propagation in a gas. Electrons, neutral atoms, and laser-induced plasma complicate the story as well as the experimental configurations. Also, the single-atom picture failed to represent all the ionized electron and their parent ion since the majority of them won't recombine in a useful way but becomes a source of the co-propagating waves. Until the late 90s, experiments demonstrated the phase-matching mechanism in free-focusing gas jet and gas-filled waveguide configurations[41, 42, 43, 44].

Phase-matching is the key for the coherent addition of the HH signal. Light in EUV to soft X-ray regime is usually well absorbed by gaseous matter. This is due to the energy of the outermost electron state of most materials being within 10-100 eV. The absorption length L_{abs} is the distance after which the intensity drops to 1/e because of the absorbing gaseous medium. The absorption length is given by:

$$L_{abs} = \frac{1}{\rho\sigma} \tag{2.21}$$

Where ρ is the gas density and σ is the absorption cross-section. Integrating the HH signal over a distance gives[45]:

$$I_q \propto \left| \int_0^L \rho A_q(z) \exp\left(\frac{z-L}{2L_{abs}}\right) \exp\left(i\phi_q(z)\right) dz \right|^2 \tag{2.22}$$

where $A_q(z)$ and $\phi_q(z)$ are the harmonic amplitude and phase of the single-atom response. L is the length of the conversion medium. If assume there is no transverse dependence of $A_q(z)$ then the equation becomes:

$$I_q \propto \rho^2 A_q^2 \frac{4L_{abs}^2}{1+4\pi^2(L_{abs}^2/L_c^2)} \left(1+\exp\left(\frac{-L}{L_{abs}} - 2\cos\left(\frac{-\pi L}{L_c}\right)\exp\left(\frac{-L}{2L_{abs}}\right)\right)\right) \tag{2.23}$$

Where the coherence is defined as:

$$L_{coh} = \frac{\pi}{\Delta k} \tag{2.24}$$

For perfect phase-matching, the (2.23) coverages to a finite value as shown in Fig 2.6.

The equation (2.20) carries a lot of information for HHG because there are many sources of dispersion that can affect on the *k*-vector at the same time with different scaling. When $\Delta k > 0$ the driving laser phase velocity is faster while when $\Delta k < 0$, the driving laser phase velocity is slower. The most common dispersion is from neutral atoms:

$$\Delta k = \frac{n_q \omega_q}{c} - q\frac{n_L \omega_L}{c} = \frac{q\omega_L}{c}[n_q(p,T) - n_L(p,T)] \tag{2.25}$$

If apply the Causius-Mossotti relationship then we can derive that,

$$n(p,T) = 1 + (n^0 - 1)\frac{pT_0}{p_0 T} \tag{2.26}$$

The temperature usually is not the optimal controlling parameter. The index of refraction increase with the pressure. Considering the index of X-rays is mostly very close to one[46]. We can get that,

$$\Delta k_{neutral} = -\frac{q\omega_L}{c}[n_L^0 - n_q^0]\frac{pT_0}{p_0 T} \tag{2.27}$$

Which is a negative quantity. It can be intuitively understood that gases will 'slow down' the driving laser but the HH is mostly unaffected.

Similar to the neutral gas contribution, the multiply charged ion provides similar dispersion. The multiply charged ion has its outer electrons more strongly bounded. In such a way, it reduces polarizability and has a lower index of refraction.

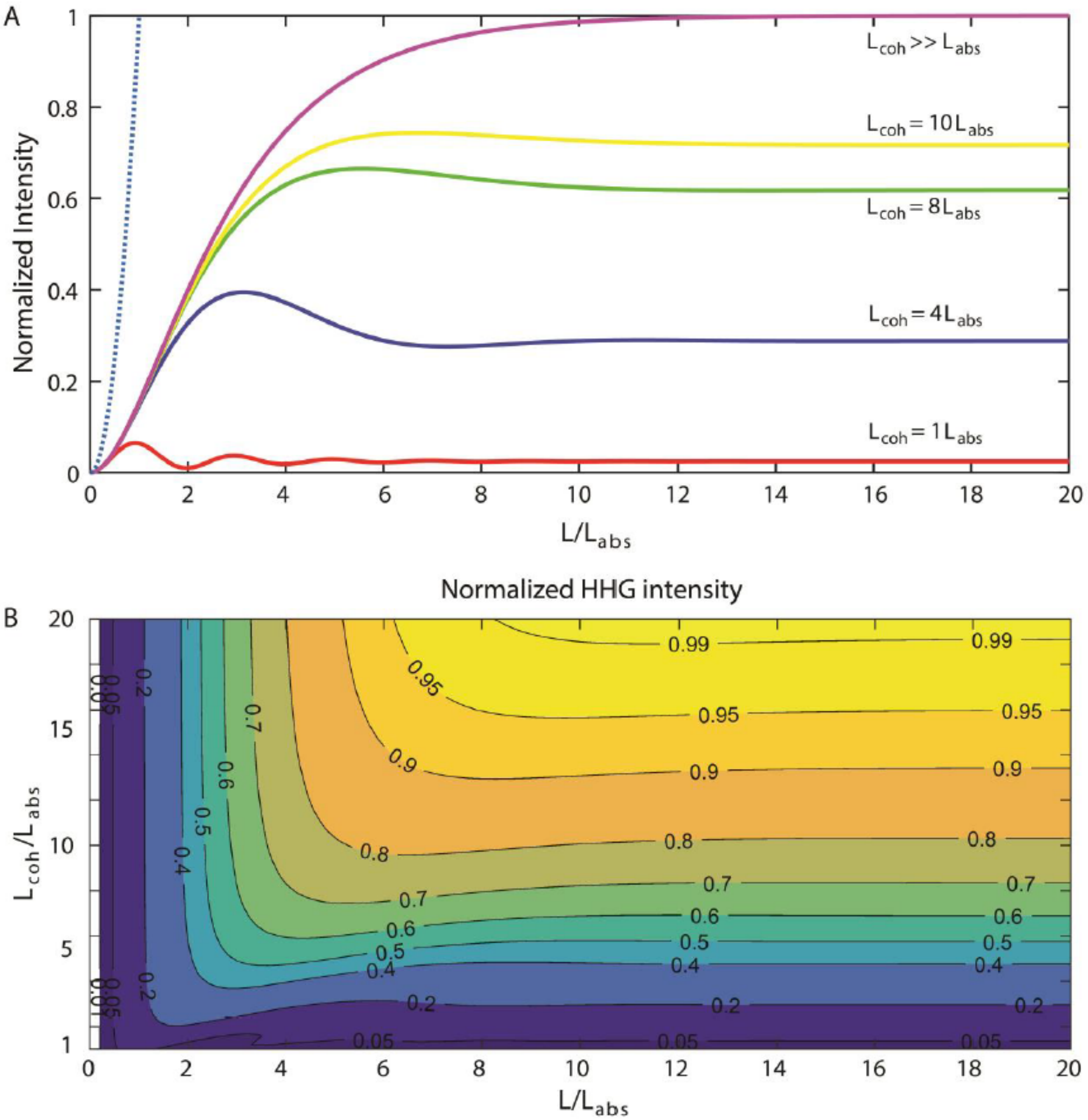

Figure 2.6. A) Normalized HH intensity as a function of L with different L_{coh}/L_{abs} ratio. B) 2D normalized intensity map in normalized coordinates L_{coh}/L_{abs} and L/L_{abs}. Graph from Dimitar Popmintchev.

While free electron is different. the free-electron index of refraction is:

$$n_e = \sqrt{1 - 4\pi c^2 \frac{\rho_e r_e}{\omega^2}} \approx 1 - 2\pi c^2 \frac{\rho_e r_e}{\omega^2} \tag{2.28}$$

Where ρ_e is the electron density and $r_e = e^2/4\pi\varepsilon_0 m_e c^2$ is the classical electron radius. Also, need to notice that all HH below the plasma frequency $\omega_p = \sqrt{4\pi c^2 \rho_e r_e}$ will be strongly attenuated. And the electron contribution is positive:

$$\Delta k = \frac{q\omega_L}{c}\frac{\lambda^2 \rho_0 \eta r_e}{2\pi}(1 - \frac{1}{q^2})\frac{pT_0}{p_0 T} \tag{2.29}$$

So to achieve minimum Δk for many orders of harmonic then the above three contribution needs to find a good balance.

The experimental configuration also matters and affects the signal quality greatly. There are two major setups: free-focusing with a gas jet and a gas-filled waveguide. For free-focusing geometry, the mismatch is usually positive,

$$\Delta k_{geometry} = \frac{qk_L r^2}{2z_R^2}(\frac{1}{q^2} - 1) + \frac{Nq}{z_R}(1 - \frac{1}{q^2}) \tag{2.30}$$

and it suffers from the Gouy phase where there will be also a transverse phase-matching issue. It is usually more beneficial to use a waveguide for HHG, it consumes gas slower and usually with a much higher efficiency and also with a much healthier contribution for phase-matching. For the glass waveguide which is a hollow-core glass capillary. The k-vector is[47]:

$$k_{waveguide} = \sqrt{k_0^2 - (\frac{u_{nm}}{a})^2} \approx \frac{2\pi}{\lambda}[1 - \frac{1}{2}(\frac{u_{nm}\lambda}{2\pi a})^2] \tag{2.31}$$

Where a is the inner radius. u_{nm} is the m^{th} root of the Bessel function $J_{n-1}(u_{nm}) = 0$. The mode will be suppressed if the cutoff HH wavelength is shorter than $\lambda_{nm} = 2\pi a/u_{nm}$. The fundamental mode HE_{11} has the longest cristal wavelength. Higher-order modes are suppressed at shorter signal wavelengths. The waveguide contribution on dispersion can be derived as:

$$\Delta k_{waveguide} = \frac{q\omega_L}{c}[\frac{1}{2}(\frac{u_{nm}\lambda_L}{2\pi a})^2(1 - \frac{1}{q^2})] \tag{2.32}$$

Which is a positive quantity.

2.2.2 Phase Matching of High Harmonics using Ti: Sapphire laser driver

The most commonly used HH driver is Ti: Sapphire laser which offers ultrafast laser pulse down to below 20fs and up to more than 30mJ. However, phase matching is not favor Ti: Sapphire in the X-ray regime. As mentioned above, there are several major contributions to the phase mismatch. With the refractive index being close to one for the X-ray regime. Those contributions of phase mismatch need to balance each other to make the refractive index of the driving laser to be as close to unity as possible.

Contribution from neutral atoms scales inversely with wavelength such that $\Delta n_{atoms} \sim 1/\lambda^2$ which electrons contribution scales quadratically with the laser wavelength $\Delta n_{electron} \sim -\lambda^2$. At long infrared wavelengths, the plasma refractive index is large and hard to get balance by the atom contribution such that very high pressure and low ionization level is required to reach optimal phase matching. The low ionization level usually needs to be achieved by loosely focusing the laser beam. For this reason, even though the Ti: Sapphire laser can be with a combination of short pulse duration and high pulse energy, its high harmonic is hard to reach an X-ray regime because the process wasted the possible high peak intensity that can boost the ponderomotive energy U_P and cannot get high ionization potential.

2.2.3 Quasi-phase matching using periodic physical structures and all-optical light structures

For IR-driven high harmonic generation, the ionization is limited to a low level. Otherwise, the plasma dispersion will be too big to be balanced whatever the gas pressure. The laser-dependent critical ionization level is derived as:

$$\eta_{CR}(\lambda_L) = \frac{1}{\frac{\lambda_L^2 N_a r_e}{2\pi\Delta\delta(\lambda_L)} + 1} \tag{2.33}$$

With the phase-mismatch condition, there will be also HH yield but the HH emission builds up periodically over a coherence length. Also, the signals are with different phases and thus are not able to add up efficiently as Fig 2.7.

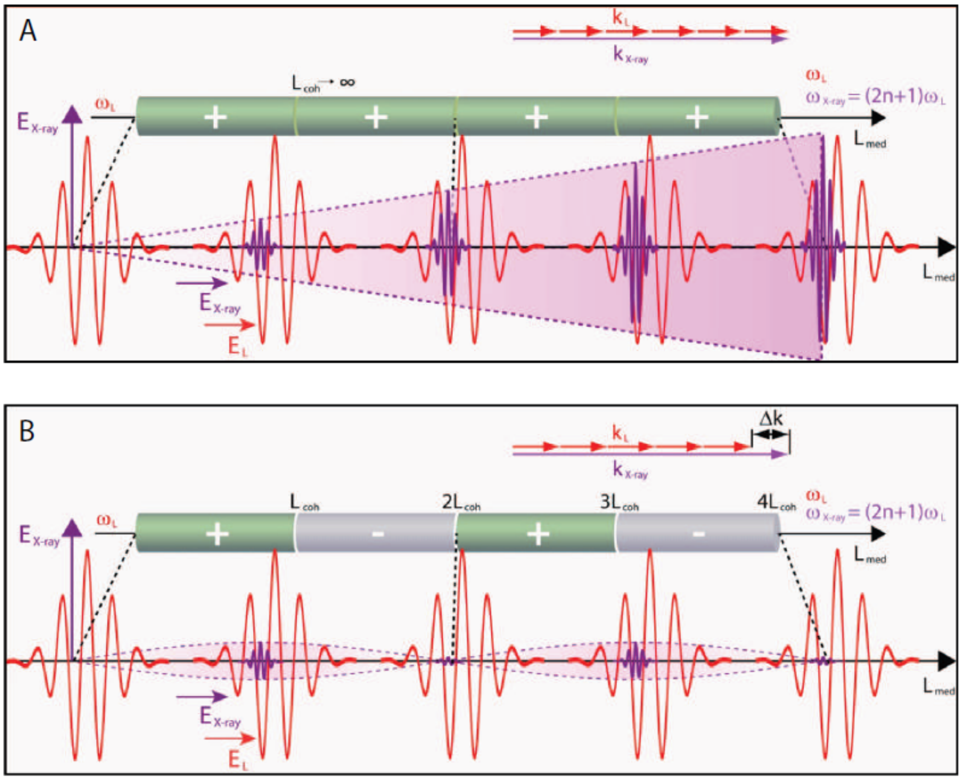

Figure 2.7. A) When the HHG is phase-matched, the HH signal grows linearly with the medium length theoretically. (B) Without phase-matching, the HH signal periodically oscillates on the scale of one coherence length. Graph from Tenio Popmintchev

Quasi-phasematching for low-order harmonics is proposed in 1962[4]. By introducing a periodicity of the nonlinearity to the nonlinear medium corresponding to the coherence length. Where the coherence length is defined as the distance that the fundamental and signal light to be out of phase by π. The generation of HH most of the time requires to be in a gas medium such that this initial method cannot be directly applied. But an analog method can be achieved. For example, the basic idea remains the same, the QPM can be achieved by restricting the HHG to be at the position where the HH signal can be added up constructively. Or equivalently, suppress the HHG at the out-of-phase zones. The idea can be illustrated in Fig 2.8.

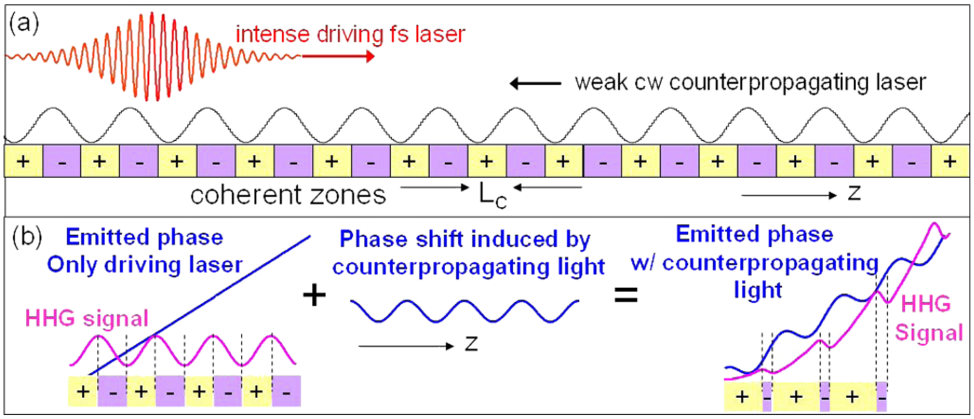

Figure 2.8. All-optical grating-assisted quasi-phase matching approach [48]. Where different zone can be separated.

3.2.2.1 modulated waveguide

A modulated hollow core waveguide as shown in Fig 2.9 can be used to periodically modulate the driving laser intensity such that harmonic with higher energy can be efficiently generated even with a substantial ionization level[49, 50].

The QPM structure is also helpful to make the generation of isolated attosecond pulses possible. As the temporally longer driving laser propagates through a certain region, the ionization level increases over time. The phase-matching approaches are optimal when closer to the critical ionization over time. The HH signal is mostly emitted during this time window. The critical ionization level is higher for the QPM case such that it could be closer to peak of the pulse with optimal laser intensity. The time window could be much shorter and may limit the HHG emission within half-cycle of the driving laser.

With modulated waveguide, the generation of the coherent soft X-ray can be all the way to the ”water window” region up to 4.4nm corresponding to 282eV. The phase mismatch that is normally resent between the driving laser and HH can be partially compensated.

3.2.2.2 Series of Gasjet

There is also an approach to modulating the gas density by using a series of gas jets[51] as shown in Fig 2.10.

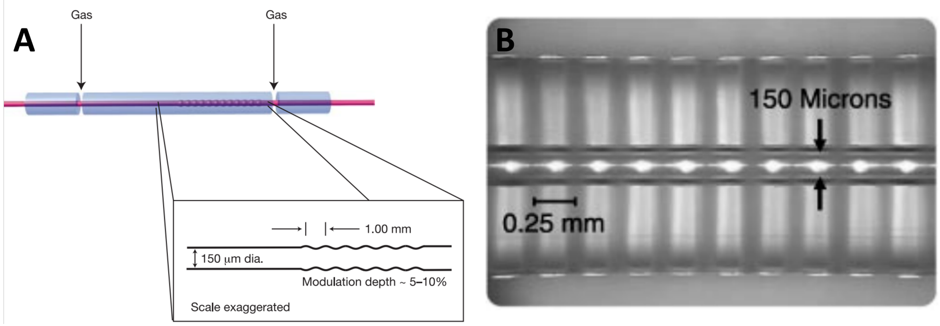

Figure 2.9. Mechanical solution, modulated waveguide[49, 50].

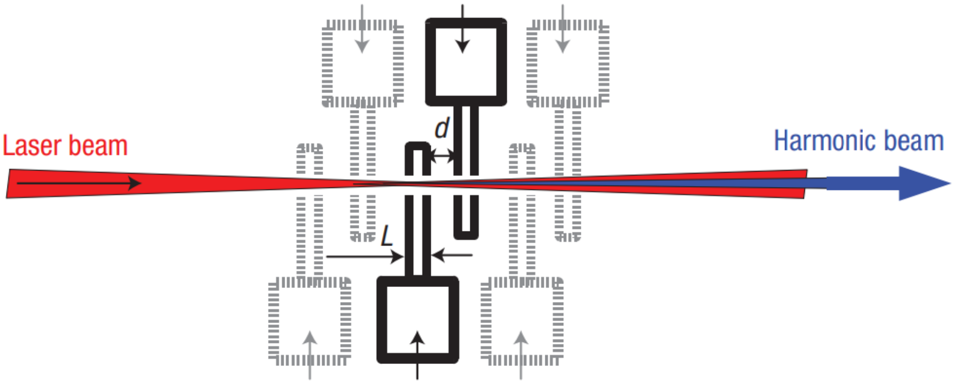

Figure 2.10. Series of gasjets[51].

All atoms are treated the same with the same single-atom emission amplitude. The phase mismatch is $z\Delta k$ grows linearly with z, the propagation distance. The q-th order harmonic intensity generated in a source of length L can be approximated as:

$$I_q \propto N_a^2 \frac{\sin^2(\frac{L\Delta k}{2})}{\Delta k^2} \tag{2.34}$$

Here N_a is the number of atomic dipole radiators driven by the laser. When dephasing is dominated by free electrons, the phase mismatch $L\Delta k$ scales with the density N_e of free electrons, $\Delta k \propto N_e \propto N_a$

$$I_q \propto \sin^2(L\Delta k/2) = \sin^2\left(\frac{\pi N_a}{2N_{a,q}}\right) \tag{2.35}$$

Here $N_{a,q}$ is the largest density that the q^{th} harmonic monotonically grows over propagation distance L. If N_a keeps growing by higher the gas pressure will decrease the HH yield from destructive interference of HH photons emission from the first half and the second half of the source.

The destructive interference can be shifted to higher N_a to boost the overall yield by dividing the total propagation length L into M sections. The M-separated sections can be shifted such that the phase difference of the exit of one section and the entrance of the next section is π at a given harmonic frequency $\omega_q = q\omega_L$

The optimized q-th harmonic at ω_q will be:

$$I_q \propto \frac{1-(-1)^M \cos\left(\frac{\pi N_a}{N_{a,q}}\right)}{1+\cos\left(\frac{\pi N_a}{M N_{a,q}}\right)} \sin^2\left(\frac{\pi N_a}{2M N_{a,q}}\right) \tag{2.36}$$

This modification allows M times of atomic density and M^2 times of HH yield.

3.2.2.3 Counter-propagating Laser Field

All-optical QPM[52] can also use a train of counterpropagating pulses to modulate the nonlinear index of refraction of periodic regions in a short waveguide as shown in Fig 2.11. The enhancement can be more than 10 times for some selected harmonics. Or can be more than 300 times by using three counterpropagating pulses in a long waveguide. The short and long trajectories also behave differently to these counterpropagating pulses and the enhancement could be selective by adjusting the counterpropagating pulse intensities.

It is possible that in the future, the quasi-phase matching technique could enable the HHG in the full X-ray absorption length to escalate the HH yield further.

2.2.4 Effective phase matching in the Soft and Hard X-ray regime in multiply charged plasma using Visible and UV driving lasers

High harmonics are generated at very high laser intensities which will generate laser-induced plasma, this plasma-induced phase mismatch limits the useful flux at the highest photon

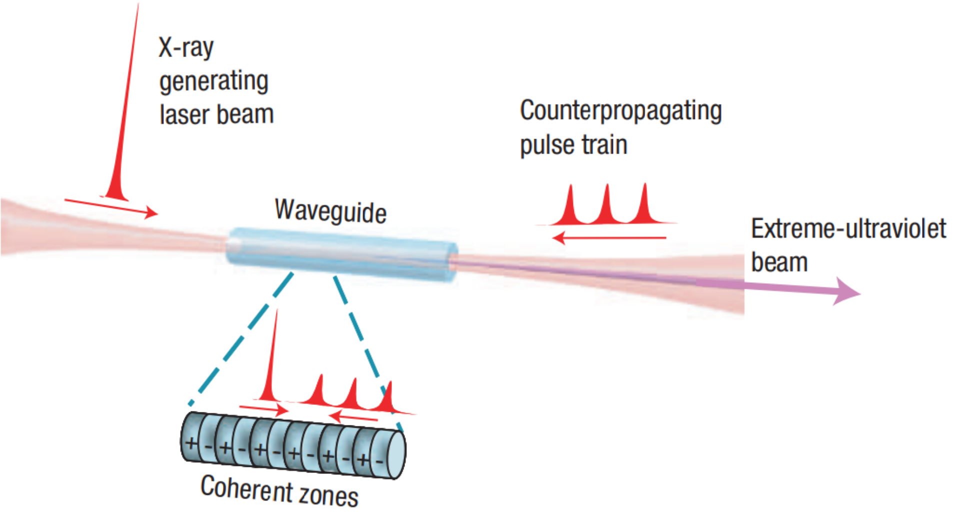

Figure 2.11. Counter-propagatig pulse train[52] .

energies in the soft X-ray region of the spectrum. Solving this ionization-induced phase mismatch becomes a critical challenge to the further development of coherent EUV and soft X-ray sources. And there is a surprise from UV-driven high harmonic[53] which can trace back to the late 80s when the high harmonic is discovered by using a 248 nm driving laser[1]. But now, the newer study gives a better understanding of the behavior and its physics.

Different from the IR-driven case, where high gas pressure and loose focusing are required to have low ionization levels and a large number of emitters. The refractive index scale law mentioned in section 3.22 is in favor of UV spectral range as a HH driver. The neutral atoms(Δn_{atoms}) and multiple ionized ions(Δn_{ions}) can provide larger dispersion than the IR case. And the plasma contribution is smaller and thus easier to be balanced as shown in Fig 2.12. HH can be emitted from an ion instead of a neutral atom thus gaining higher I_P, the ionization level can be much higher than 100%. Previous work claimed the efficient cutoff high harmonic emission could be from all the way to Ar^{5+}[53]. In the experiment, the UV-driven harmonic was also able to tolerate a much bigger range of gas pressure with efficient emission and a much bigger range of peak intensity which also creates a great condition to quantitatively study the ionization behavior in different regimes and probe possible novel electron correlation effects.

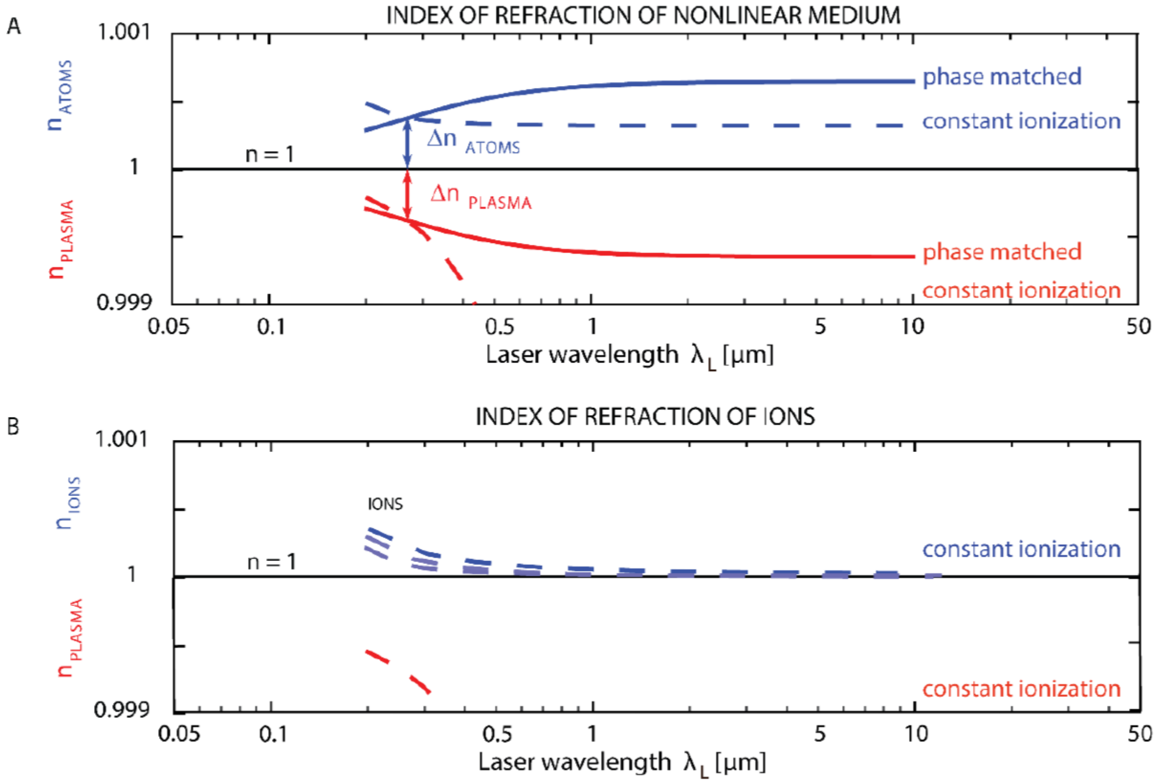

Figure 2.12. (A). Index of refraction of argon atom(blue-dashed) compared to the plasma refractive index(red-dashed) as a function of driving laser wavelength. For constant ionization level of 40%. The plasma refractive indices change much faster than the atoms. The solid lines show the refractive indices under phase-matching conditions near the HH cutoff. (B) The trend of ions' refractive indices. At shorter wavelengths, the ions' refractive indices start to change faster and easier to compensate for the plasma. Such a trend shows the HH phase-matching favors shorter driving laser wavelength. Graph from Dimitar Popmintchev

Chapter 3

Advance technology: design of ultrafast infrared/visible/UV laser parameters for efficient X-ray generation

Pulse duration is an essential driving laser parameter for efficient X-ray generation. It not only affects the possible highest peak intensity. It is also of vital importance for phase-matching. To get the highest yield and highest cutoff, the optimal condition is met when the temporal phase-matching window overlaps with the peak of the pulse. The pulse duration for most ultrafast lasers is limited by the gain bandwidth and cavity design. Ultrashort intense few-cycle pulses are mainly achieved by optical parametric pulse amplification and nonlinear compression. Post-laser operation aims at having a shorter laser pulse duration is a major task for building a robust high harmonic source.

3.1 Self Phase Modulation of infrared laser pulses in revolver-type anti-resonant fiber for the first time.

Pulse duration is limited by its spectral bandwidth. They shared an inverse relationship. Such that the first step is always to find a healthy way to broaden the spectrum. And with spectral broadening, the pulse could be compressed to near-transform limited pulse duration by canceling the chirp. Successful compression using noble-gas filled fiber can reach down to sub 2 cycle[54]. Here we are using a revolver-type anti-resonant fiber[55, 56] which offers low transmission loss and very efficient guiding with rather simple. The structure is shown in Fig 3.1. The anti-resonant effect is from the interference of the reflected waves from the inner and outer annulus interfaces. The advantage of using fiber for spectral broadening is that the high intensity can be reminded for long propagation length within the fiber with a well-defined guiding mode such that the nonlinear phase could quickly accumulate. Instead of long fiber, we used an 11cm long revolver-type antiresonant fiber

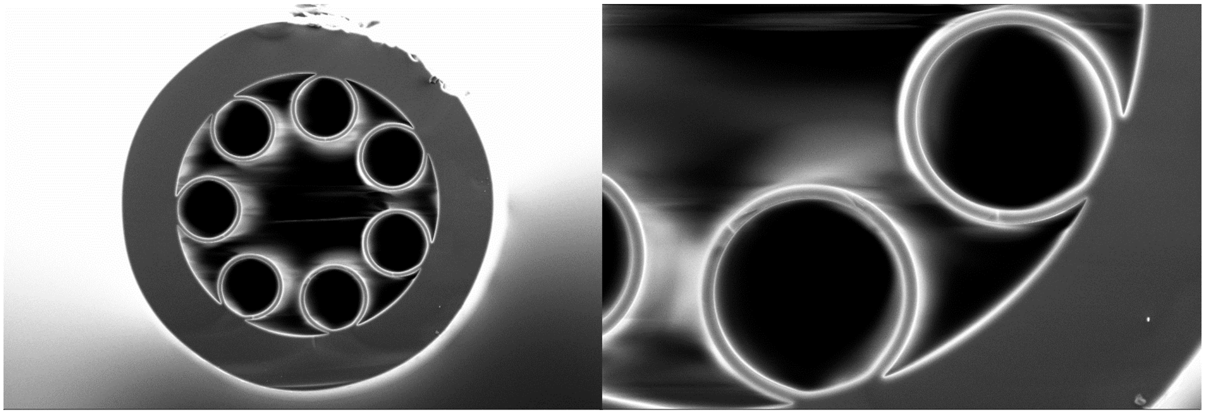

Figure 3.1. SEM image of antiresonant fiber. The fiber consists of seven annulus-type anti-resonant interfaces. The fiber is with outer diameter of 120μm and an inner diameter of 88μm, the center hollow zone is with a diameter of 42μm. The revolver is with an outer diameter of 23$\pm\mu$m and the revolver wall with a thickness of 1.25μm. All dimensions with a tolerance of 2% of its principle value. Graph from Prof. Mariusz Klimczak from the University of Warsaw.

Instead of using meter-long fiber with an injection of noble gases. We here only used a short segment of fiber(11 cm) filled with atmospheric air, we were able to broaden the spectrum by four times from the Fourier-transform limited(FTL) pulse duration of 220fs of the laser down to 56fs as shown in Fig 3.3. With a single-stage prism compressor, we were able to compress the pulse down to 68fs measured by Second Harmonic Generation Frequency Resolved Optical Gating(FROG), the experimental and retrieved trace is shown in Fig 3.4. The total compression efficiency is 66%.

The successful compression by using such an easy setup(Fig 3.2) shows its great potential. Future optimization could be filling the fiber with argon gas which has much higher nonlinearity than air such that a shorter fiber could be used to enhance the throughput.

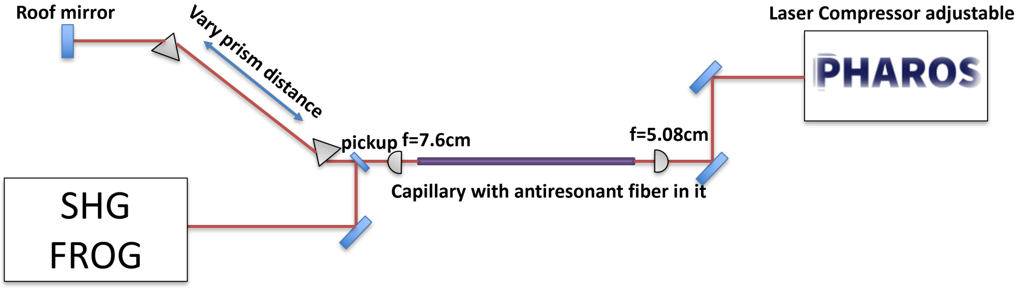

Figure 3.2. Single stage laser pulse compression using air-filled antiresonant fiber and prism pair compressor.

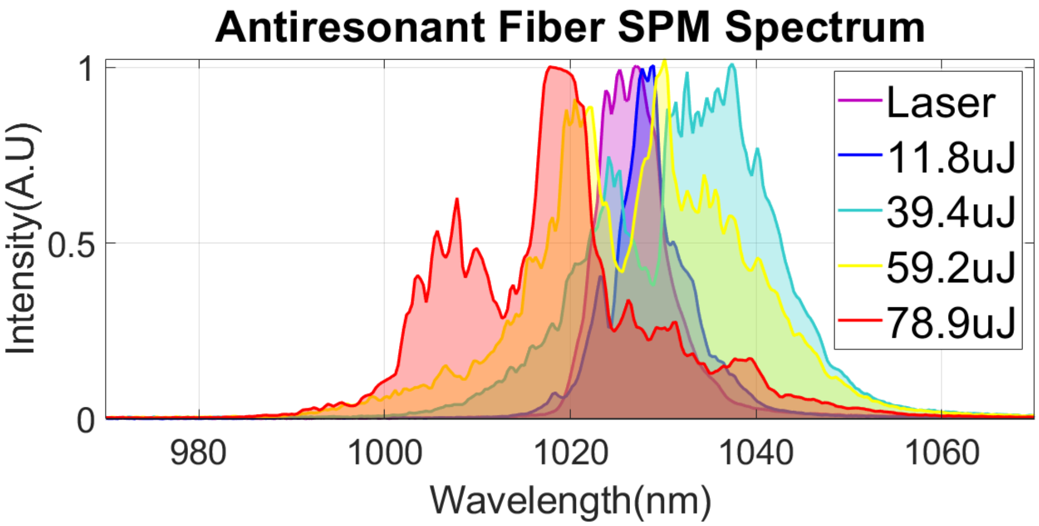

Figure 3.3. Spectral phase modulation of different laser pulse energy after propagation in an 11cm long antiresonant fiber. The Fourier transform-limited pulse duration of the broadest spectrum goes down to 56fs. The laser is initially with a pulse duration of 250 fs.

3.2 Self Phase Modulation of visible laser pulses in the thin plate/periodic Kerr medium

3.2.1 Abstract

We present a single-stage compression technique for the second-harmonic pulses at 515 nm in the visible spectral range, generated by a 1030 nm Yb-based sub-picosecond regenerative amplifier. Using a multi-plate arrangement, we demonstrate compression from 180 fs to 40 fs with a high efficiency of spectral broadening greater than 95% and a compression efficiency of 75%.

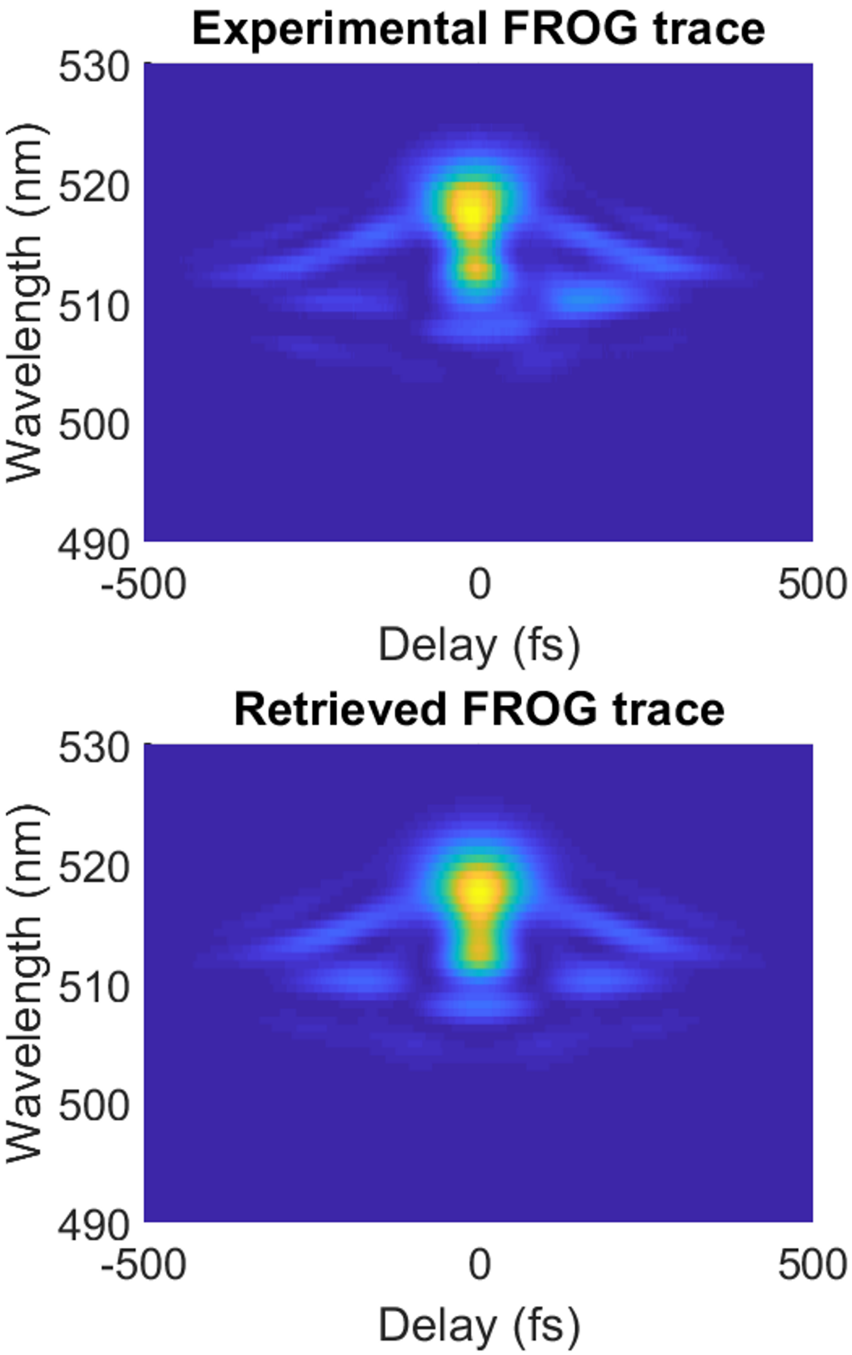

Figure 3.4. The SHG-FROG trace shows typical signs of compression.

Utilizing a low nonlinearity medium provides a straightforward and reliable approach to achieve shorter pulse durations (20 laser cycles) while preserving superior spatial beam quality with 97% of the energy concentrated in the central Arie disk. Additionally, the method simultaneously improves the temporal pulse quality without introducing a femtosecond-to-picosecond pedestal. The resulting enhanced laser parameters are crucial for extreme nonlinear optics applications and ultrabright EUV and X-ray high-harmonic generation, due to the short wavelength of the driving laser and the high repetition rate of 100 kHz to 1 MHz.

3.2.2 Introduction

Fully coherent light with ultrashort wavelengths and pulse durations is essential to study the ultrafast dynamics of atomic, molecular, and plasma systems, nanomaterials, and biosystems. EUV sources based on the process of high-order harmonic generation have gained their status quo in the field through the upconversion of near-infrared pulses from femtosecond Ti:Sapphire lasers, optical parametric amplifiers, and optical parametric chirped pulse amplifiers with high energy and high peak power. While, in general, high harmonic generation typically requires high peak power to reach high cutoff photon energy and record efficiency greater than $10^{-3} - 10^{-7}$ using UV - to - mid-IR drivers [1-3], a post-compression technique to further shorten the laser pulses at shorter UV - VIS laser wavelengths in the time domain are in demand. Several successful approaches have been demonstrated to date where femtosecond pulses at the fundamental near-infrared wavelengths of Ti:Sapphire or Yb-based lasers or optical parametric amplifiers derived from them have been compressed to several cycles in duration[57, 58, 59]. However, a practical spectrally broadening and compression scheme of UV-VIS laser pulses at very high average power has not been utilized. Also worth noticing is that conventional high harmonic generation drivers are usually limited to low repetition rates of up to a few kHz, while many EUV – X-ray imaging and spectroscopic applications can greatly benefit from a high repetition rate, high-flux source.

In this work, we demonstrate the capability of a kHz-to-MHz Yb:KGW sub-picosecond amplifier at 1030 nm to be utilized for highly efficient high harmonic generation in the EUV region by spectrally broadening and compressing its second harmonic at 515 nm. The advantages of high harmonic generation in gases driven by short-wavelength VIS lasers are extremely high single-atom efficiency due to low quantum diffusion of the rescattering electron, ultra-narrow linewidths of the harmonics due to broader temporal phase-matching window, enhanced phase and group-delay matching due to high linear and nonlinear indices of refraction of atoms and ions [1, 2]. In addition, the superb spatial coherence and, finally, an extended X-ray cutoff with intrinsically-compressed near-transform limited attosecond pulses make this technique very attractive for high-resolution dynamic imaging and for angle-resolved photoemission spectroscopies [1]. It is also worth noting that high harmonic generation inside a noble gas-filled capillary could benefit from self-confinement in both space and time. We demonstrate a near spatio-temporal solitary mode of propagation in periodic thin-plate media at VIS laser wavelengths and achieve spectral broadening via self-phase modulation (SPM) while maintaining an extremely good spatial profile of nearly-identical spot sizes and similar pulse durations at each plate. This eliminates the strong conical emission loss and enhances the efficiency of the pulse broadening geometry to above 93%, resulting in compression from 180 fs to 40 fs at 515 nm, or 23 cycles at FWHM with post-compression 42µJ pulse energy. This pulse duration is in the optimal range for effective phase matching of high-order harmonic generation using UV-VIS drivers. Post-laser pulse compression is done by compensating the chirp of the spectrally broadened pulse such that the pulse duration of the laser light can be further shortened.

3.3 Spectral Broadening in Low Nonlinearity Multi-Plate Geometry

Self-phase modulation modifies the spectral property while the laser pulse propagates in material with laser-induced third-order Kerr nonlinearity $\chi^{(3)}$. Such that the index of refraction changed $n(t) = n_0 + n_2 I(t)$. Here, we choose Calcium Flouride CaF$_2$($n_2 = 1.9210^{-16}$cm^2/W). Here I(t) is the laser intensity. The nonlinear accumulated phase, often referred to as B-integral, can be evaluated as:

$$B(t) = \frac{\omega_0}{c}\int_0^L n_2 I(z,t)dz \approx \frac{\omega_0}{c} L n_2 I(t) = \frac{2\pi c}{\lambda} L n_2 I(t) \tag{3.1}$$

Here ω_0 is the initial circular frequency, c is the speed of light and L is the thickness of the media. This nonlinear phase results in a frequency shift:

$$\Delta\omega(t) = \omega(t) - \omega_0 = -\frac{\partial}{\partial t}B(t) \approx \frac{\omega_0}{c} L n_2 \frac{\partial}{\partial t} I(t) \tag{3.2}$$

The intensity slope of the laser field controls the maximum frequency change. In principle, tight focusing can produce the biggest spectral broadening. However, for pulse compression, the use of spatial-temporal solitons induced by propagation is preferred. Although there is an accumulation of B-integral and chirp due to media properties, the use of chirp compensation optics can compress the pulse to a duration close to the Fourier transform limit with a small amount of unbalanced dispersion of higher order. However, the spectral broadening process can also cause temporal splitting of the laser pulse, or the media can greatly reshape the temporal and spatial profile of the laser, making it difficult to compress using standard commercial chirp compensation optics efficiently. To avoid temporal splitting and strong spatial deformation, we use thin plates of solid material of Calcium fluoride with 111 cuts. This also provides smaller dispersion compared to commonly used materials such as sapphire or fused silica. Group velocity dispersion (GVD) and third-order dispersion (TOD) are the two major terms that contribute to chromatic dispersion and can be easily evaluated[60]:

$$POD(n) = \frac{\partial^p}{\partial \omega^p} k(\omega) = (-1)^p \frac{1}{c} (\frac{\lambda}{2\pi c})^{p-1} \sum_{m=0}^{p} \mathcal{B}(p,m) \lambda^m \frac{\partial^m}{\partial \lambda^m} n(\lambda) \tag{3.3}$$

Such that the GVD and TOD at central wavelength 515nm is 48.619fs2/mm and 16.744fs3/mm, respectively.

A single thin plate can achieve large spectral broadening by tight focusing, however, accumulating a significant nonlinear phase usually leads to a conical emission with an Arie ring pattern causing substantial energy losses. The formation of single or multiple filaments inside the solid material leads to severe beam distortions or beam splitting. Alternatively, a larger beam waist can reduce the fast nonlinear phase accumulation per plate with a weaker self-refocusing, thus, a considerable spectral broadening can be achieved using a soliton-like propagation in a set of multiple thin plates.

One fascinating occurrence associated with filament propagation is the refocusing cycle of the laser. During laser filamentation, the beam rapidly shrinks down and expands, leading to a continuous series of divergence and refocusing that can persist over long distances. The formation of filaments generates a plasma that transforms a narrowband laser pulse into a broadband pulse, opening up new possibilities for applications. An intriguing feature of this plasma, induced by filamentation, is its ability to restrict the density of electrons, thereby averting optical breakdown. In a medium with a Kerr nonlinearity, the following simplified formula can be used to estimate the focal length:

$$f_c \approx \frac{\pi w_0^4}{8 n_2 P l} \tag{3.4}$$

where w_0 is the beam is the refractive index of the medium, λ is the wavelength of the laser beam, ω_0 is the beam waist at the focus, n_2 is the Kerr nonlinear coefficient of the medium with length l, and P is the optical power. This formula shows that the focal length in self-focusing is proportional to the initial beam waist inversely proportional to the nonlinear refractive index of the medium and the laser beam power. In our experiment, the distance between the plates is set to approximately $2f_c$, where f_c varies on each plate. This translate to a critical phase of $b_c = \frac{4}{\lambda} n_2 (\frac{2E_c}{t_p w^2})$. Where E_c is the pulse energy, t_p is the pulse duration and w is the beam radius.

In our experiments, a Yb:KGW laser amplifier of 8 W average power, with a tunable repetition rate between 100 kHz and 1 MHz, and 250 fs pulse duration, is used to generate second harmonic pulses in a Type I BBO crystal with a high conversion efficiency of more than 67%. The 515 nm beam of 56 μJ energy per pulse (at 100 kHz) and shorter 180 fs pulse duration due to the nonlinear intensity dependence is then focused by a long focal length lens of F=1 m, ensuring a long Rayleigh range of more than 15 cm. Eight CaF2 thin plates of 1 mm thickness are chosen to be the Kerr medium, equally spaced by 2 inches, and are used for spectral broadening, with the first plate placed right at the flat wavefront of the beam in focus. The plates are placed at alternating Brewster angles to minimize the reflection loss and minimize any asymmetries. Furthermore, the precise [111] CaF2 crystal cut eliminates any depolarization degradation and energy loss since CaF2 is known for wavelength-dependent depolarization issues in white light generation for other orientations[61]. Also, the plates are placed in a counter-rotating configuration, shown in Fig.3.5 to compensate for wavefront distortion. Prism pair compressor as a transmission optics could also induce dispersion to intense short pulse such that the beam size that sends into the prism pair better to be as big as possible to minimize this unwanted dispersion.

3.4 High-Performance Laser Pulse Compression with Enhanced Spatial and Temporal Quality

Many nonlinear effects are due to third-order susceptibility such that the spatiotemporal propagation of intense laser light in media is hard to control towards the desired direction. In this work, we experimentally maximize the utilization of SPM and self-focusing. Each plate contributes to the spectral broadening and provides similar self-focusing to maintain the spatial soliton propagation. The beam size on each plate is measured using 2f-2f imaging, and it remains 350±10 μm. Pulse duration after each plate is also remaining similar, around 200±10 fs. The pulse enters a spatial-temporal soliton mode that supports spectral broadening without splitting. The B-integral for each plate should be identical, and each plate contributes to the spectral broadening.

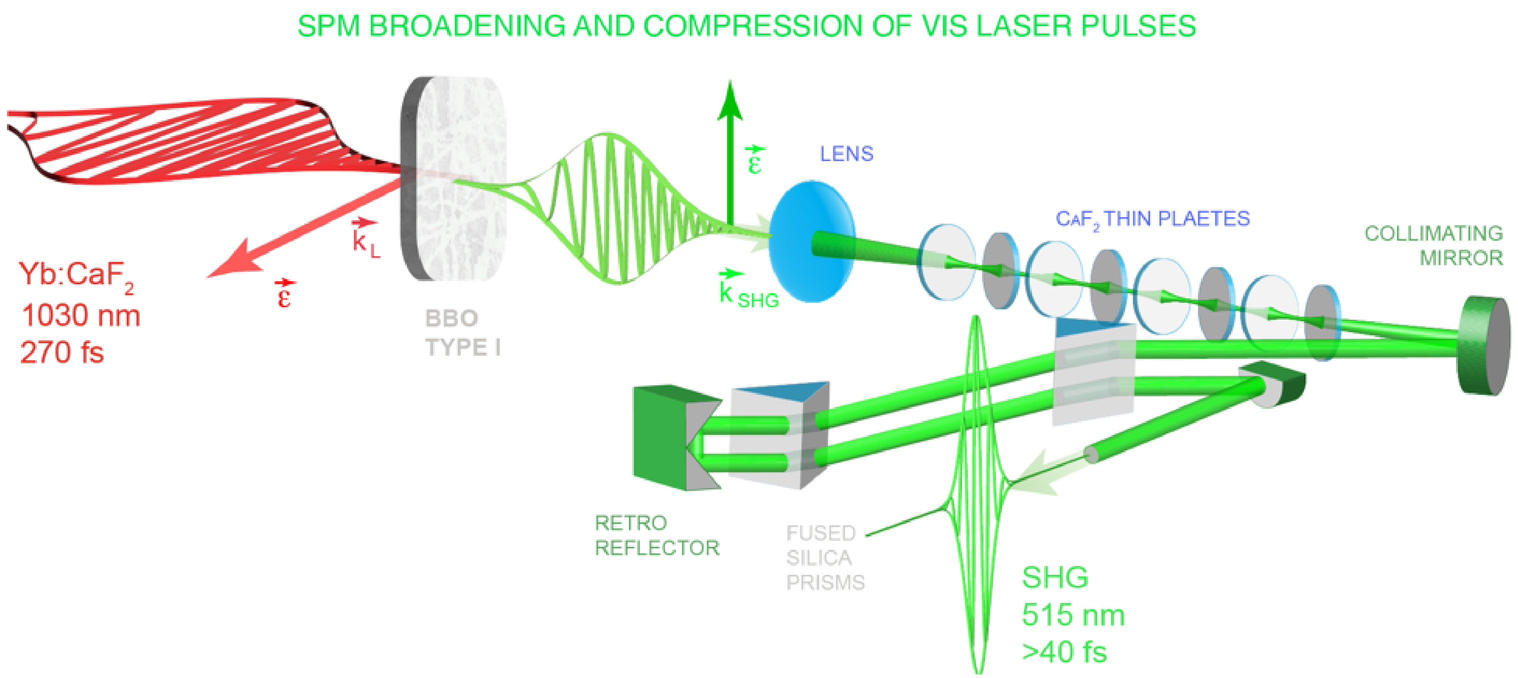

Figure 3.5. Schematic of a single-stage spectral broadening and compression of ultrafast VIS 515 nm laser pulses using thin plates with low nonlinearity. Experimental setup: high power 8 W, 250 fs, near-IR laser pulses amplified in a 1030 nm KGW regenerative laser amplifier are upconverted with 70% efficiency to its second harmonic of 5.6 W, 180 fs, 515 nm pulses in a BBO crystal. The VIS pulses are spectrally broadened in an array of thin CaF2 plates with low nonlinearity in alternating Brewster angle geometry, with a high 93% efficiency, then compressed using a prism-pair compressor to sub-40 fs in an excellent Gaussian beam with 78% efficiency. The overall efficiency is 75%.

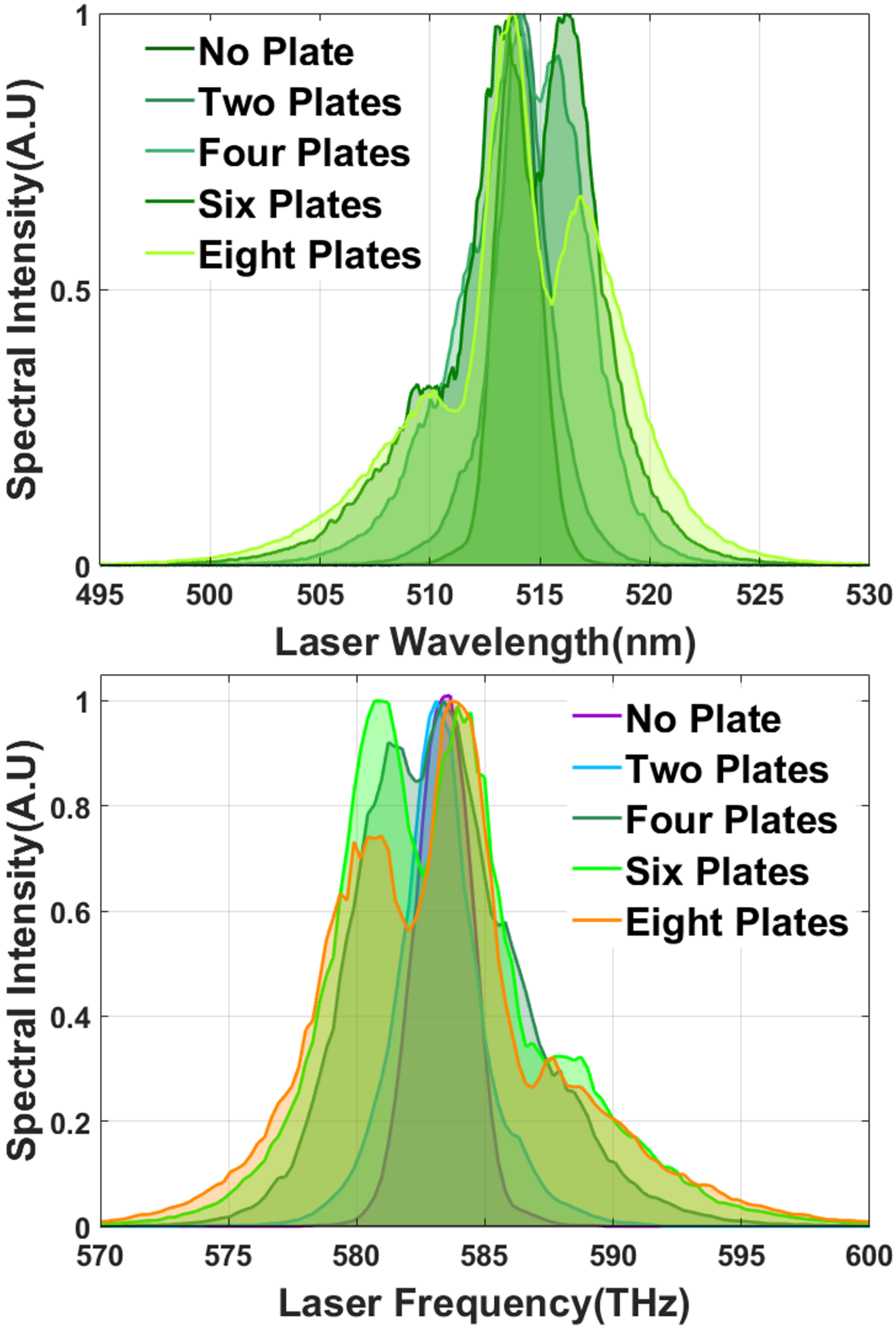

Figure 3.6. Spectral broadening through nonlinear spectral phase modulation after plates. Top: wavelength domain. Bottom: frequency domain. This is the first effective spectral broadening for visible laser light.

For dry air experiments, the gas environment plays an important role, while its nonlinearity is smaller compared to solid materials. Soliton mode propagation in a vacuum with controlled pressure and gas species is expected to fine-tune of the dispersion of the SPM setup. Atomic and molecular gases with either polarization properties or much higher nonlinearity can be used to fine-tune the spectral broadening and optimize the spatial-spectral-temporal beam quality.

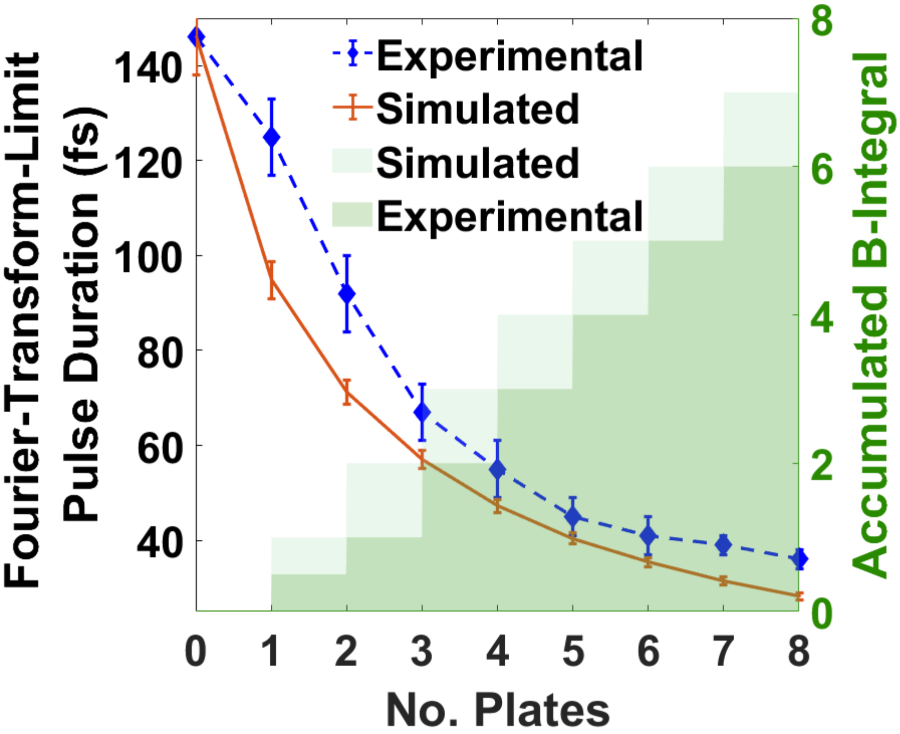

Figure 3.7. Fourier Transform Limited (FTL) pulse duration after each plate. Accumulated nonlinear phase and corresponding B-integral after each plate. Here we simulate the case of periodic soliton mode with $b = 1$.

Chirp decides how far away the laser pulse is from its Fourier-transform limited pulse duration. FROG, as a characterization tool, is able to retrieve the spectral phase information such that it offers a guide on the amount of compensation needed for different order dispersion. Here we did an analytical calculation to optimize the dispersion compensation such that we can cancel the second while minimizing the third-order dispersion[60].

The fused silica prism pair compressor with a 70 cm tip-to-tip distance is able to compensate for the needed dispersion that yields a sub-40 fs pulse with superb spatial-temporal quality. The loss focusing near spatiotemporal solitary mode also offers a chance for post-laser compression for high pulse energy laser. The SPM for ultrafast laser with high pulse energy could be problematic with a single lens such that it could accumulate too much nonlinear phase or the focal length is relatively long and needs a vacuum environment for pulse propagation to reduce distortion in the air. The near spatiotemporal solitary mode suggests instead of focusing the laser beam, one can down scope the laser beam by using a pair of positive and negative lenses. The designed beam size on plates and the periodic spacing between plates depend on the critical phase on each plate that makes the soliton propagation possible.

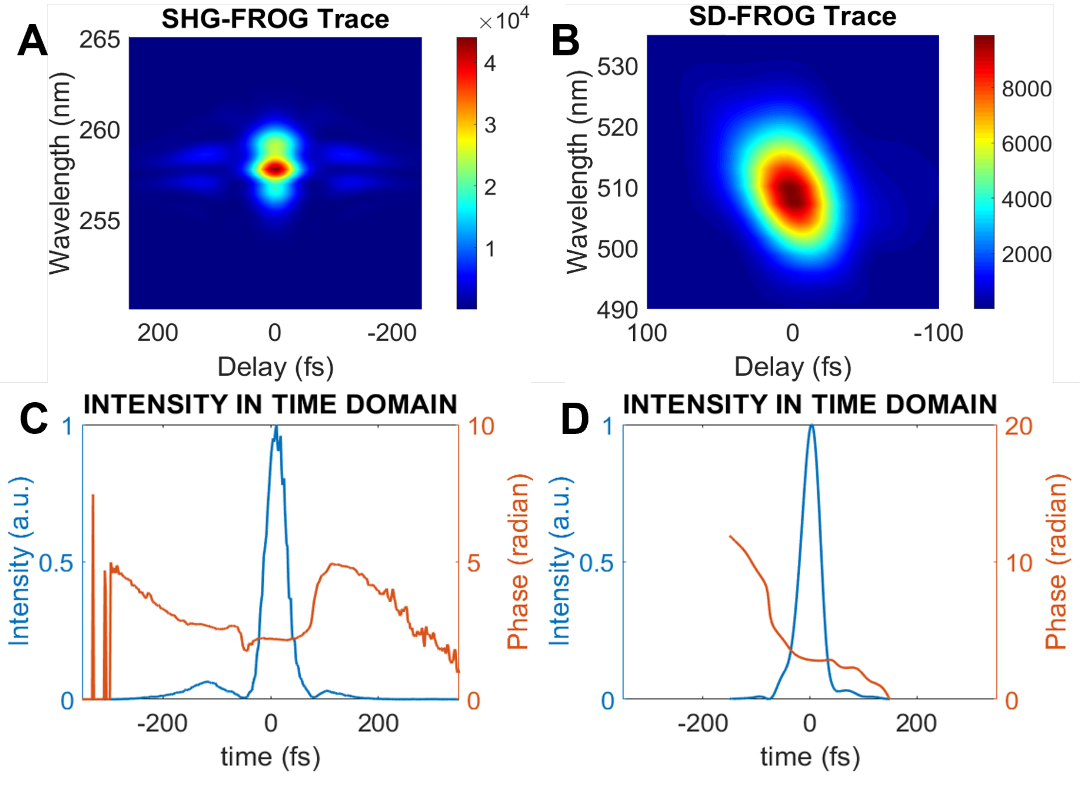

Figure 3.8. FROG measurement of the compressed pulse. A and C: SHG-FROG measurement. B and D: SD-FROG measurement. For the first time, we were able to use this method to compress pulsed visible laser to be 4.5 times shorter.

3.5 Ultrabright High Harmonic Generation Using Short-Pulse Short-Wavelength UV-VIS Lasers

Yb-based lasers gained high popularity in academic research and industry in the last decade. The extreme nonlinear process, including secondary light sources based on high harmonic generation, also benefits from its scalable high repetition rate, high power, and high stability. Recent understanding demonstrated that using a shorter wavelength laser driver can greatly enhance efficiency[53, 62, 63]. The single atom yield of high-order harmonics in different configuration scales from λ^{-5} for the most gas jet to even $\lambda^{-7.5}$ for the phase-matched case. That, by shortening the driver wavelength by a factor of 2, the single atom yield is 32 to 512 times larger. Also, the plasma dispersion, which destroys the phase-matching for the long infrared driver, can be effectively compensated by the dispersion of ions in the UV-VIS spectral range as the resonances of atoms are approached. Essentially, the temporal phase matching window increases for UV-VIS drivers. So for UV-VIS-driven high harmonics, multiple 10-to-50 cycles, instead of ten cycles of the laser pulse, are able to generate harmonic efficiently. Compressing a long 180 fs second harmonic pulse in a single SPM stage instead of compressing the fundamental laser beam can yield a higher second harmonic conversion efficiency while greatly maintaining the laser quality, which plays an important role in an efficient high harmonic generation. Here, we calculate here the tunnel ionization that 515 nm laser could induce with the compressed pulse energy and duration. The ionization is directly ADK plot here.

Phase matching of high harmonic generation using UV-VIS drivers favors longer pulse durations since the temporal phase-matching window for efficient upconversion in the EUV – X-ray regime increases with the decrease of the laser wavelength. The demonstrated straightforward compression scheme provides a driver of 23-cycle pulse duration and a feasible peak intensity of $> 1.0 \times 10^{15}$W/cm^2 to reach the soft X-ray regime at 100 eV at repetition rates of 100 kHz and higher, i.e., more than two orders of magnitude greater compared to that of most of the conventional laser amplifiers. Theoretically, the emission can reach the technologically relevant

13.5 nm EUV wavelength with very narrow linewidths using Ar ions or neutral He (see Fig.3.9)

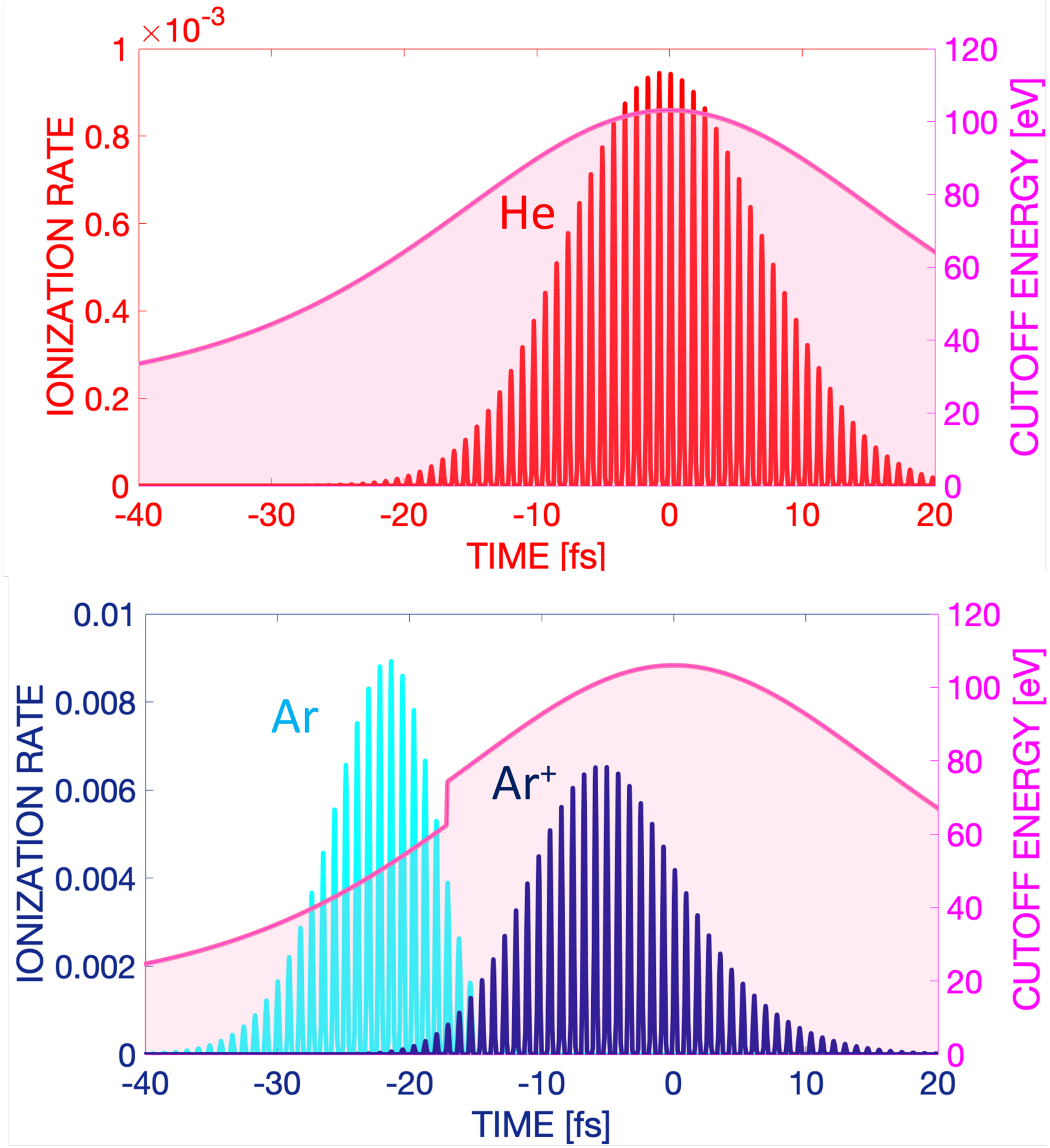

Figure 3.9. Theoretical high harmonic cutoffs at the technologically relevant 13.5 nm EUV wavelength (91.7 eV) for a 515 nm driver with a 40 fs pulse duration for an experimentally feasible peak intensity of 1.0×10^{15} W/cm^2 (ionization of Ar ions in blue and neutral He gas in red).

3.6 Conclusion

This work implements a straightforward method to generate short 40 fs VIS pulses at the second-harmonic wavelength of Yb-based laser amplifiers with kHz-to-MHz repetition rates. The resulting pulse has a high-quality spatial profile with 97% of energy in the central mode of the Arie pattern, excellent temporal quality without any pedestal, and high compression efficiency. These features make the single-stage scheme an appealing frontend for ultrabright attosecond high harmonic generation using VIS driving lasers.

Chapter 3, partially, is currently being prepared for the publication of the material High-performance compression of VIS 515 nm laser pulses for bright phase-matched EUV - X-ray high-order harmonic generation at kHz-MHz repetition rates, Siyang Wang, Jieyu Yan, Sirius Song, Alexander Atanassov, Zhihan Wu, Dimitar Popmintchev, Tenio Popmintchev. The dissertation author was the primary investigator and the author of this paper.

Chapter 4

Bright Coherent X-ray Generation Designs and High-Performance Spectrometer and Monochromator for EUV and X-ray Attosecond Pulses

4.1 Lego Hollow Waveguide Designs for Phase-Matching of Extreme High Harmonic Generation

The early trial of using hollow core waveguide on HHG was proposed and conducted in the late 90s[41, 64]. For low-loss telecommunication fibers, the light gets guided by total internal reflection with a high index of refraction core and a low index of refraction of cladding. Also requires a numerical aperture to match the launch angle and mode area. Hollow-core fiber does not really guide the laser light with a guided mode. By adding high reflective cladding such as the photonic bandgap fibers, the waveguide is able to guide light within the transmission window well. But hollow-core waveguide is with the advantage that the transmission window is very broad as shown in Fig 4.1. Compare to gas-jet. Hollow-core waveguide is for efficient High Harmonic Generation with usually 10 times less gas consumption and more than 10 times efficiency due to its advantage in phase-matching and longer distance for accumulation of signals. The High Harmonics spatial mode and spatial coherence from the waveguide are also much better and with smaller divergence.

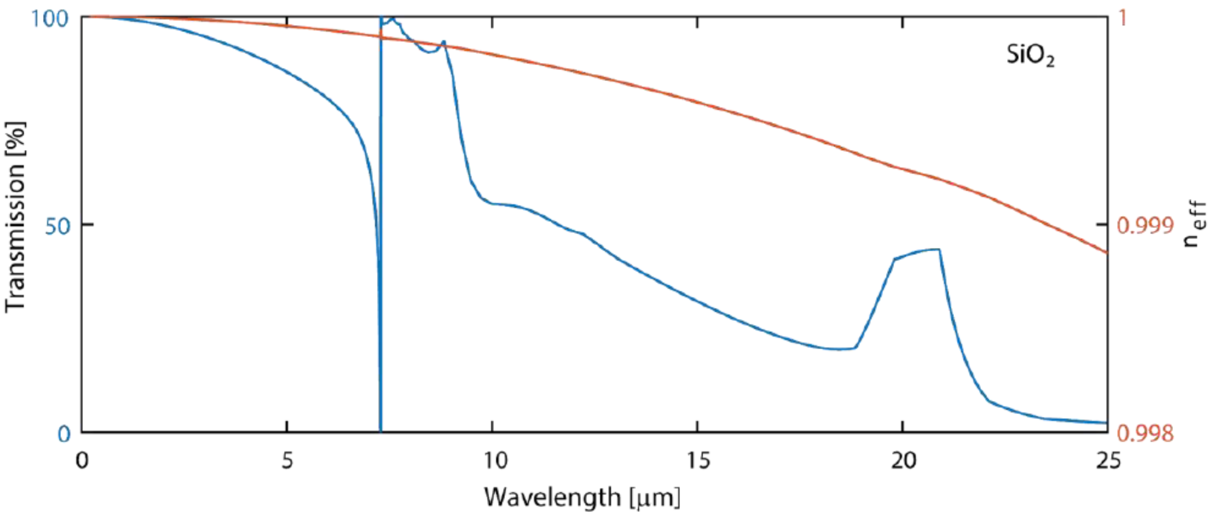

Figure 4.1. Transmission(blue curve) for the HE_{11} mode and effective mode index(red curve) of typical silicon-dioxide hollow core waveguide with radius of 200μm. Graph from Dimitar Popmintchev.

By drilling holes on the fiber's side surface, we can make gas-injected hollow-core fibers that can be used for HHG. Gas injection is of vital importance. For an efficient HHG, a steady-state gas pressure gradient between gas injection points and entrance or exit and a relatively stable constant pressure between gas injection points are wanted.

The complicated part is that we design no formation of melting and recast layers. A sharp and straight hole is wanted such that it can provide consistent gas flow and is easier to maintain pressure gradient. The finish requires parameters that can obtain a straight and clean trench with no thermal damage. The laser penetration depth has a positive correlation to the laser pulse duration $d_{penetration} \propto t_L^{1/2}$. And with shorter and shorter pulse duration, the penetration depth can be reduced to only one layer of molecules such that it will produce no residue and no melting to the deeper layers. Such a process can also be understood by classifying the time scale of different interactions. The photon-to-electron interaction is usually the fastest(within 10fs) and the electron-electron interaction is slower to be with a time scale of 100fs. The electron-to-phonon interaction is even slower roughly with a time scale close to 1ps. Then phonon-phonon interaction is the slowest usually within 100ps. If the whole machining process is faster than the time scale of phonon-phonon interaction then there should be no serious melting happening and the main process should be sublimation as shown in Fig 4.2. If the pulse duration has a timescale longer than heat diffusion time then the quality of the micro-hole edge would be hard to control. It also depends on what kind of process it is.

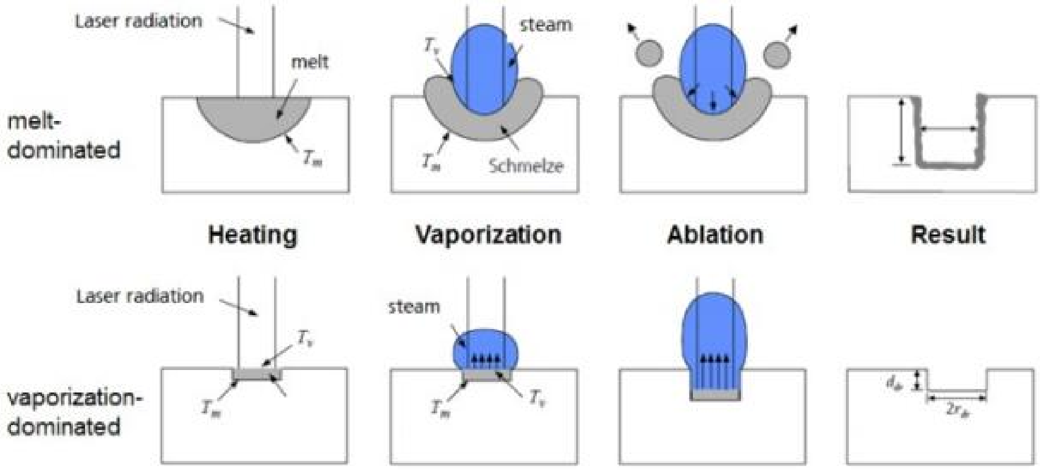

Figure 4.2. Melt or Vaporization dominated process. Adapted from[65]

The laser machining process often causes microstructure changes and induces defects such as forming a recast layer and cracks [65]. The solution to this is to use an ultrashort pulsed laser. From a laser material processor's point of view, the 'ultrafast laser' usually means a laser with a pulse duration below 10ps. Ultrafast Laser machinings technologies such as helical-drilling[66] and trepanning[67] have been developed for over a decade and have proven their ability in high-quality and clean drilling. Helical drilling can rotate the focal spot profile around the beam axis as shown in Fig 4.3 such that a round machining profile can be achieved without the need for aberration-free focusing.

We designed an ultrafast laser machining setup that guides 250fs laser pulse through flexible Kagome fiber(Beam Delivery System by GLO Photonics) into the scan head with a pair of Galvano. An F-theta lens with a focal length of 10cm enables us to do scanning and

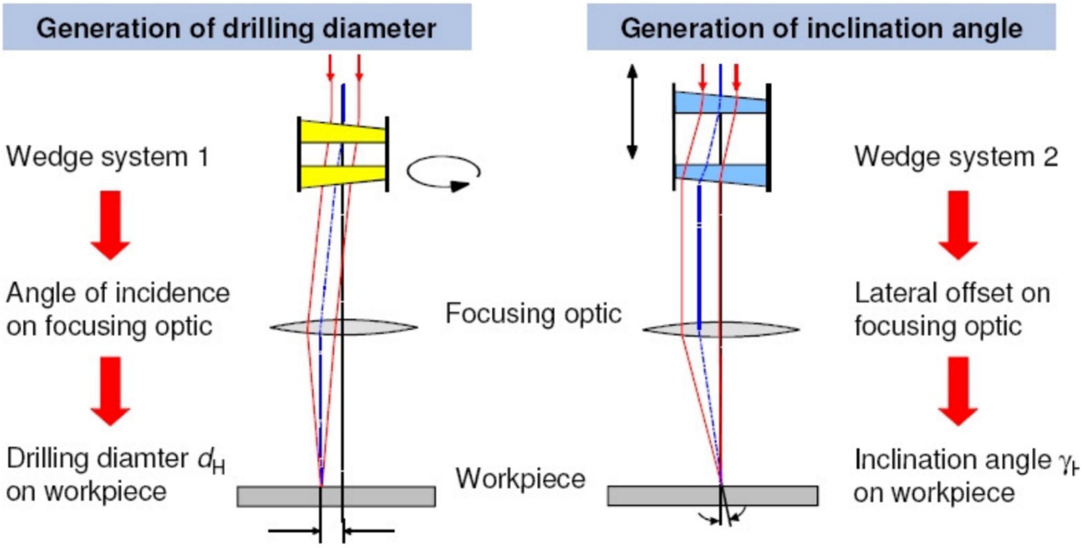

Figure 4.3. The optical principle of helical drilling. Adapted from [66]. Helical drilling is able to do self-rotation around the beam axis so it has less requirement for the laser focusing profile.

machining in a plane. By scanning the laser focus with a helical path, we were able to achieve drilling a clean hole. The setup is shown in Fig 4.4. By adjusting the focus plane and repeating the helical drilling we were also able to achieve a near-straight profile without damaging the other side of the capillary's inner wall.

The machining scan head is calibrated by using a chessboard and controlled by our custom-made software. By trial and error, we find the best recipe for drilling a sharp and clean straight hole as shown by Fig 4.5 in the fiber such that it could serve as the gas injection port. Double-side drilling is also done such that it can be used for a free-focusing gas jet(Fig 4.6) for HHG.

A multifunction waveguide host is designed for the drilled fiber such that it can provide a vacuum, visibility of the exit and entrance, stable gas injection ports, and ultra-stability in defining position. The vacuum is achieved by using low-outgassing UV-cured glue which seals the fiber from the gas injection ports. There are usually two gas injection ports to achieve near-constant gas pressure in between. The highest precision tolerances of the host define the

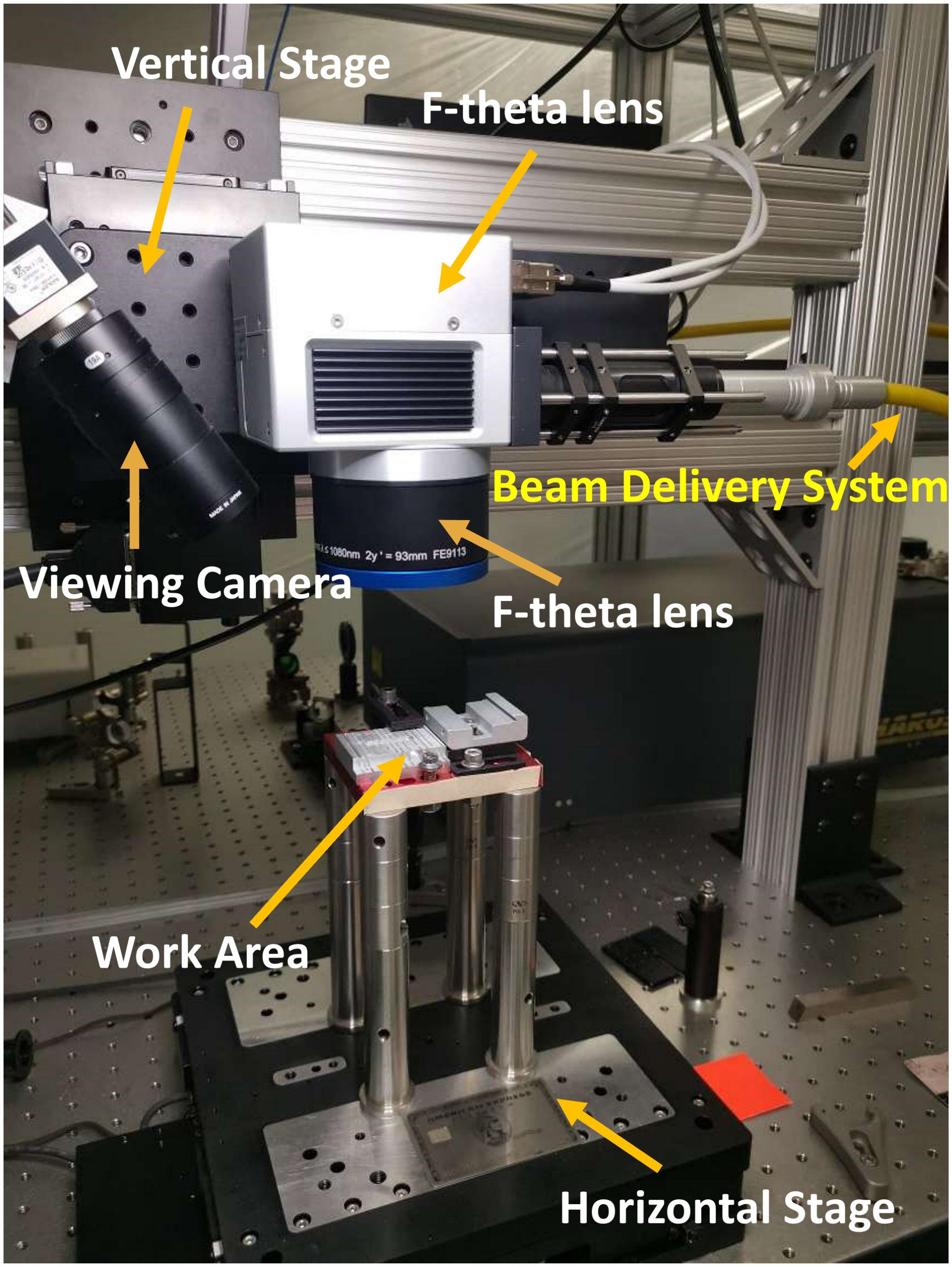

Figure 4.4. The ultrafast machining stage set-up.

fixed position of the fibers which makes the replacement and realignment of new fibers much easier.

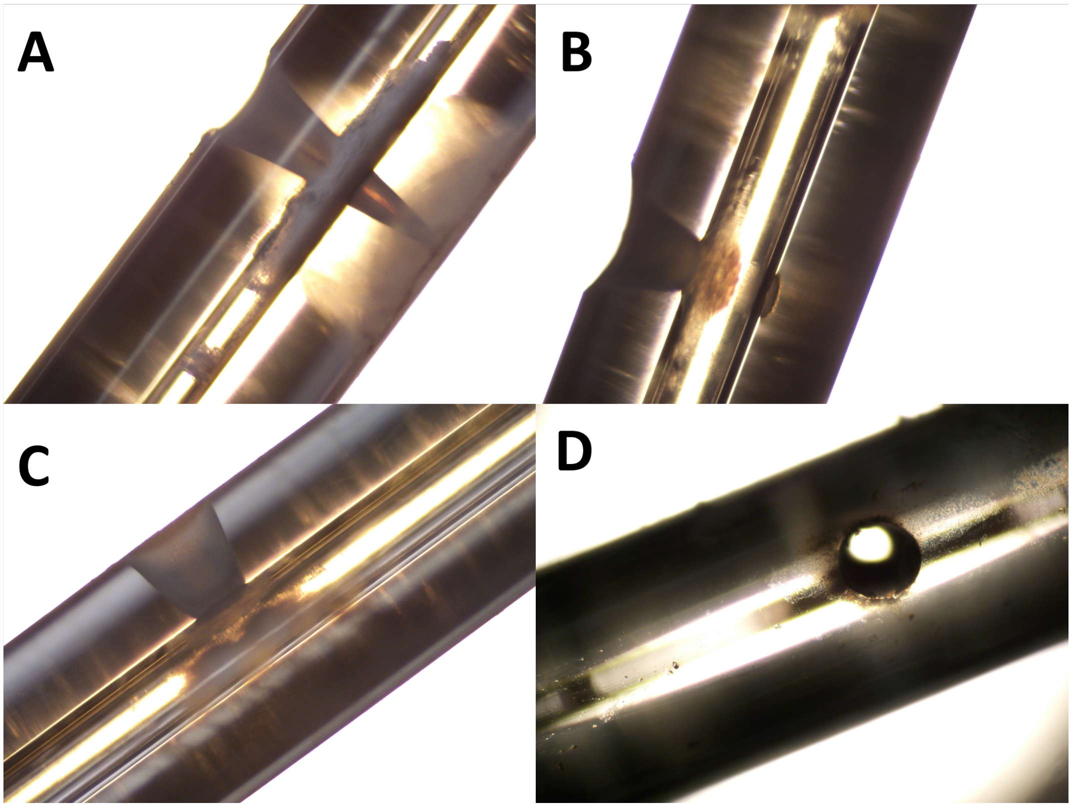

Figure 4.5. (A)Early result of fiber drilling that gives clean cone-structured hole. (B) Optimization with gradually shifting focusing position but the drilling went to the other side of the inner wall which could induce unwanted turbulence of gas. (C)Hole with the optimized procedure. (D) Eagle view of the drilled hole.

With well-defined constant pressure in between the gas injection points and pressure gradient at both entrance and exit, the phase matching condition can be found by tuning the gas pressure and laser focusing position.

The generation of X-ray HH photons usually requires a long interaction distance with stable gas pressure. This stable and big pressure-length product is sometimes challenging since the other part of the HH beamline needs to be vacuumed. Waveguide with well-controlled gas injection and differential pumping at both entrance and exit of the fiber would be the best solution so far.

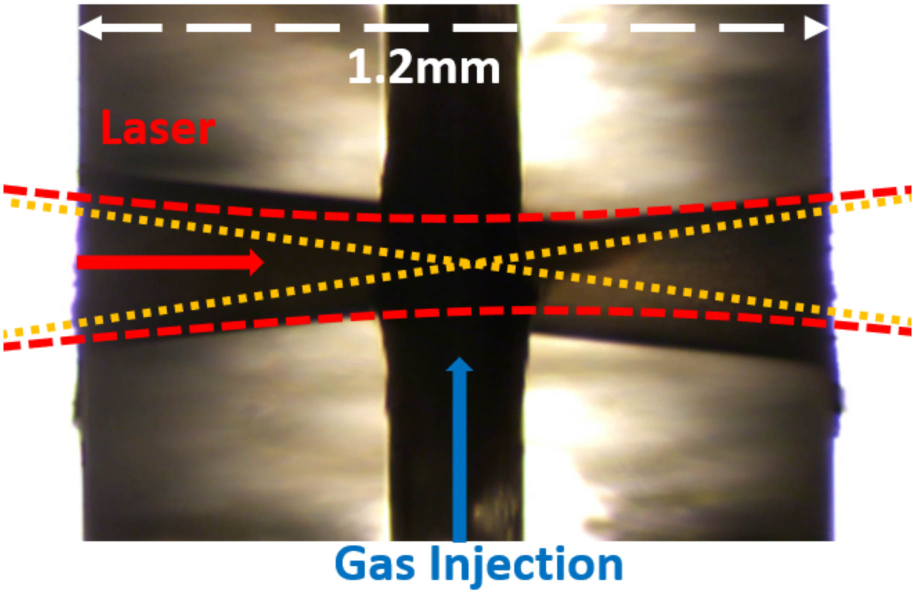

Figure 4.6. Pre-drilled hollow core fiber for high harmonic gasjet design.

4.2 Lego Design of X-ray Toroidal Mirror Focusing Optics

To design a spectrometer with good resolution, there needs focusing optics to image the X-ray source onto the detector. The common focusing optics for X-ray could be a pair of glaze incidence KB(Kirkpatrick and Baez) mirrors, placed perpendicular to each other. The two mirrors provide focusing in horizontal and vertical directions separately. We design here one optics focusing system by using a glace incidence gold-coated toroidal mirror. With five degrees of freedom of motion(2 linear and 3 rotational), this single toroidal mirror provides a one-to-one real image on the X-ray detector. The distance of the toroidal mirror to the source is the same as the distance to the detector which equals 2f where f is the focal length of the toroidal mirror. The toroidal mirror can be replaced by an ellipsoid which offers aberration-free refocusing as shown in Fig 4.7.

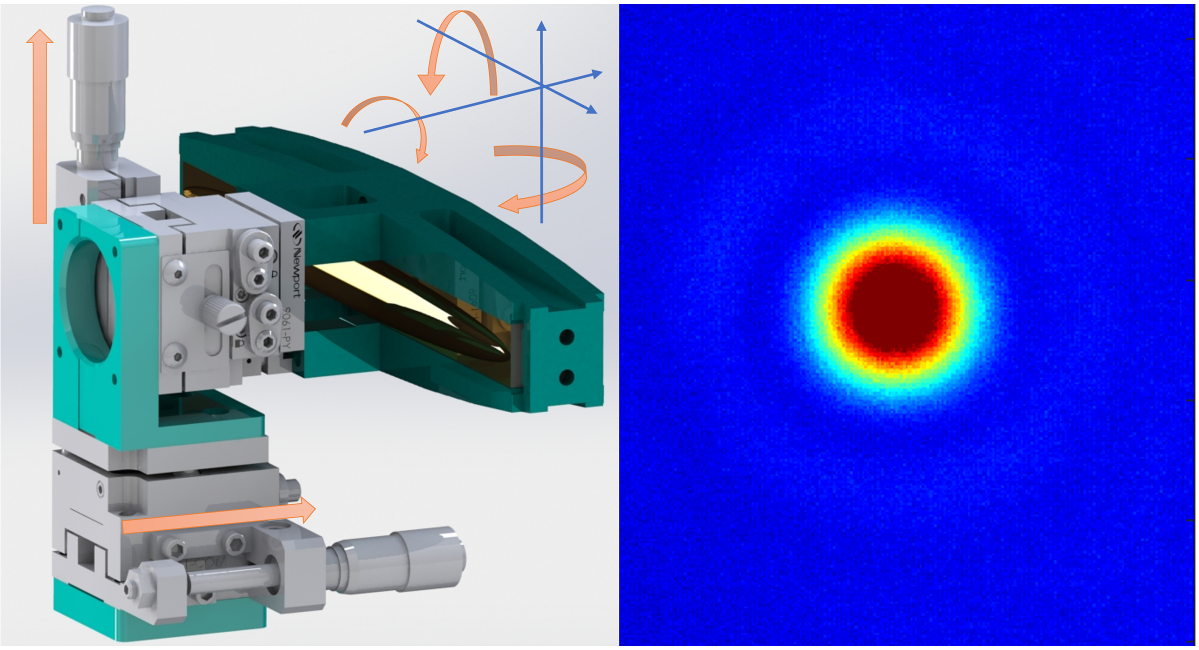

Figure 4.7. Left: The mounting of the toroidal mirror provides 5 degrees of freedom. Which enables the tuning of the refocusing image to be with minimum aberration. Right: the refocus of the fundamental light on the camera.

4.3 Lego Design of Conical Diffraction Grating Geometry - in Reflection Mode

We made High-Performance Spectrometer and Monochromator designs for EUV and X-ray Attosecond Pulses with record-high efficiency and easiness of alignment.

Building a robust spectrometer is essential for high-performance HH light sources. And high-efficiency diffractive optics is highly desired. Toroidal or cylindrical gratings are commonly used but they usually suffer from low efficiency(usually less than 10% towards the 1^{st} order diffraction). Here we pick Echelle-type conical grating in a glaze incidence(2 or 4-degree glaze incidence) way to reduce the shadowing effect and take advantage of its high glazing angle to achieve state-of-art high efficiency(as high as 70% to 90% at specific harmonics(Fig 4.8). The conical grating is designed to be also with six degrees of motion(3 linear and 3 rotational). The

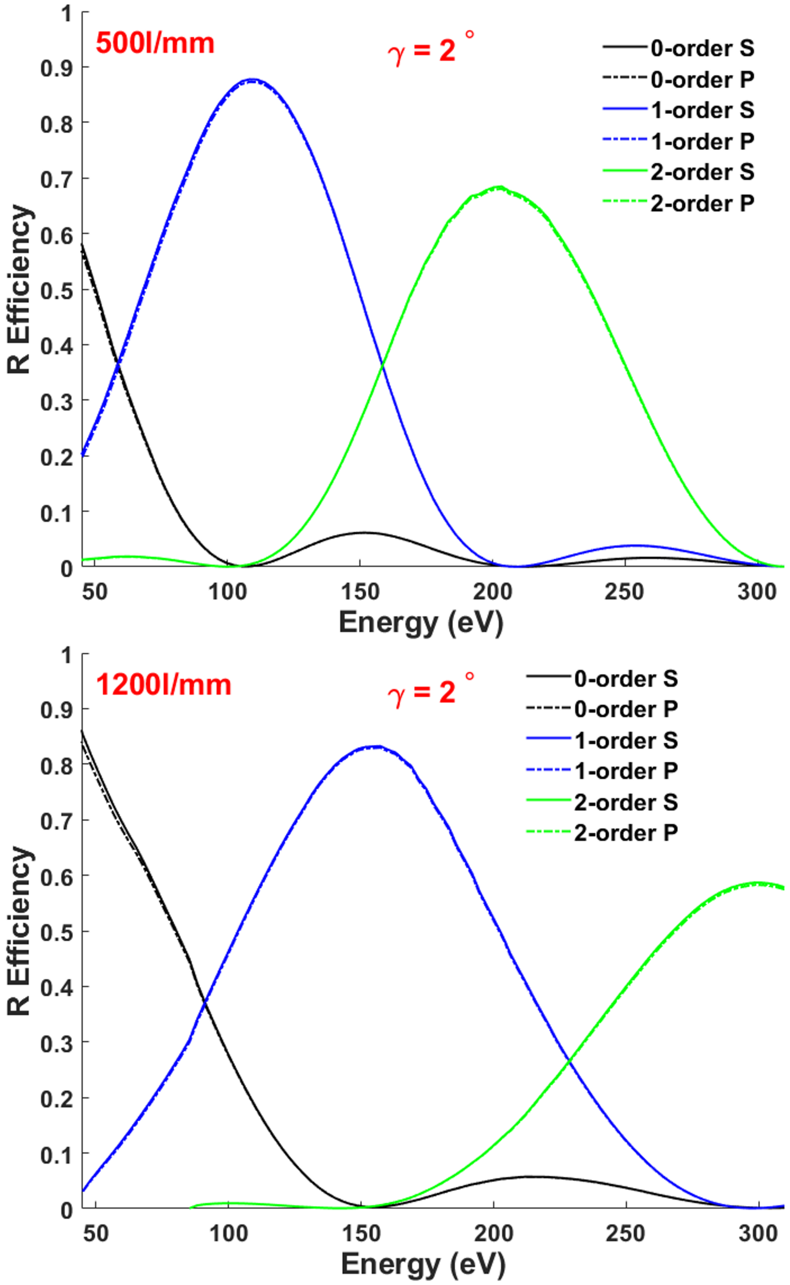

Figure 4.8. Conical grating efficiency for the first and second diffraction order of grating with 500l/mm(Top) and 1200l/mm(Bottom). S and P polarized light have almost identical reflection efficiency. This grating enables record high efficiency in EUV to the softX-ray regime and 60-80% of efficiency can be reached for first, second, and third-order diffraction. More information can be found in Appendix C.

diffraction of given wavelength λ and diffraction order follows the equation:

$$\frac{m\lambda}{d} = \sin\gamma(\sin\alpha + \sin\beta) \tag{4.1}$$

Where d is the groove spacing of the grating. α and β follows the below schematic in Fig 4.9.

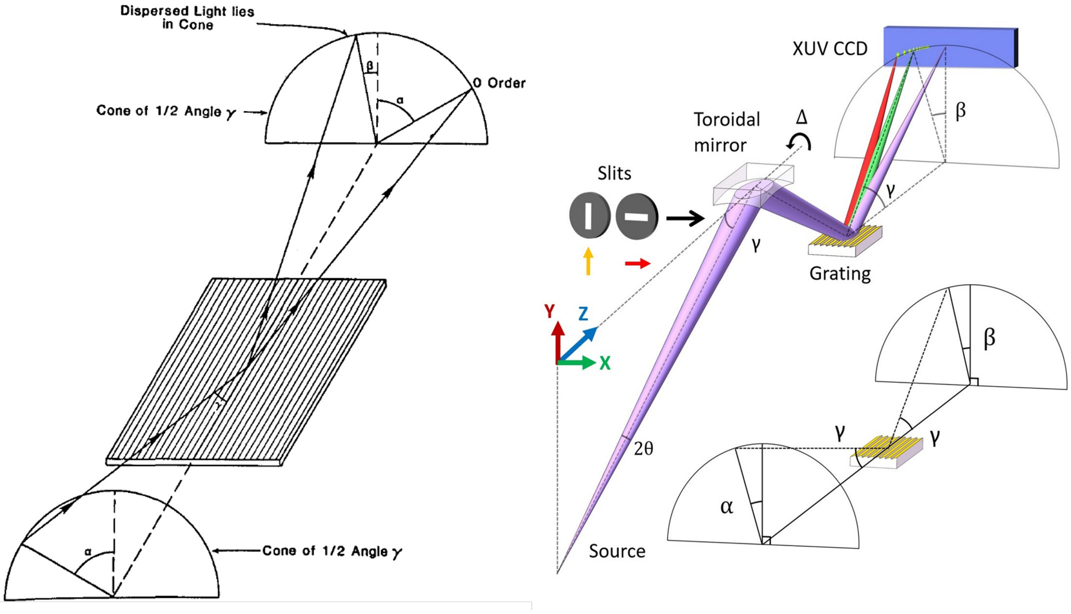

Figure 4.9. Conical diffraction geometry graph from[68, 69]. Spherical coordinates are used here. γ is defined by the angle between the incoming ray and the grating ruling. α and β are the azimuth angle of the incoming and diffracted light.

4.4 Lego Design of Transmission Diffraction Grating Geometry

High Harmonic spectrum usually with many orders of harmonics such that one grating cannot be optimized for the full spectral range for most of the time. We designed here a quick solution by using a nano-structure transmission grating with different groove densities from 500 lines/mm to 10k lines/mm. All of these small transmission gratings are on the same chip(Fig 4.10) such that we can select which one to use just by linear shifting the grating chip.

It is the precise deposition(Fig 4.11) of material and novel electron beam etching that

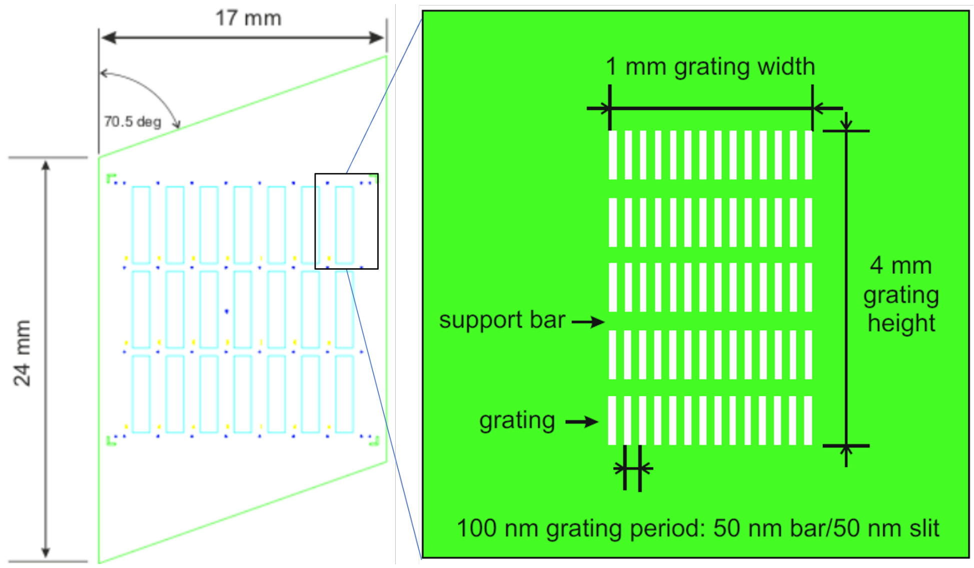

Figure 4.10. Nanostructure transmission gratings on a chip with different groove densities from 500l/mm to 10000l/mm.

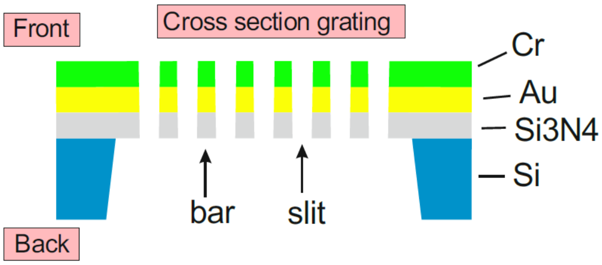

Figure 4.11. Cross section of the transmission grating.

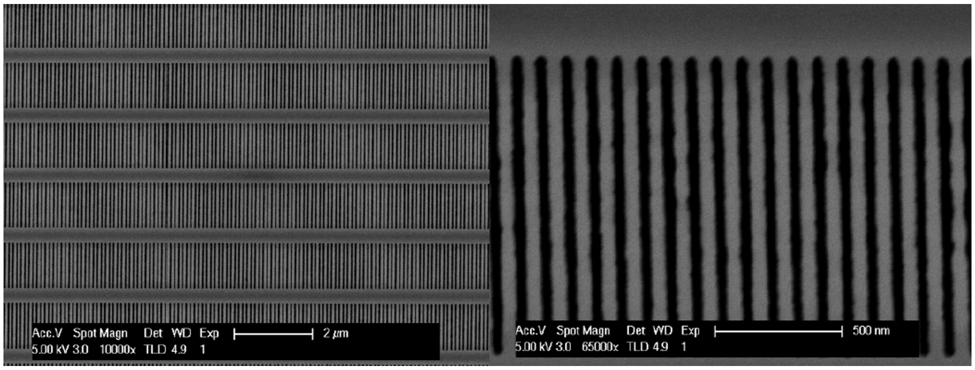

Figure 4.12. SEM image of nanostructure transmission gratings with 10k lines/mm. Adapted from[70].

made this nanostructure grating possible(Fig 4.12). The efficiency is below 20% for the first-order diffraction but it can be used to resolve HH spectrum from the EUV regime all the way to the hard X-ray regime($>$1000eV).

4.5 Modular Beamline Design

The home-designed new version of HH beamlines absorbs many ideas of optimization and tested to be an excellent system for different configurations and experiments. The major advantages of our beamline design include:

1. Highly modular beamline with different modules for a specific task.
2. Compact in volume to boost the vacuum pumping efficiency. The compact design enables efficient pumping with one turbo pump to 10^{-7} torr within one hour.
3. The light height is set to be the lowest at 3 inches to maximize stability.
4. Lego-like half-inch grid system. The length of the beamline is highly adjustable.
5. Light-tight design to reduce the scattered and reflected light to greatly reduce the noise of the CCD camera.
6. Tight-fitting design reduces the complexity of light-waveguide coupling alignment.

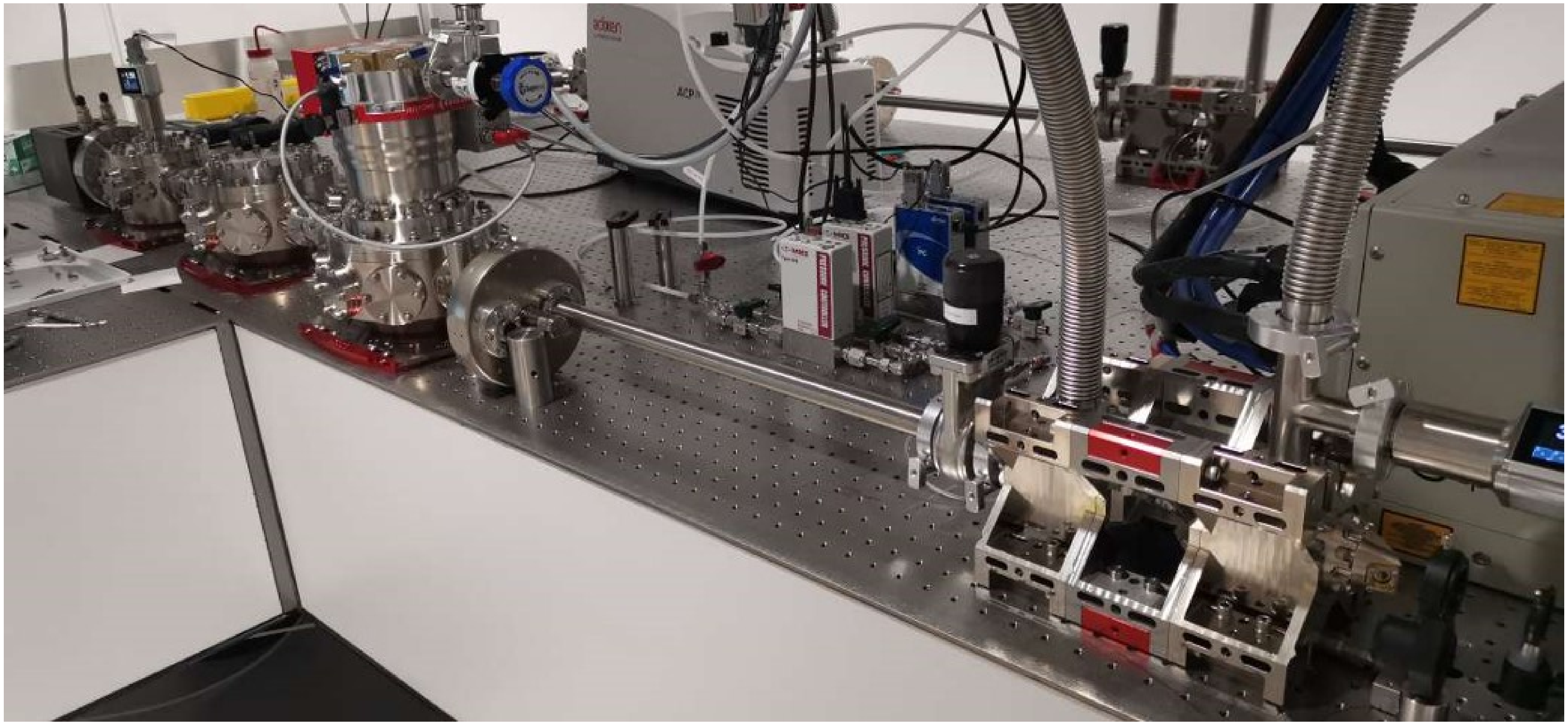

Figure 4.13. Modern compact modular beamline with reflective grating configuration. The full beamline is with a length of less than three meters.

Chapter 5

First Coherent EUV - Soft X-ray Light with Continuous Red and Blue Wavelength Tunability

5.1 Initial Idea

For spectroscopy research. The spectrum of the light source is required to cover the interested spectra range. HH spectrum is able to cover a wide range of spectra with odd harmonics of the driving laser frequency. If the linewidth of each harmonic is narrow then the HH spectrum is similar to a frequency comb and limited for some spectroscopy studies such as probing the absorption edge of many ferromagnetic. To unlock the full potential of HH source as a tool for spectroscopy research, tunability is wanted to be able to shift the harmonic peak to better overlap with the absorption edge. Luckily, there is an efficient way to tune the driving laser central wavelength.

Post-laser Blue shift in atomic gases is found due to plasma-induced SPM or Raman-active ionization[71, 72] or from nonadiabatic effect(a single atom effect) due to the rapid increase in the electric field of an ultrafast laser pulse[73]. And in the other direction, redshift in molecular gases from stimulated/cascaded Raman scattering effect[74]. By tuning the driving laser frequency using atomic or molecular gases, full tunability of HH spectrum can also be achieved.

5.2 Abstract

We demonstrate a continuously wavelength-tunable, bright, narrow-bandwidth, coherent high-order harmonic source in the extreme ultraviolet–soft X-ray spectral range driven by visible lasers. The harmonic peaks are conveniently shifted towards lower or higher energies by adjusting the second harmonic generation phase-matching parameters and gas density inside a spectral-broadening waveguide. In the time domain, the X-rays emerge as a train of sub-300 attosecond pulses, making this source ideal for dynamic, coherent, multidimensional diffractive imaging of ferromagnetic materials, nanostructures, etc., at the nanometer spatial and sub-femtosecond temporal scales. Further, the visible driving laser beams have a record-setting short pulse duration of sub-10fs with a more than 30-fold increase in intensity, stemming from a direct nonlinear assisted self-compression in a second harmonic conversion process of chirped infrared pulses, derived from a spectrally broadened sub-ps Yb: CaF_2 laser amplifier.

5.3 Introduction

State-of-the-art tabletop X-ray sources based on the process of high harmonic generation can deliver fully coherent light with high brightness, unprecedented spatial coherence, and attosecond scale temporal structurec[1, 5, 41, 75, 53, 76, 77]. They have an unsurpassed ability to penetrate opaque objects, visualize subwavelength nanostructures, control spin, and magnetic currents, access the chemistry and structure of materials at a picometer length and femtosecond-to-attosecond temporal scales, etc[53, 26, 78, 79, 80, 81]. Nonetheless, the wavelength tunability of these light sources remains, thus far, very limited. The importance of this feature for tabletop sources has been anticipated to access the dimension of the material's identity through their absorption-edge fingerprints. Most of the current understanding of the atomic or molecular structure of matter and its dynamics is based on diffraction measurements, or more specifically, on the interaction of the light's electric field with the charge density of matter. On the other hand, the magnetic scattering cross-section appears as a small relativistic correction. Even at resonance, the amplitude of the resulting magnetic diffraction can be orders of magnitude smaller than that of the charge scattering amplitude. Accordingly, resonant magnetic diffraction imaging has been one of the most challenging experiments considering that narrow bandwidth, near-edge, ultrabright X-ray light is a prerequisite in this case. Here we demonstrate a fully spatially and temporally coherent, continuously wavelength-tunable, extreme ultra-violet (EUV) – soft X-ray source covering ferromagnetic N and M absorption edges. This source is thus ideal for ultrafast coherent magnetic multidimensional imaging, featuring well-spaced harmonics -, 4.8-5.2 eV - with excellent peak-to-valley contrast, allowing harmonic isolation with EUV mirrors or monochromators and straightforward experimental implementation. Our approach combines continuous tunability of the harmonics towards lower or higher wavelengths in the EUV to the soft X-ray regimes covering the entire photon energy spacing between harmonics for the first time, with high brightness and narrow bandwidth of near 1 eV. The temporal structure is predicted to consist of attosecond pulse trains with a characteristically low attosecond chirp. The VIS source is discussed elsewhere.

5.4 Wavelength-tunable, ultrafast, coherent X-ray light

The high harmonic sources have established the status quo of the tabletop attosecond science owing to the Ti:Sapphire laser amplifiers delivering beams with excellent spatial profile quality and ultrafast pulses down to the near single-cycle regime.

Nevertheless, the spectral range of this laser's wavelength engenders some adverse effects on extending the cutoff energies for high harmonic generation (HHG) and on the ability to phase-match far-infrared (far-IR) frequencies in optical parametric implementations. In our experiments, we used a Yb:CaF_2 laser amplifier at 1030 nm, delivering sub-picosecond laser pulses (180 - 220 fs) with up to 14 mJ at 0.5-1 kHz (Fig. 5.1) [82]. The pulses are spectrally

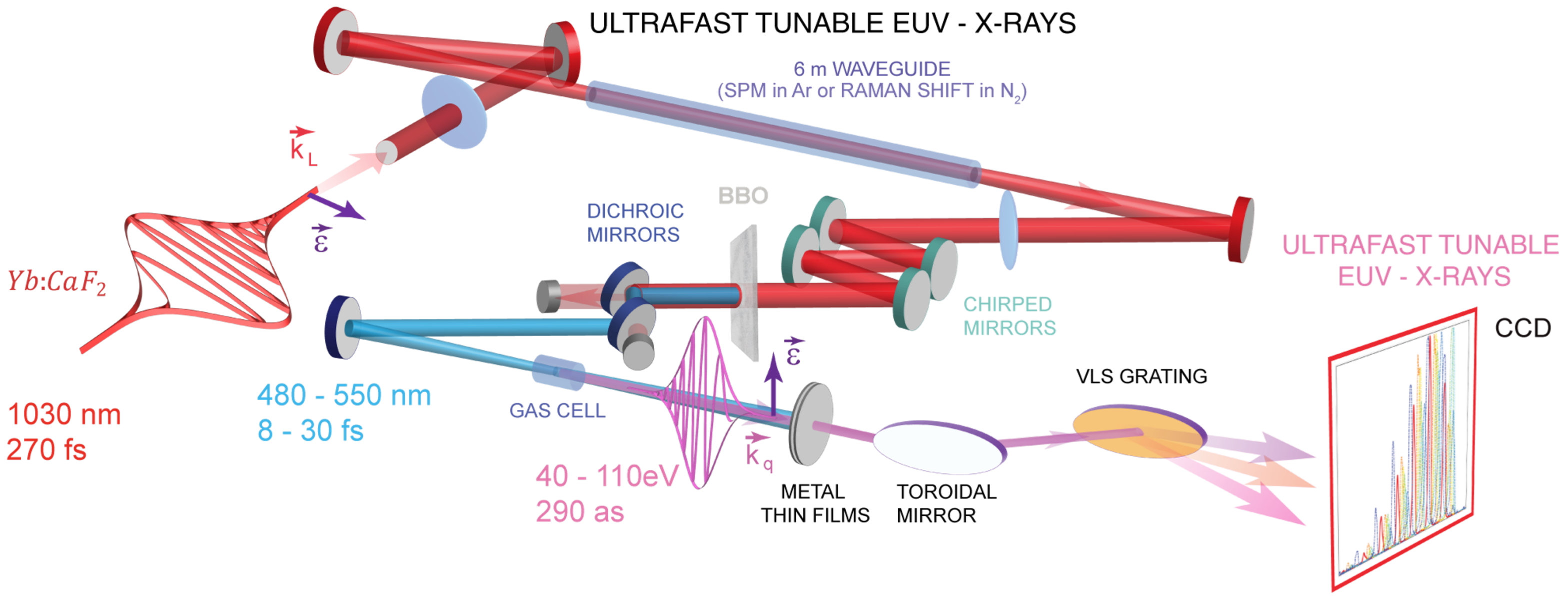

Figure 5.1. Pulse compression and generation of tunable VIS driving laser light at 480-550 nm. Experimental setup: sub-picosecond pulses at 1030 nm are spectrally broadened and compressed to femtosecond scales of 15-30 fs, using a gas-filled hollow-core fiber and chirped mirrors. Further, a 300μm long BBO crystal generates the visible laser beam with a temporal duration of 8-30 fs. The pressure and the nature of the atomic or molecular gas species inside the waveguide control the spectral broadening and the spectral blue or red shift, respectively.

broadened in a 6-meter-long hollow-core fiber with a 1 mm core diameter and compressed using a set of four chirped mirrors, balancing a group delay dispersion (GDD) of near 600 fs^2 [15-22]. Using such an approach, the Yb:CaF_2 laser pulses can be compressed to sub-15fs with partially uncompensated very higher chromatic dispersion orders. Subsequently, we use a BBO type I crystal with 20-30% conversion efficiency to obtain tunable driving pulses in the visible 480-550 nm spectral range, with short record-setting short pulse durations of 8-30 fs in the using crystals. Furthermore, we vary the gas species and tune the pressure inside the waveguide, considering that BBO crystals can phase-match a finite bandwidth to extract a second harmonic with maximum energy and desired spectrum ideal for high harmonic upconversion. The fiber is filled with Ar or N_2 gas at pressures p=30-1000 mbar providing extreme tunability of the blue or red-shifted spectral peak of the second harmonic beams.

Interestingly, intense EUV, UV, and VIS lasers are ideal for harmonic generation since they combine favorable single-atom quantum physics and macroscopic phase-matching physics. Generating high harmonics by short-wavelength lasers exhibits numerous benefits - most notably, extremely high conversion efficiency, ultra-narrow bandwidth harmonics with significant energy separation, extended X-ray cutoffs, inherently compressed attosecond pulse structure, effective phase and group velocity matching, increased phase-mismatch, and excellent spatio-temporal coherence, etc.[53, 83]. Furthermore, recent theoretical studies uncovered that favorable attosecond-femtosecond Rabi oscillations might lead to a boost in the conversion efficiency and prevent depletion of the ionized electronic state for even shorter EUV drivers[84]. The blue and red-shifted broadened spectra can be produced using atomic gasses (i.e., Ar, Kr, Xe, etc.,) and molecular gasses (i.e., N_2, air, etc.), respectively.

Additionally, Fig. 3 demonstrates the possibility of generating high harmonics with maximum energy conversion and continuously tunable energy peaks with both blue- and red-shifts. This is enabled by the favorable interplay between the combination of optimized pressures in the waveguide and phase-matching angles of the single harmonic generating (SHG) crystal to

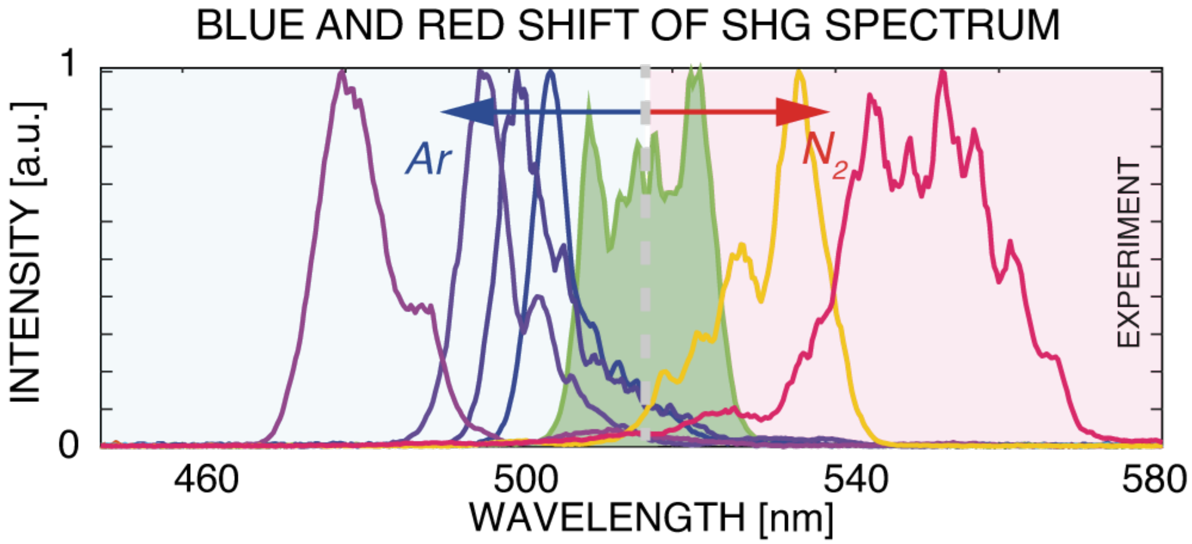

Figure 5.2. Ultrafast, tunable VIS driving laser light. Large range tunable second-harmonic spectra with central wavelengths in the 480 – 580 nm spectral range, optimized for high energy and record short second-harmonic pulse durations, ideal for efficient HHG generation. The pulses are generated in a BBO crystal using gas-broadened spectra in atomic Ar (blue-shaded area) or molecular N_2 (red-shaded area) filled waveguide.

tune the central laser wavelength. We note that, for an ultrabroad 1030 nm spectrum, the HHG peaks have a very limited tunability by simply tuning the BBO phase-matching parameters. In the process of tuning the gas pressure and, consequently, the carrier frequency of the SHG pulses, the constant chromatic dispersion of the chirped mirrors appears to limit, at first, the pulse compression of the IR pulses as the chromatic dispersion is varied. However, shorter visible pulses are beneficially obtained in the second harmonic generation process. The group velocity walk-off between the fundamental and second harmonic pulses, combined with the BBO chromatic dispersion, limits the energy transfer between the pulses and leads to temporal reshaping and spread of the pulses. Nonetheless, the situation changes when the pulse tail contains substantial energy. Using chirped pulses, the rear of the fundamental pulse transfers power to the second harmonic peak at farther propagation distances, owing to group-velocity mismatch[60]. This results in a sharp peak with shortened second harmonic pulse duration. Hence, the third (TOD) and higher dispersion orders act as a driving source for self-compression. In addition, the pulse chirping prevents further distortion of the pulse spread during propagation

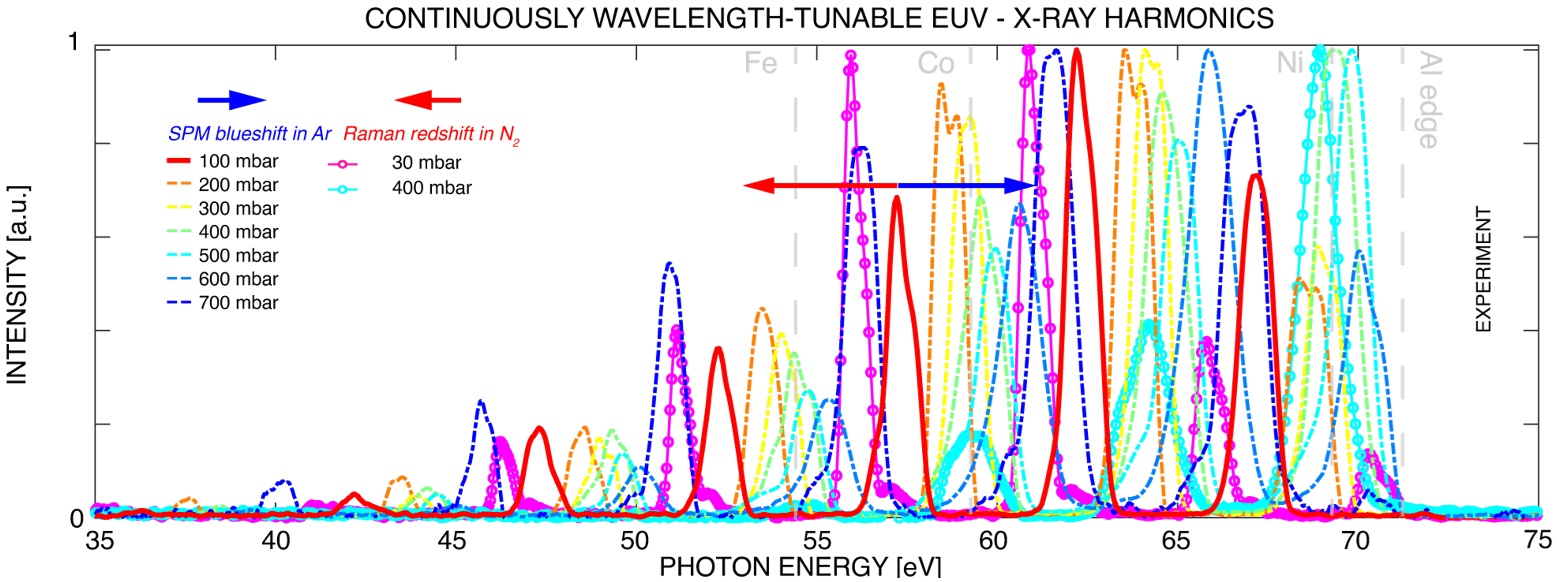

Figure 5.3. Continuously wavelength-tunable EUV – X-ray high harmonics from He atoms, generated by a tunable VIS driving laser with wavelengths spanning the broad range of 480 - 550nm. Blue-shift and red-shift wavelength-tunable EUV harmonics. The arrows indicate the shift direction when atomic Ar (blue-shift) or molecular N_2 gas (red-shift) is used for spectral broadening (the color coding denotes the corresponding pressure).

in the dispersive media due to lower nonlinearity for longer pulse durations. Alternatively, a transform-limited fundamental pulse will require an extremely short crystal length to maintain a short pulse duration at the second harmonic, causing a significantly lower conversion efficiency.

In our experiments, the high harmonics are generated by tunable VIS pulses in the 480-550 nm spectral range in a He-filled gas cell which is the unsurpassed medium for high cutoff upconversion due to the high transparency of the gas and high ionization potential[42]. The high harmonic beams are then imaged by a gold-coated toroidal mirror, spectrally separated by a gold-coated blazed spherical grating with variable line spacing. Then, the spectrally dispersed beams are detected by an X-ray CCD camera (Fig. 5.1). The blue- and the red-shifts of the VIS beam spectrum, realized inside of Ar or N_2-filled waveguide, allows for a high harmonic shift by two photons or one odd harmonic in the EUV and soft-X-ray region. This exhibits a full tunability between two adjacent harmonics towards lower or higher energies while preserving the high harmonic brightness, which has not been demonstrated to date.

However, in experiments, full tunability is rarely required as the red or blue shift of two adjacent harmonics can be adjusted to match a magnetic resonant absorption edge in the spectral space in-between, utilizing atomic or Raman-induced spectral shift in N_2 (Fig. 5.2) or other molecular gasses, i.e., air. Furthermore, the harmonics are well separated by 4.8-5.2 eV allowing for an easier selection of a resonant harmonic with X-ray mirrors or transmission filters. Finally, the harmonics are generated with an excellent peak-to-valley contrast allowing direct experimental implementation in schemes where narrow-band light is essential, e.g., in coherent diffractive magnetic imaging where off-resonance light can produce a large charge-scattering background.

The phase-matching conditions for bright coherent upconversion using visible driving wavelengths in the 480 – 550 nm spectral range allow, first, for a broader temporal phase matching window and, second, second for effectively phase-matched upconversion throughout the EUV spectral range and the soft X-ray regime up to a phase matching cutoff of 130 eV. The critical ionization level which sets a limit to the maximum laser intensity which can used,

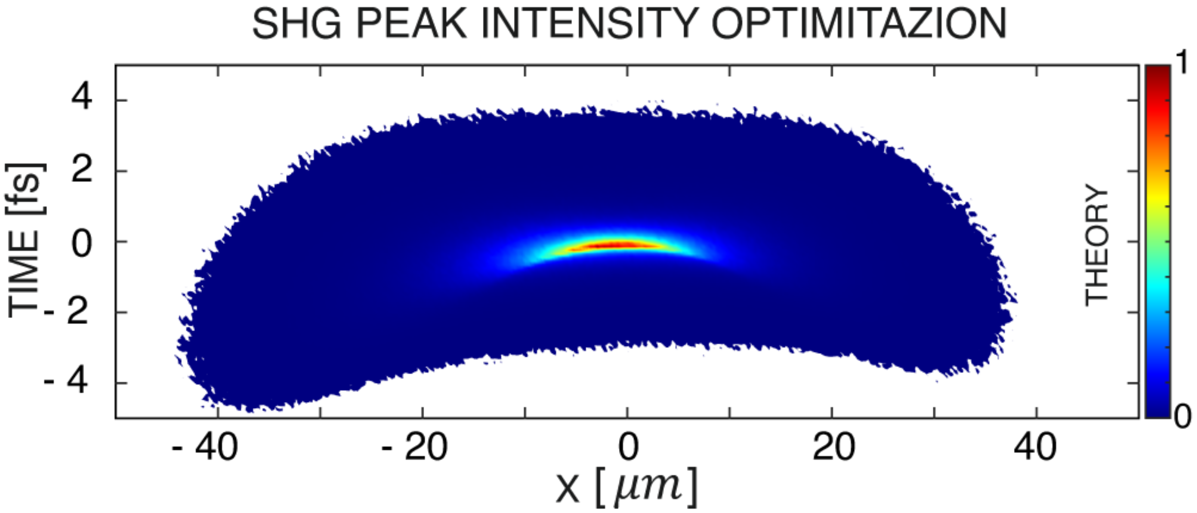

Figure 5.4. Second harmonic peak intensity optimization of the VIS driving laser light. Neural network optimization of flat wavefront second harmonic beam showing an optimal spatio-temporal intensity distribution at the focus.

is favorably boosted due to the larger indices of refraction of noble gases for shorter VIS-UV drivers as we approach the UV resonances of atoms. Furthermore, the indices of refraction of ions also become significant. As a result, bright narrow linewidth harmonics are generated due to the larger number of the half cycles which contribute to the constructive addition of high harmonic fields. Furthermore, higher effective phase matching cutoffs are allowed due to the increase of the limiting laser intensity. The broad bidirectional wavelength tunability of the driver leads to a smooth change of the phase matching conditions without substantial changes of phase matching parameters as shown in Fig. 5.5. Neutral He atoms and He+ ion modify the phase matching conditions to boost the emission per atom to scaling of $\lambda_{LASER}^{-7.5}$ with driving laser wavelength.

In addition, to maximize the VIS laser intensity and, correspondingly, to extend the X-ray cutoff in this geometry, we use a very short 15 cm focusing spherical mirror at a 3° incidence angle. These parameters are selected by a Neural-Network optimization using Monte-Carlo ray tracing for the highest peak-intensity-product $1/\omega_x\omega_y\tau$ at the focus in restricted parameter space, where ω_x, ω_y, τ are the beam waists in x and y direction and the temporally broadened pulse duration due to the focusing geometry (Fig.5.4), respectively[85]. In addition, we vary the location where the peak-intensity product is estimated and effectively define the focus at the position of the circle of least confusion. The simulated SHG source spatial size has statistical Gaussian distribution with a standard deviation of $\sigma_{x,y} = 2.8$ mm and statistical divergence with a standard deviation of $\sigma_{\theta_x,\theta_y} = 100$ μrad, corresponding to an M-squared value of $M^{2\sim3-5}$. The statistical approach provides an efficient way to evaluate the beam parameters, both spatial and temporal, at the desired position with a relatively small number of rays.

Our calculations indicate that for the selected beam waist and divergence, spherical mirrors down to nearly 10 cm of focal length can be used to achieve tight focusing before the spatiotemporal aberrations limit the intensity growth. In this configuration, we experimentally observe harmonics up to $>$ 110 eV emitted from neutral He atoms (Fig.5.6). No emission from He ions is observed, as indicated by the strong-field approximation (SFA) calculations in Fig. 5.6 (C). In the future, increasing the peak intensity of the driving VIS laser beams will readily effectively phase-match harmonics in the “water window” at 285 - 420 eV, where water is transparent, hence allowing for in vivo dynamic studies of artificial or living specimens, and beyond.

5.5 Conclusion

In summary, we demonstrated continuous wavelength-tunable bright harmonics, resonantly covering the magnetic N and M absorption edges of ferromagnetic elements: Fe 54 eV, Co 60 eV, Ni 68 eV, Gd 20 eV, and 145 eV. The harmonics emerge as a train of sub-300 attosecond pulses in the time domain, as indicated by our calculations, allowing for ultrafast pump-probe multidimensional (4+1D) imaging in the near future, where the additional effective dimension is the material identity. Moreover, we generate continuously wavelength-tunable, visible beams with ultrashort pulse duration down to 8 fs, owing to direct nonlinear self-compression.

Chapter 5, in full, is currently being prepared for the publication of the material:

Wavelength-Tuneable High-order Harmonics: A Novel Approach for Narrow Bandwidth, Coherent and Bright EUV - Soft X-ray Radiation with Controlled Spectrum. Dimitar Popmintchev, Siyang Wang, Jieyu Yan, Sirius Song, Ryan Clairmont, Zhihan Wu, Elizaveta Gangrskaia, Tenio Popmintchev.The dissertation author is the co-author of this paper.

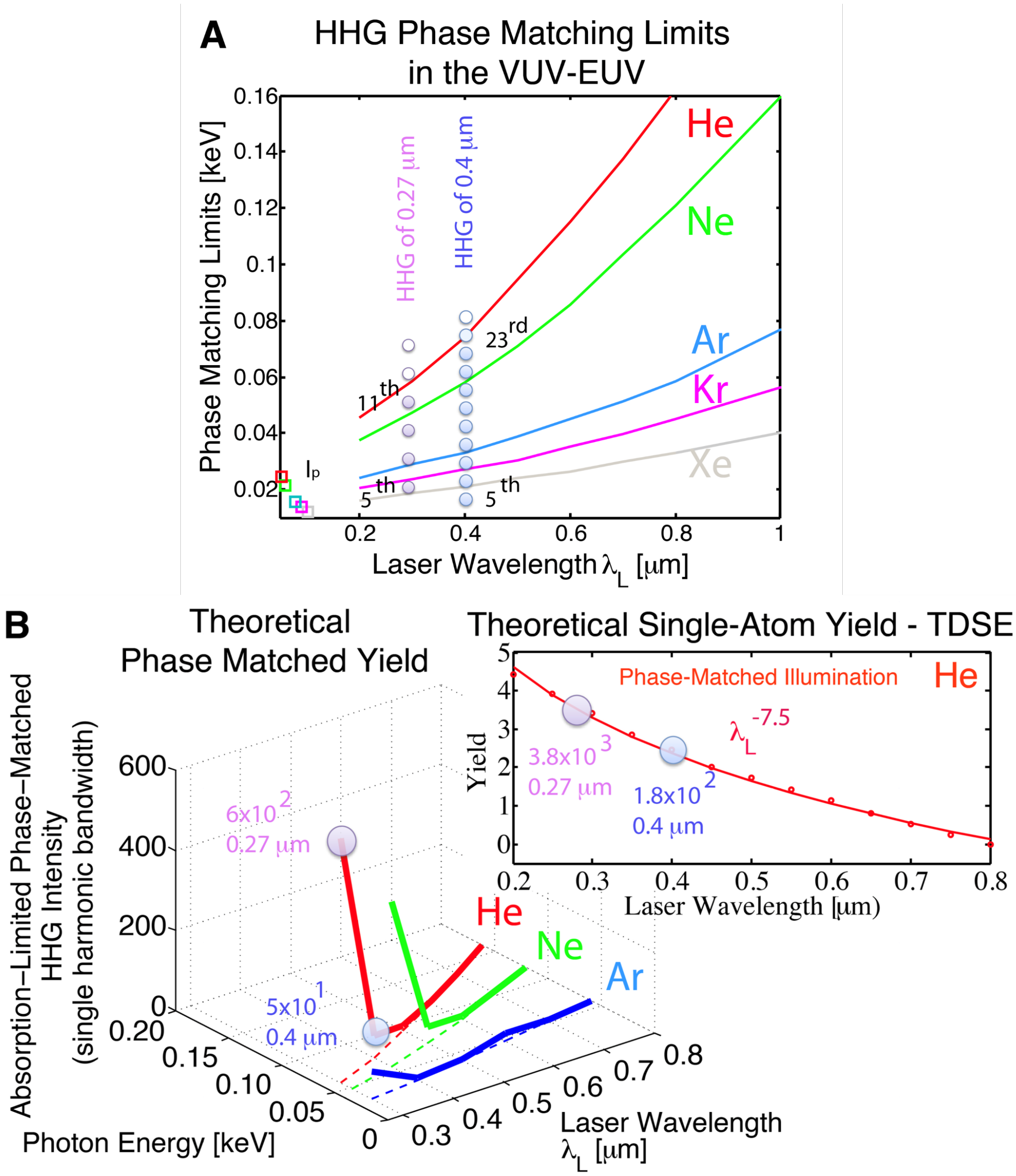

Figure 5.5. Predicted high harmonic full phase matching and effective phase matching emission as a function of the driving laser wavelength in the VIS and UV regions. A) Phase matching and effective phase matching cutoffs. Lines show the theoretical predictions. Solid circles represent experimental results using 0.27 and 0.4 μm laser pulses. Open circles show non-phase-matched HHG orders. B. Using UV driving lasers, a combination of very high critical ionization for phase matching, high laser intensity, high single-atom microscopic yield that scales very favorably as $\lambda_{LASER}^{-7.5}$ under phase-matched illumination, and high phase-matched macroscopic yield allow for more than two orders of magnitude higher VUV-EUV harmonic flux compared with 0.8 μm drivers. The plots are normalized to the phase-matched emission for each gas using 0.8 μm Ti:Sapphire driving lasers.

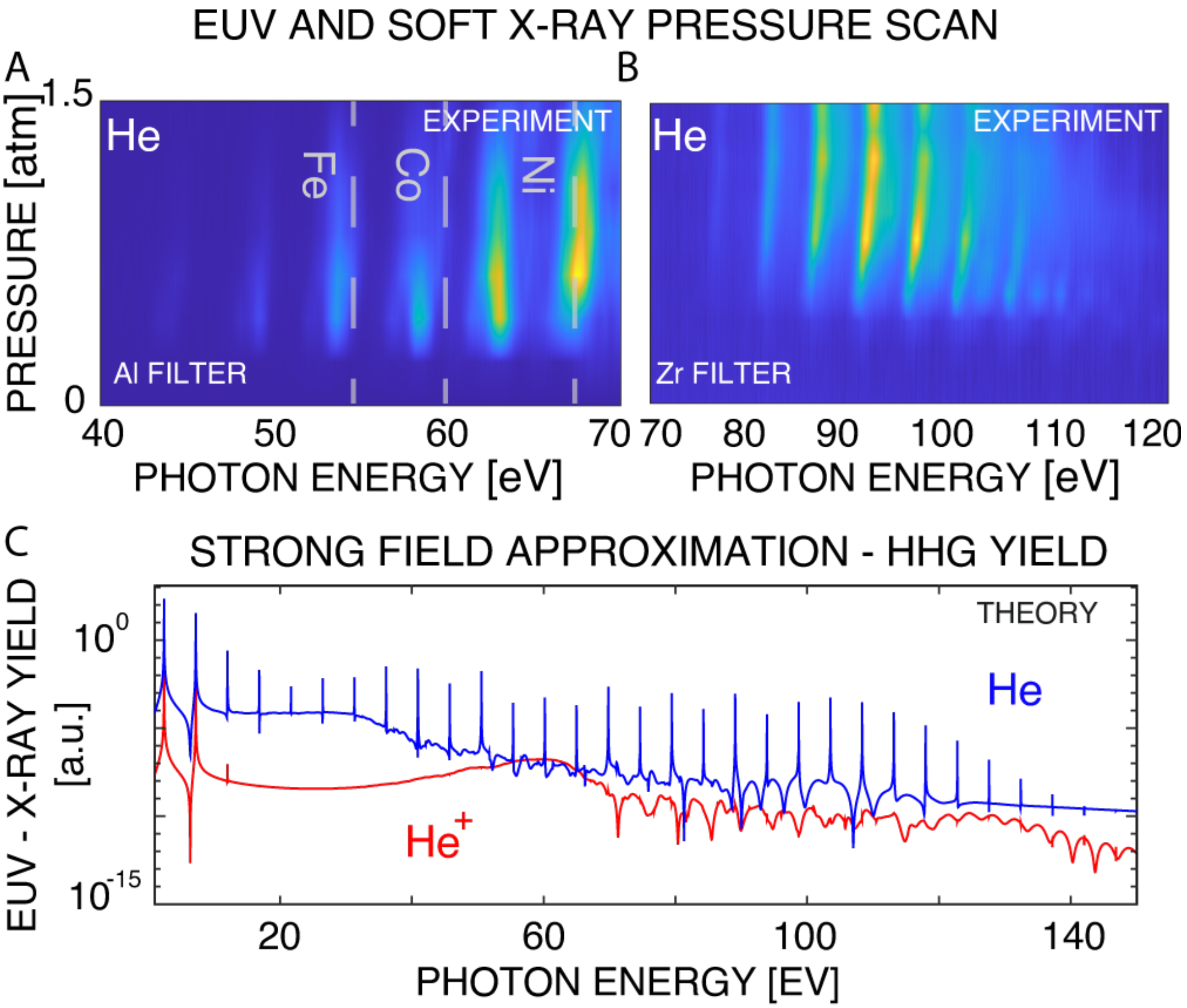

Figure 5.6. Continuously wavelength-tunable EUV – X-ray high harmonics from He atoms, generated by a tunable VIS driving laser with wavelengths spanning the broad range of 480-550 nm. A) and B) Experimental backing-pressure dependence of the high harmonics from He, extending into the soft-X-ray region for Ar-filled waveguide at 400 mbar. C) Single-atom estimate of the harmonic yield from neutral He atoms and He+ ions at an intensity of 10^{15}/ W/cm^2.

Chapter 6

Extending Bright Coherent EUV High Harmonic Emission into the X-ray Regime Using 400 nm Driving Laser

We demonstrate here the fundamental research of exploring the properties and limits of High Harmonic Generation by using a 400 nm driving laser. The 400 nm driven HH shows many features that enable it to be a very robust and ultrabright light source that covers the EUV regime and can be extended to the soft X-ray regime.

6.1 Experimental Setup

The driving laser is the second harmonic from a Ti: Sapphire laser amplifier with a central wavelength of 800 nm, up to 7W at 1 kHz repetition rate and 35fs pulse duration. The second harmonic as the driving laser of HH is generated by using a type 1 BBO crystal. Its power can go up to 2.2W with 28 fs pulse duration measured by Self-diffraction(SD) FROG 6.2. The HH is generated inside a gas-filled hollow-core capillary with an inner diameter of 150 or 250 μm. By using grating with different groove densities we could see wanted harmonics with good resolutions and the harmonics show a narrow linewidth feature as in Fig.6.3. We are able to see the HH cutoff of both Helium and Argon to be around 150eV at different phase-matching gas pressure.

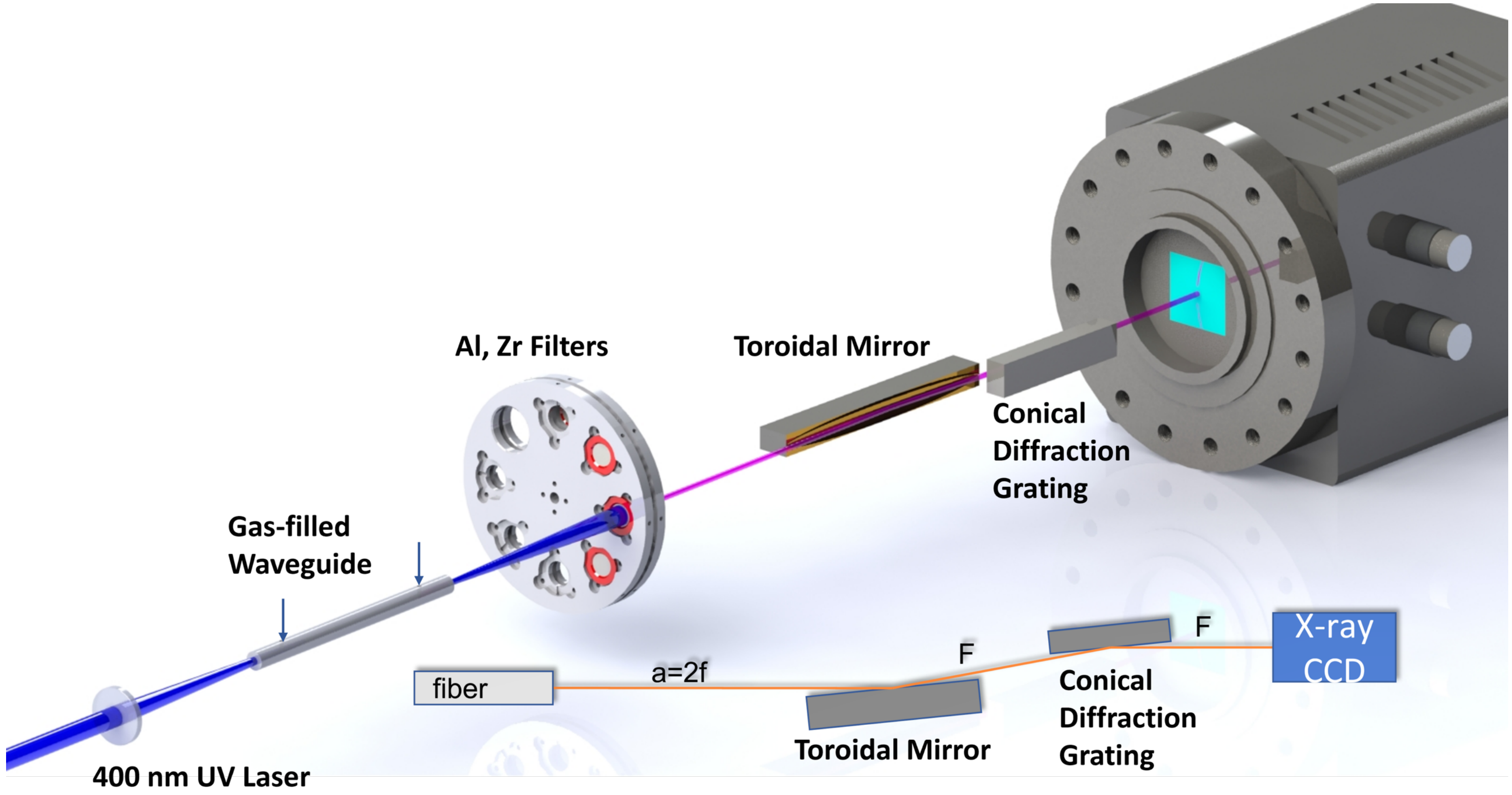

Figure 6.1. High Harmonic Beamline Setup The 400nm laser gets focused on the noble gas-filled Waveguide and then get filtered by two thin Metal filter on Filter Wheel. Harmonics through filters incident on a toroidal mirror at 2 degrees to do 2f-2f imaging to the CCD camera. A conical diffraction-type grating is at halfway from the toroidal mirror to the camera and diffracts the harmonics in a conical pattern.

This novel 2-optics spectrometer design(Fig 6.1) is able to achieve overall high efficiency, low cost, and simplicity. The overall efficiency from the 2 optics can reach close to 80% for certain harmonic which enables detecting the weakest signal. The most commonly used conical diffraction grating in our experiment is with 500 lines/mm and 1200 lines/mm and with nearly 2 degrees of glaze incidence angle in our experiment, the efficiency simulation can be found in Fig 4.8. More calculations can be found in Appendix C.

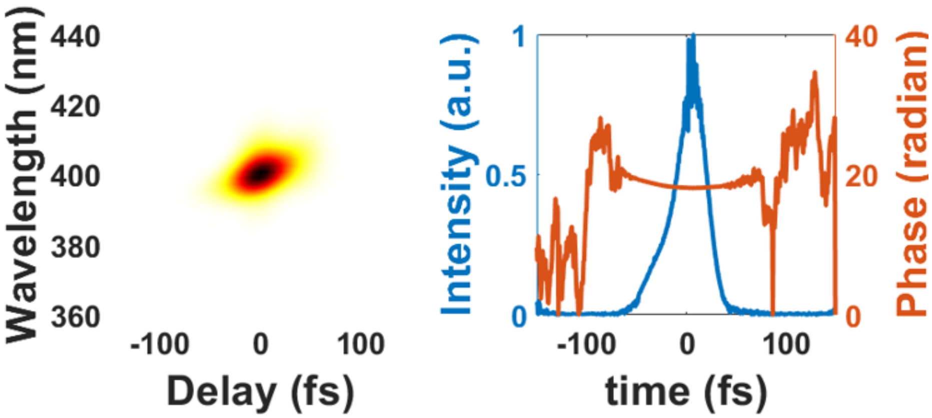

Figure 6.2. Self-diffraction frequency-resolved optical gating(SD-FROG) measurement of the 400 nm driving laser. The pulse duration can be down to 28 fs.

Without quasi-phase matching, the 400 nm driven high harmonic is able to reach a bright phase-matched cutoff in the soft X-ray regime. The bright phase-matched cutoff from He and Ar is observed to be up to more than 140 eV(Fig 6.3) and from Ne to be up to 120 eV. This is by far the record high achieved experimental high harmonic cutoff by using the second harmonic of Ti:Sapphire laser.

Ultrabright HH signal at the EUV regime is observed with optimized waveguide coupling and phase-matching conditions.

6.2 Ultrabright harmonic signal in EUV Regime

The HH single atom yield scale with $\lambda_L^{-5.5}$[38, 39, 40]. The 400nm driving HH is ultrabright that is promising for applications such as imaging. The number of photons per eV

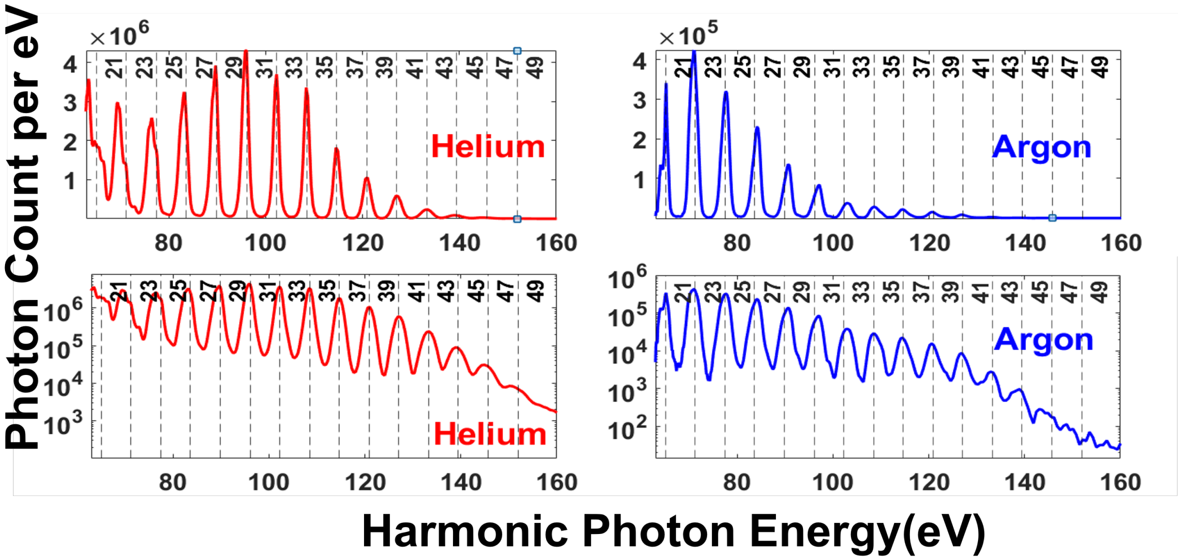

Figure 6.3. High Harmonic Spectrum from argon and helium Top: HH spectrum from helium and argon with a linear scale.Bottom: HH spectrum from helium and argon with a log scale. The conventional cutoff is more t than 140 eV. The HH is optimized at 31st harmonics with 13 nm in Helium.

per second with optimized parameters can reach 10^{10} photons per eV per second for harmonics below the Al edge(at around 72eV) and can reach 10^6 photons per eV per second for harmonics above Zr edge(at around 65eV) all the way to 31^{th} harmonic corresponding to 96.1eV photon energy which is close to the industrial-interested light at 13.5nm. The counting of high harmonic photons is achieved by using the signal from the X-ray CCD. With determined q-th harmonic energy E_q at a certain CCD pixel, then the photon number N_q can be calculated by the pixel count N_{pixel} with the equation:

$$N_q = \frac{N_{pixel}}{(E_q/E_{eh})\eta_q g} \tag{6.1}$$

Where E_{eh} is the electron-hole pair in silicon which is 3.65eV. η_q is the quantum efficiency of the CCD camera at photon energy E_q and g is the analog gain which determines how many electrons can fill the well to contribute a single count. The incident angle-dependent efficiency of the grating and toroidal mirror can be calculated with specific photon energy such that we are able to calculate the theoretical photon flux at the source.

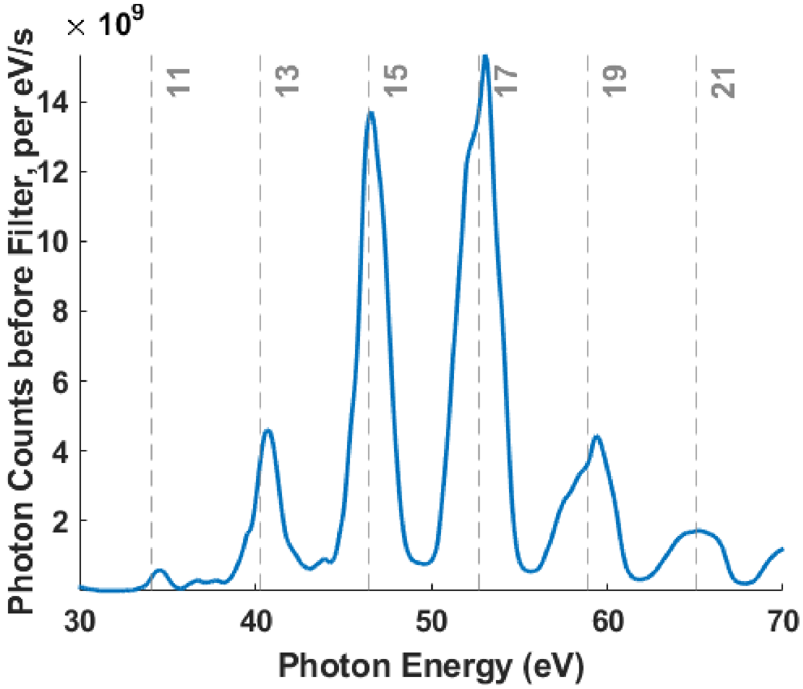

Figure 6.4. Calculated photon flux at the source. The harmonic photon per harmonic is able to reach 10^{10} photons/eV/s for 15^{th} and 17^{th} harmonic with corresponding photon energy of 46.5eV and 52.7eV.

6.3 Phase Matching Bahavior

UV-driven HH can take advantage of the scaling of plasma and ion dispersion to be able to balance each other such that the high ionization level won't destroy the phase-matching completely and in the way, the temporal phase-matching window is longer such that it is a much more phase-matching friendly regime compared to IR-driven HH. Many cycles of UV driving laser can be within this phase-matching window such that the coherent addition of HH is very efficient and much easier especially within a waveguide geometry where the spatial region for coherent addition of HH signal can move along the waveguide. In such a way, the phase-matching condition for 400nm driving HH can be met with a large range of noble gas pressure as shown in Fig 6.5 and Fig 6.7 for a smaller range with the different signal regime with argon and helium. The higher gas pressure comes with weaker signal strength. However, that decrease could be explained by the long propagation length inside the waveguide and reabsorption from the gas.

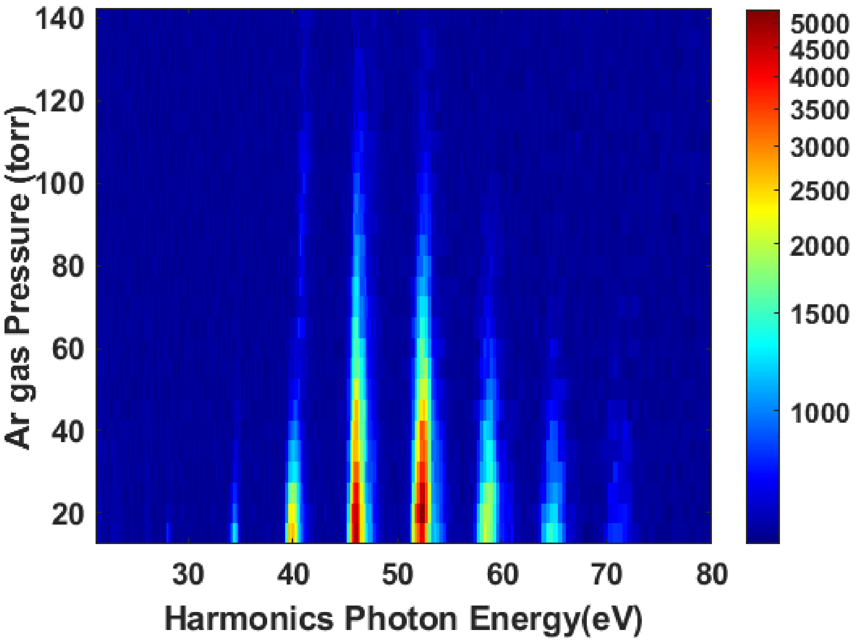

Figure 6.5. HH gas pressure scan with Ar and Al filters. The pressure scan shows that phase-matching favors low gas pressure.

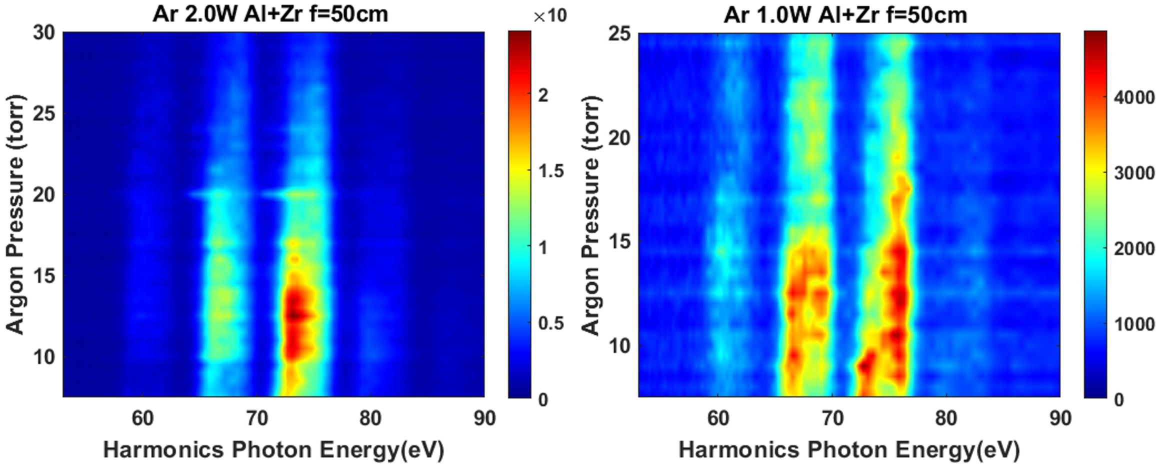

Figure 6.6. HH gas pressure scan with Ar. High-resolution pressure scan with 1W and 2W of driving laser power. Using a combination of aluminum and zirconium filters. This shows a weak expected tendency that higher-order harmonic favors high pressure.

6.4 Reaching Ultra-High Peak Intensity

Here we use a focusing lens that simplifies the experimental setup and also makes longitudinal tuning of focus position possible. For femtosecond driving laser pulse with a

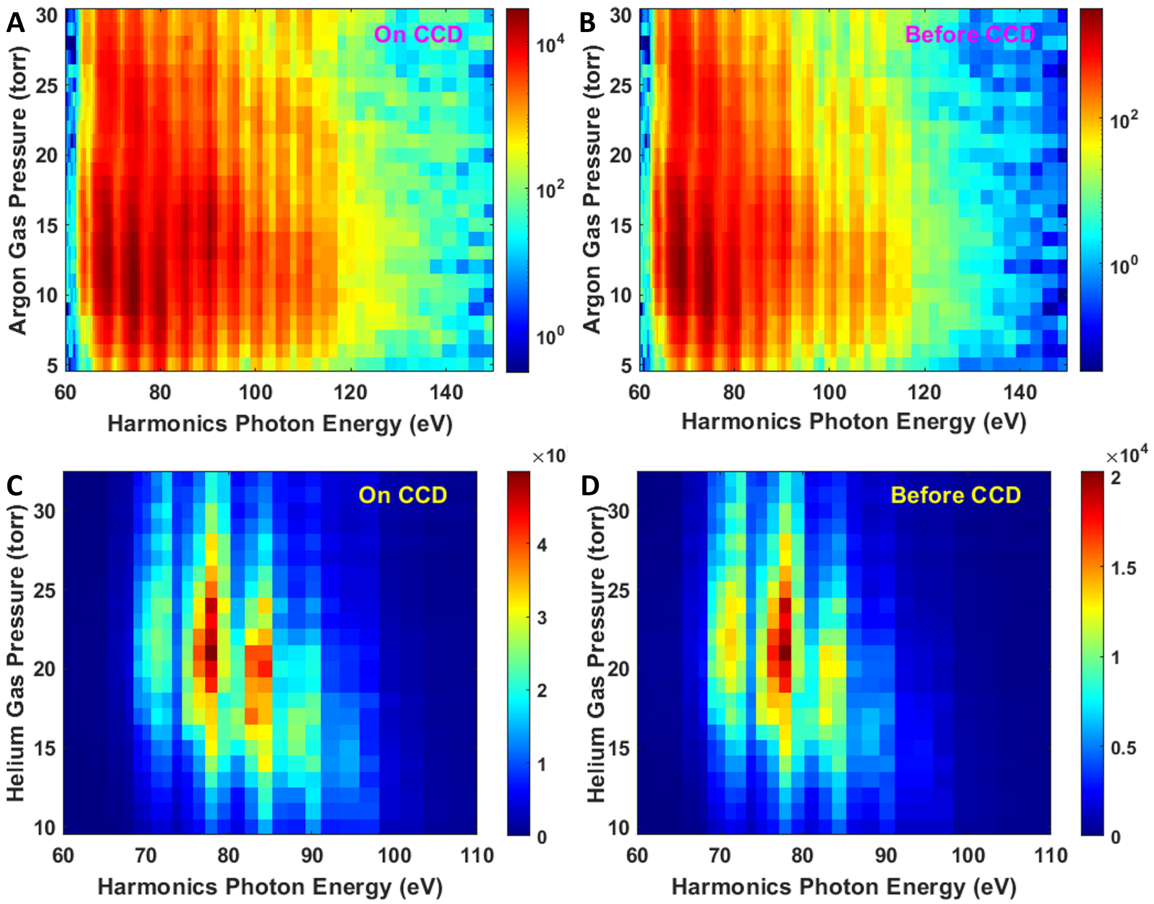

Figure 6.7. HH gas pressure scan with Ar(A and B) and He(C and D). Pressure scan with 2W of driving laser power with high peak intensity. Using a pair of zirconium filters. (A and C): Measured intensity of HH signal on the CCD at different gas pressure. (B and D): calculated photo count per eV before the CCD at different gas pressure with CCD hole-pair excitation and quantum efficiency into account.

relatively broad bandwidth, the lens will induce chromatic aberration with different optical path $d_{opt} = n_L(\lambda)L(h)$ within the lens, where $n_L(\lambda)$ is the wavelength-dependent refractive index and $L(h)$ is the lens thickness at different height transverse h. Wavelength-dependent defocusing $f(\lambda)$. This chromatic aberration will elongate the focus over a length $\Delta f(\lambda) = -f^2\Delta\frac{\partial(1/f)}{\partial\lambda}$. Also, the different thicknesses of the lens will introduce different nonlinear dispersion at different heights which could lead to big pulse front tilt and pulse broadening with $\Delta\tau = t(h) - t(0) = \frac{-\lambda h^2}{2(n-1)f(\lambda)}\frac{\partial n}{\partial\lambda}$.where $t(h)$ is the time delay for the light within the beam but with transverse height h from the optical axis. For our UV driving laser, the nonlinear dispersion is a major obstacle to achieving good focus with ultrahigh peak intensity.

Instead of a lens, the focusing mirrors do not suffer from chromatic aberration. But it suffers geometrical aberration that depends on the ratio of transverse height h and the radius of the mirror R. It also broadens the pulse at focus with $\Delta\tau = t(h) - t(0) = -\frac{3}{4c}\frac{h^4}{R^3}$. Also, the focusing mirror usually has to deviate the reflected beam from the incoming beam by angle θ which induced a different focusing condition for rays in the plane of incidence, and the rays in the plane perpendicular to the plane of incidence. For a large beam, it is hard to keep the deviation angle θ to be very small(within at least 5 degrees). These issues prevent us from reaching high peak intensity by using tight focusing for efficient HHG with the highest cutoff. This angle issue can be solved with a customized coating that is optimized for a fixed degree of incidence.

The driving laser scan shows that for the higher orders of harmonic that need to be observed with Zr filters, the cutoff has a healthy linear relationship with the increasing laser power until the peak intensity is not enough to ionize the electron with high ionization potential(helium case). The low-order harmonics show a positive correlation with the driving laser power which shows that the limit of the brightness of 400nm driving HH is not yet reached by using the current laser system. The 400nm driven HH with ultrabright signal and with a large range of phase-matching pressure could potentially be with an even higher cutoff energy but it is limited by the highest peak intensity the laser can be reached. It is very promising to reach the 'water window' regime with higher driving laser peak intensity.

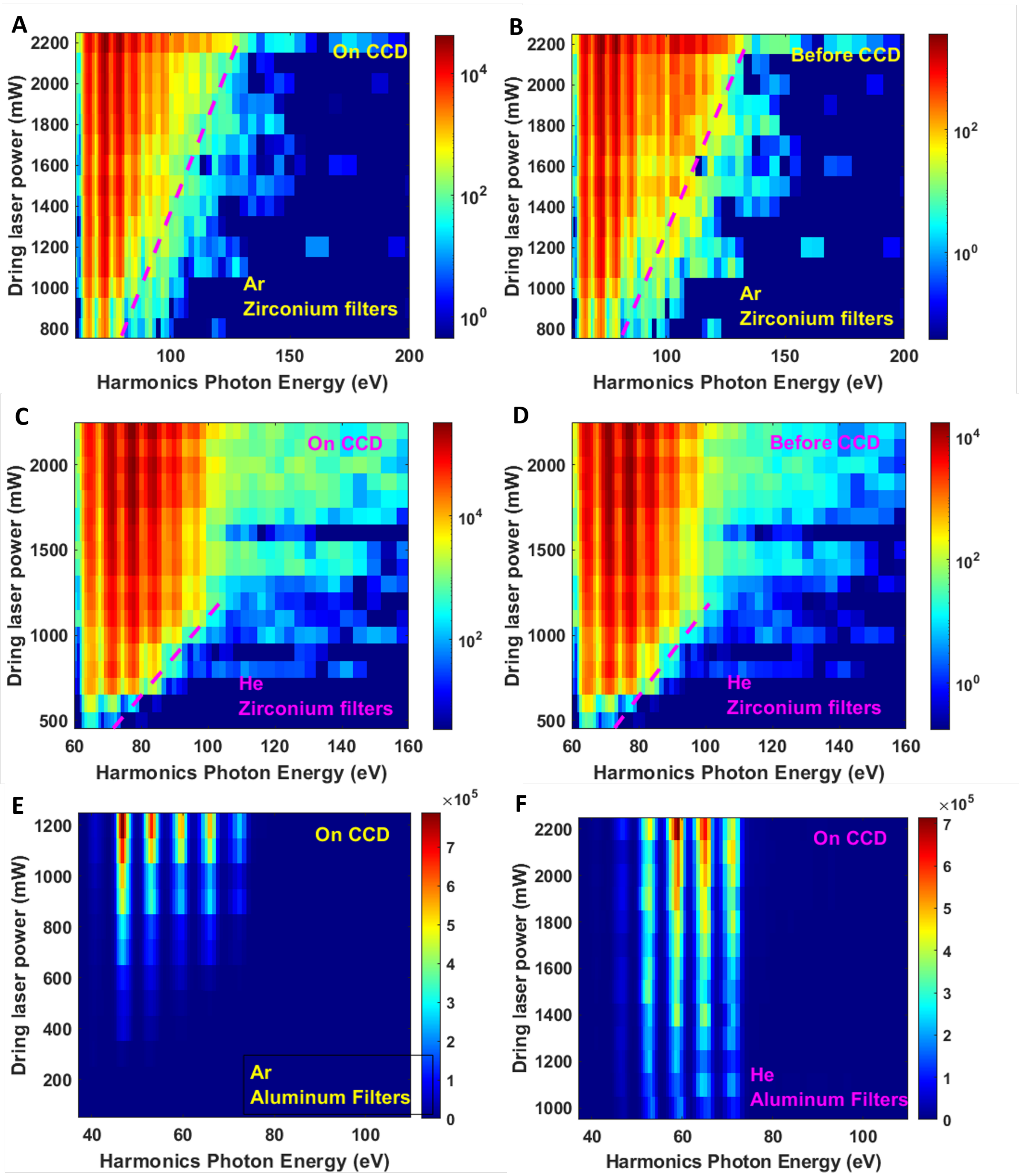

Figure 6.8. Driving laser power scan. (A and C): Measured intensity of HH signal on the CCD at different laser power with Ar and He with Zr filters. (B and D): calculated photo count per eV before the CCD at different laser power with Ar and He with Zr filters. (E and F): Measured intensity of HH signal on the CCD at different laser power with Ar and He with Al filters

Chapter 7

Surprise in Electron-Electron Correlations - Ionization and Recombination Effects

We demonstrate here the extension of the High-Harmonic-Generation cutoff photon energy in the soft X-ray regime up to 300eV which is likely from the double recombination of correlated electrons of Helium.

7.1 Discovery of Secondary High Harmonic Plateau

We observe experimentally, for the first time to our knowledge, a secondary plateau in UV-driven high harmonic generation in the X-ray regime, extending the conventional cutoff from 130 eV to 300 eV, due to emission of a single X-ray photon at double recombination of highly-correlated electrons in helium atoms. We use 400 nm UV laser pulses, with a duration of 28 fs and energies of up to 2.8 mJ at 1 kHz, derived through a second harmonic upconversion of a Ti:Sapphire laser amplifier, which is used to drive high harmonic generation inside a gas-filled hollow waveguide (Figure 6.1). Bright emission extending up to 120-150 eV from He, Ne, and Ar is observed within the effective phase-matching cutoffs for UV driving lasers, where low quantum diffusion of the rescattering electron and high linear refractive indices of atoms and ions contribute favorably to increase the single atom and ion yield, and the phase-matching efficiency[53]. With increasing the peak intensity by using tighter focus, the HH spectrum shifts towards a higher cutoff and enters an over-driving regime that the fast accumulation of laser-induced plasma starts to diminish the optimal phase-matching conditions but boosts the possible correlation of electrons. Surprisingly, at laser intensities greater than 2×10^{15}W/cm2, X-ray emission from He exhibits two signature plateau regions(Fig 7.1) – a conventional combined plateau extending up to 130 eV from He atoms and He^{+} ions, determined using TDSE calculations including two active electrons[86, 87], as well as a secondary plateau extending - well beyond the conventional $I_p + 3.17U_p$ cutoff - up to 300 eV, where U_p is the ponderomotive energy and I_p is the ionization of the emitting ion.

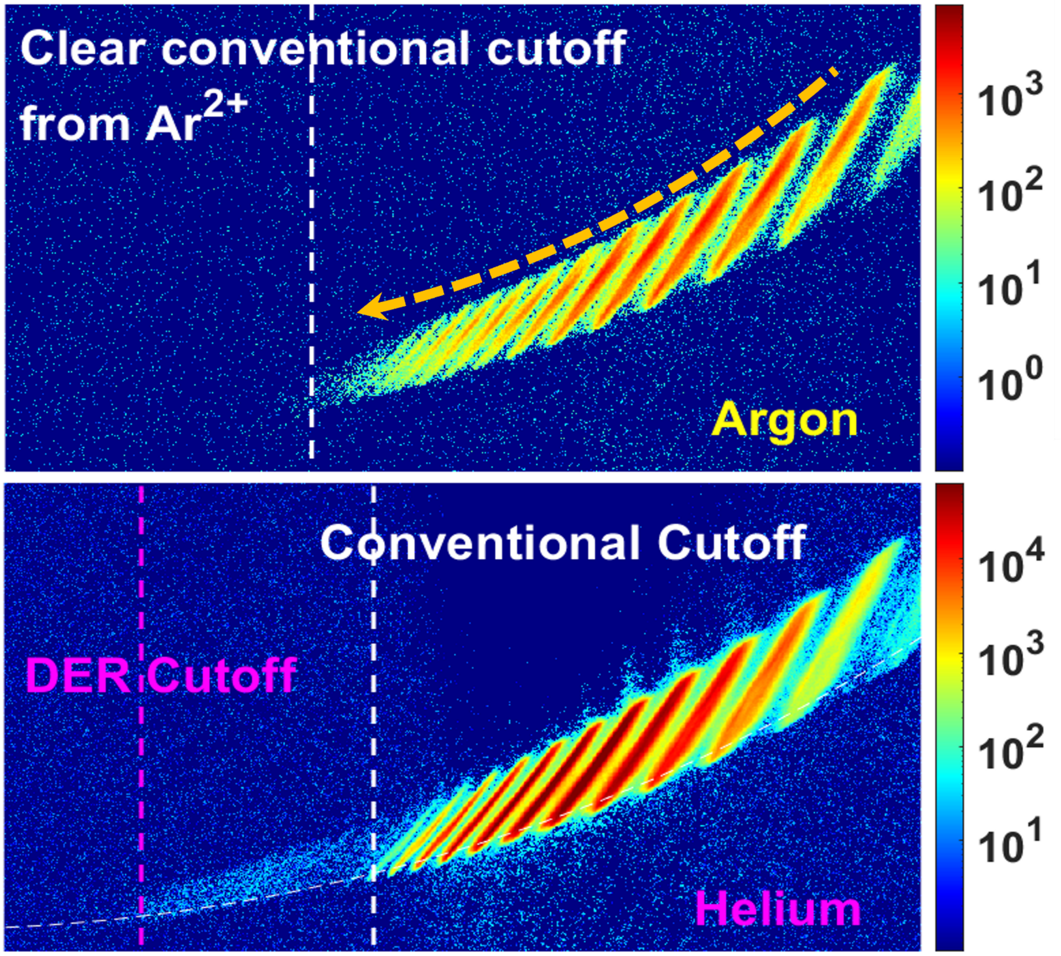

Figure 7.1. Image of a conical pattern of HH spectrum Top: Image from argon gas that shows a clear cutoff. The dashed arrow is the direction of higher harmonic order with higher harmonic photon energy. Bottom: Image from helium with an extended secondary plateau.

7.2 Attosecond Electron Double-Recombination in Helium

Numerical simulations predict that double-electron-recombination (DER) is the physical process with the highest probability to yield a secondary plateau[88, 89]. In this highly-correlated electron system, fractions of the two-electron wavefunctions are ionized at different laser half-cycles and travel along different trajectories, mitigating strong repulsion during local space-time correlation in the presence of the strong UV field, but recombine with the parent ion at the same instant to produce a single X-ray photon. The observed DER plateau in He is more than 4 orders of magnitude weaker.

And to make sure it is a coherent rescattering process we tested with driving laser ellipticity and found the secondary plateau has a characteristic stronger dependence on the ellipticity of the UV driver, due to the longer rescattering time (Fig.7.5). Measurement at different driving laser intensities indicates that the DER cutoffs scale as $5.5U_p$ (Fig.7.2), in agreement with earlier theoretical scaling as $h\nu_{DER} = I_p^{(1)} + I_p(2) + 5.5U_p$ or $I_p^{(1)} + I_p^{(2)} + 4.7U_p$ for ionization of the two electrons separated by a full or a half-laser cycle, in contrast to the single-electron recombination (SER) $h\nu_{SER} = I_p^{(i)} + 3.17U_p$ where $I_p^{(1)}$ =24.4 eV and $I_p^{(2)}$ =54.6 eV are the ionization potentials of helium. The electrons are ionized at different half-laser-cycles such that the Coulomb repulsion is minimized that won't affect each electron's trajectories. Nonsequential electron ionization in the strong field is studied for many years[90] but it won't yield a higher cutoff. However, double electron recombination and one photon emission as a process do require the two electrons to be correlated and able to accumulate more kinetic energy from the combined two-electron system and yield a higher cutoff than a conventional single electron recombination picture. The classical trajectories are in Fig 7.3. The TDSE simulation with correlated electrons with different intensities is shown in Fig 7.7 to 7.9 which shows consistency with the experimental observation.

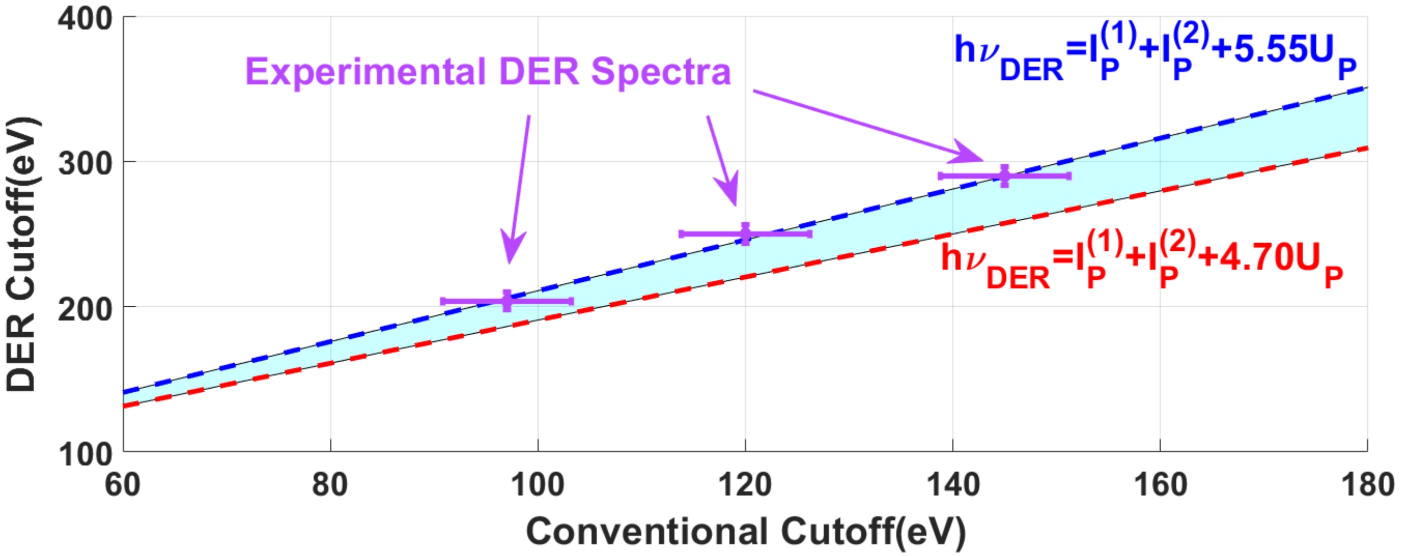

Figure 7.2. Linear relationship with conventional single recombination cutoff and secondary cutoff. Experimental data were consistent with the secondary cutoff predicted by the DER cutoff with the scaling of $5.5U_p$.

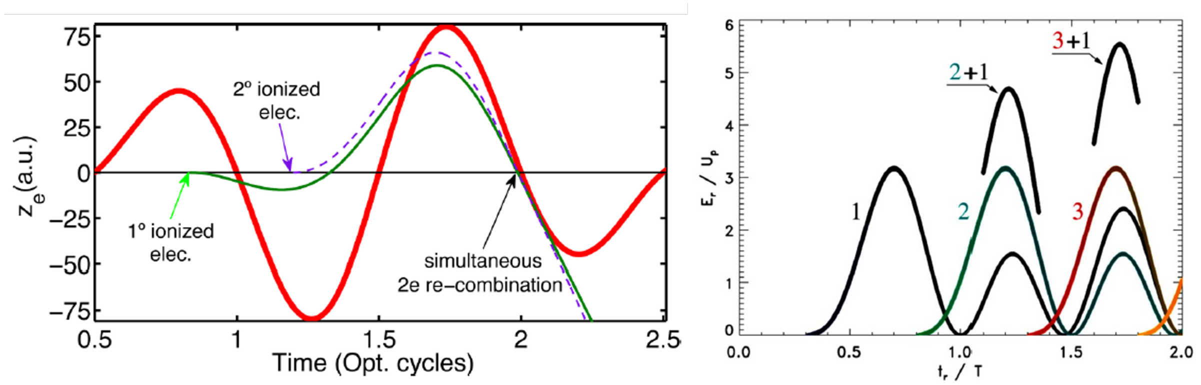

Figure 7.3. Classical trajectory of DER. Left: Classical trajectory of two electrons ionized at different half cycles and recombined at the same time with one photon emission. Right: Possible ponderomotive energy accumulated by recombination of two electrons that ionized at different half-cycle. The black, green, and red lines represent the electron ionized at the first, second, and third half cycles. For an electron ionized around $0.3T$, it reaches its maximum ponderomotive at around $0.7T$ which is the single electron case. If it recombines with an electron ionized at the second or third half cycle, their combined ponderomotive energy can be higher as the graph shows. Graph adapted from[88, 89].

7.3 Attosecond Electron-Electron Correlations in Helium

Finally, theoretically and experimentally, high local electron correlations are essential for DER from the instant of tunnel ionization to recombination. In contrast, in low electron correlation systems with many outermost electrons, the bright, effectively phase-matched signal from Ar, Ar^{+}, and Ar^{2+}, as well as Ne and Ne^{+}, extends to 120-150 eV without observable signatures of a secondary plateau (Fig.7.1). The electron-electron correlation is supposed to be much more preferred in a few-electron system where the bounded electrons are more heavily affected by the ionization of the first electron. In such a way, Helium should be the best candidate to observe such a phenomenon as we observed.

In summary, we demonstrate, for the first time to our knowledge, the second plateau of HH from Helium gas that extends the cutoff from 150 eV to more than 200 eV. These extended harmonics should be, by physics, also coherent but with different physics and temporal properties. Our work paves a way to detect highly correlated femtosecond-to-attosecond electron-electron dynamics in atomic, molecular systems, and quantum materials by using high-harmonic electron-

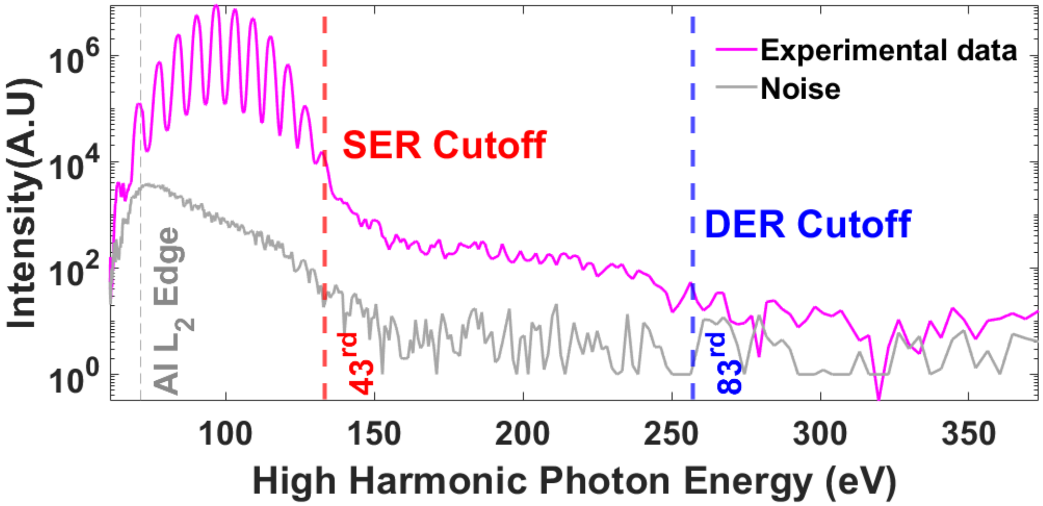

Figure 7.4. HH spectrum with the secondary cutoff from DER. The conventional single electron cutoff is around 120 eV with harmonic order 43, and the secondary cutoff is around 250 eV that close to 81^{st} harmonic.

correlation spectroscopy of interest to fundamental quantum local and non-local correlation studies, and technological importance to quantum computing and superconductivity.

7.4 Outlook

Another good candidate of studying DER is hydrogen which is a molecular system with only two electrons per H atom. Hydrogen, due to the relatively large spatial distance from the two electrons on two H atoms that made the electrical repulsion significantly smaller, is predicted to have an even higher DER cutoff with two electrons that ionize and recombine at the same time. The predicted cutoff from Hydrogen could be $I_P^{(1)} + I_p^{(2)} + 6.35U_p$ for the long pulse limit and $I_p^{(1)} + I_p^{(2)} + 6.16U_p$ for short pulse which around 6-cycle[91] with $I_p^{(1)}$ and $I_p^{(2)}$ are both 13.58 eV. We observe the bright HH signal from hydrogen but with much lower conventional cutoff photon energy. It is as predicted because the ionization potential of Hydrogen is substantially lower compared to helium. Also, the molecular property makes it affected by driving laser polarization effect such that the cutoff is lower than normal atomic gases. However, the secondary cutoff from hydrogen is not observed yet(Fig.7.6). It is also possible that the intensity of the driving

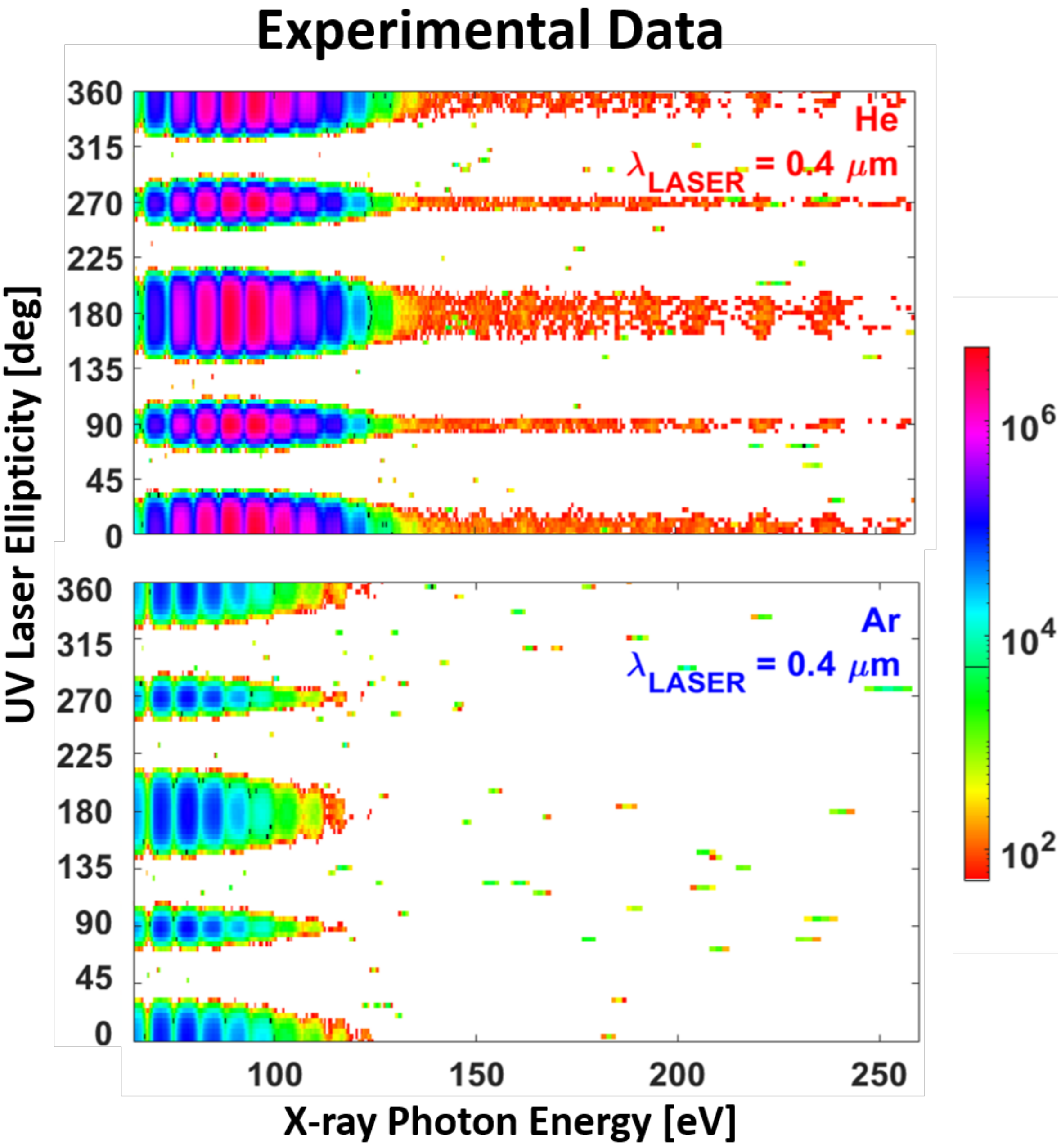

Figure 7.5. Experimental comparison of driving laser ellipticity scan of the driven laser in Helium(top) and Argon(bottom).

laser on hydrogen is way too higher than its barrier suppression threshold which is around 2.74×10^{14}W/cm^2 that it suppresses the HHG by too much. Hydrogen is a candidate worth systematic studying in the lower-intensity regime.

Chapter 7, in full, is currently being prepared for the publication of the material Surprise in Highly Correlated Two-Electron System: Extended Secondary Plateau in X-ray High Harmonic Generation from Helium Due to Double Electron Recombination. Siyang Wang, Jieyu Yan, Alba de las Heras, Sirius Song, Aleksander Prodanov, Zhihan Wu, Carlos Hernández-García, Luis Plaja, Dimitar Popmintchev, and Tenio Popmintchev. The dissertation author was the primary investigator and the author of this paper.

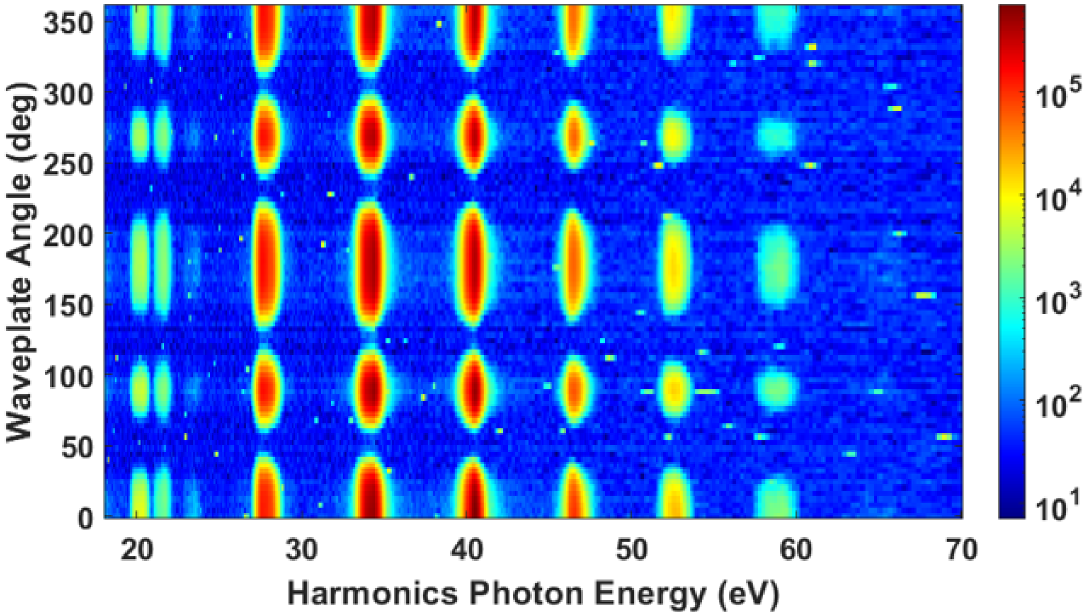

Figure 7.6. Experimental Ellipticity scan of the driven laser in hydrogen. There is no sign of a secondary plateau so far.

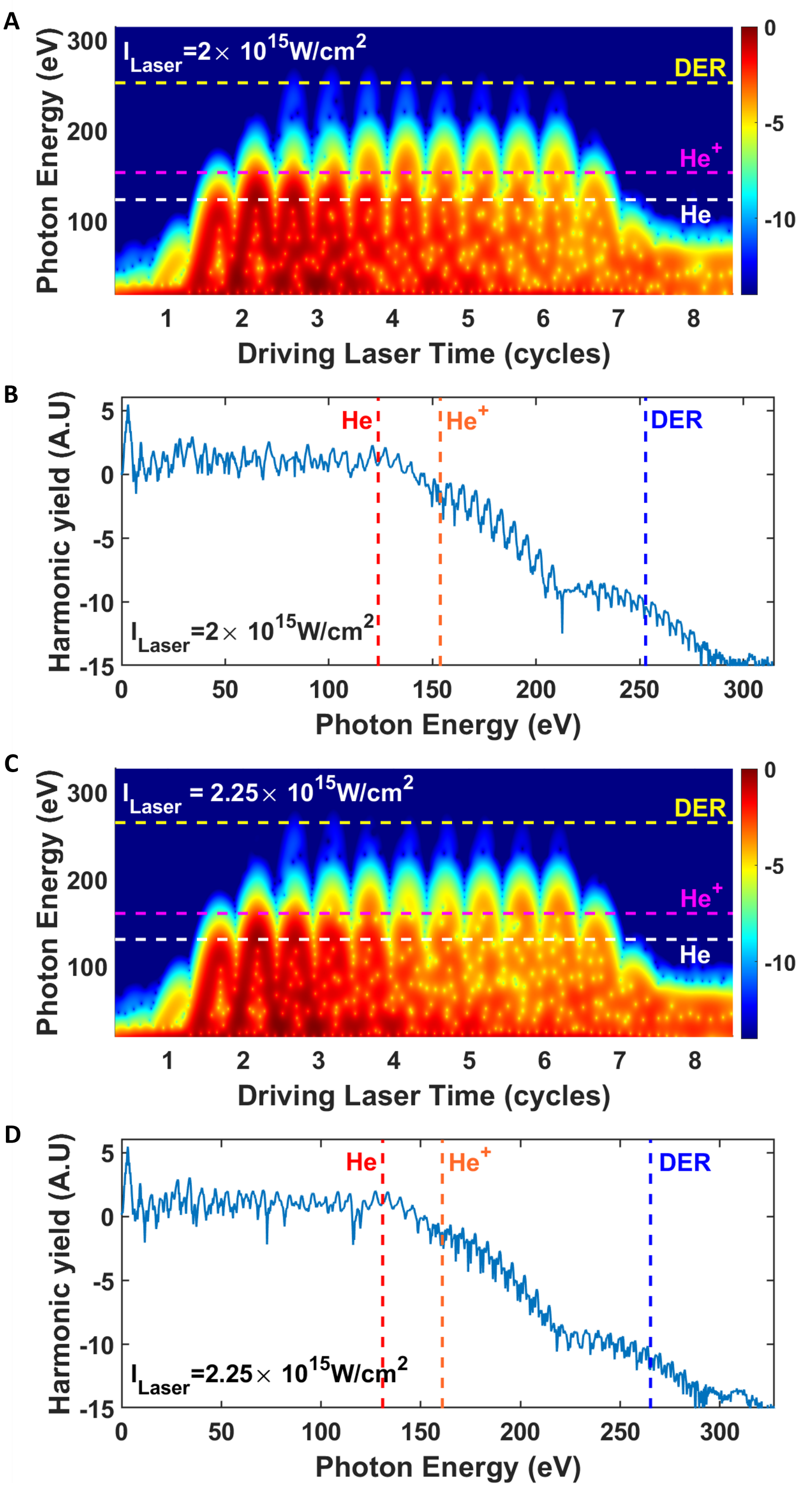

Figure 7.7. TDSE time-frequency analysis and HH spectrum. The horizontal dashed line in A and C and the vertical dashed line in B and D show the cutoff from different ions and DER.(A and B): Laser intensity of $2 \times 10^{15}\mathrm{W/cm^2}$ (C and D): Laser intensity of $2.25 \times 10^{15}\mathrm{W/cm^2}$. Graph from Alda de las Heras from Carlos Hernandez-Garcia group.

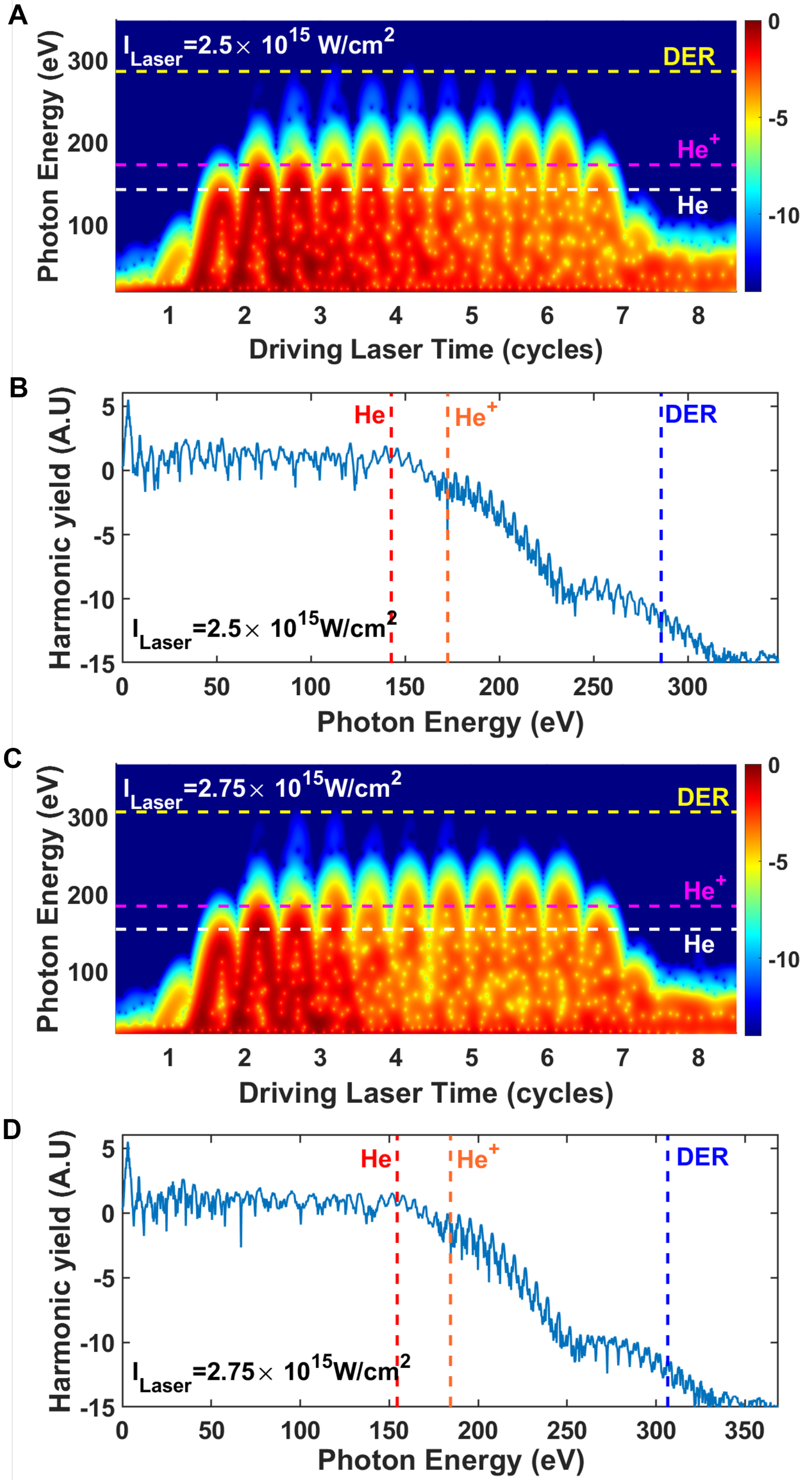

Figure 7.8. TDSE time-frequency analysis and HH spectrum. The horizontal dashed line in A and C and the vertical dashed line in B and D show the cutoff from different ions and DER.(A and B): Laser intensity of 2.5×10^{15}W/cm^2 (C and D): Laser intensity of 2.75×10^{15}W/cm^2. Graph from Alda de las Heras from Carlos Hernandez-Garcia group.

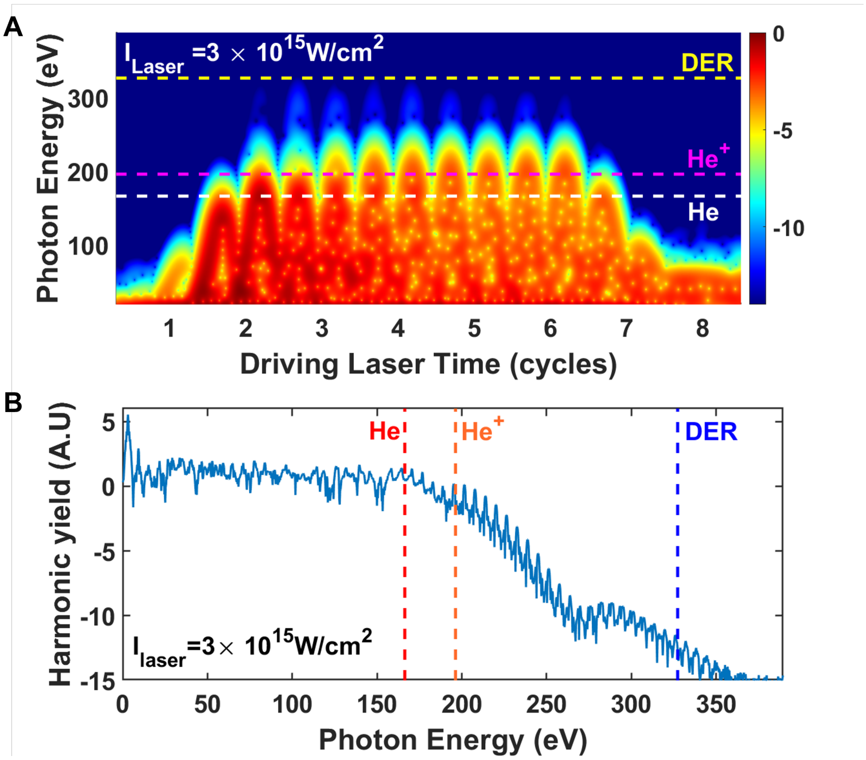

Figure 7.9. Theoretical TDSE time-frequency analysis and HH spectrum. The horizontal dashed line in A and the vertical dashed line in B show the cutoff from different ions and DER.(A and B): Laser intensity of 3×10^{15}W/cm^2. Graph from Alda de las Heras from Carlos Hernandez-Garcia group.

Appendix A

Ionization potential of noble gases

The ionization potential of noble gases and charged ions[92].

Table A.1. Ionization potentials of selected atoms and ions (From NIST).

Ionization potential [eV]						
Element	He	Ne	Ar	Kr	Xe	H_2
Neutral	24.587	21.564	15.760	13.9996	12.1298	13.598
1^{st}	54.417	40.963	27.630	24.360	20.975	
2^{nd}		63.423	40.735	35.838	31.05	
3^{rd}		97.190	59.58	50.85	42.20	
4^{th}		126.247	74.84	64.69	54.1	
5^{th}		157.934	91.290	78.49	66.703	
6^{th}		207.271	124.41	109.13	91.6	
7^{th}		239.1	143.457	125.802	105.978	
8^{th}		1195.8	422.6	233.0	179.84	
9^{th}		1362.2	479.76	268	202.0	
10^{th}			540.4	308	229.02	

Appendix B

Atomic Unit Conversion

Table B.1. Atomic unit in SI unit and its physical significance.

1 AU	in SI units	physical significance
Mass	9.1094×10^{-31}kg	mass of electron
Length	0.5292×10^{-10}m	Bohr radius
Time	2.4189×10^{-17}s	classical electron orbit time with H atom
Charge	1.609×10^{-19}C	electron charge
Intensity	3.5095×10^{16} W/cm^2	appearance intensity for H atom
Velocity	2.1877×10^{6}m/s	c divided by fine structure constant
Permittivity	1.1126×10^{14}C/V·m	Coulomb constant
Energy	27.21eV	2 Ryberg
Magnetic field	2.3505T	magnetic field of H by classical orbiting electron
Action	1.0546×10^{-34}J· s	quantum of angular momentum

In atomic unit:

$$\hbar = e = m_e = 4\pi\varepsilon_0 = 1$$

Appendix C

Conical Grating Efficiency Simulation

The conical diffraction grating has a state of art high efficiency that can be up to nearly 90%. The reflection efficiency of different diffraction orders and the spacing between the efficiency peak of different diffraction orders is a function of the blaze angle of the grating when manufactured and also the incidence angle of the HH beam.

As can be seen from the C-F from figure below that increasing the incidence angle will usually decrease the efficiency of the metal-coated surface. Also, the efficiency peak of different diffraction orders shifts to the lower energy side and with smaller spacing. However, sometimes the bigger incident angle is wanted because it comes with a lower degree of aberration.

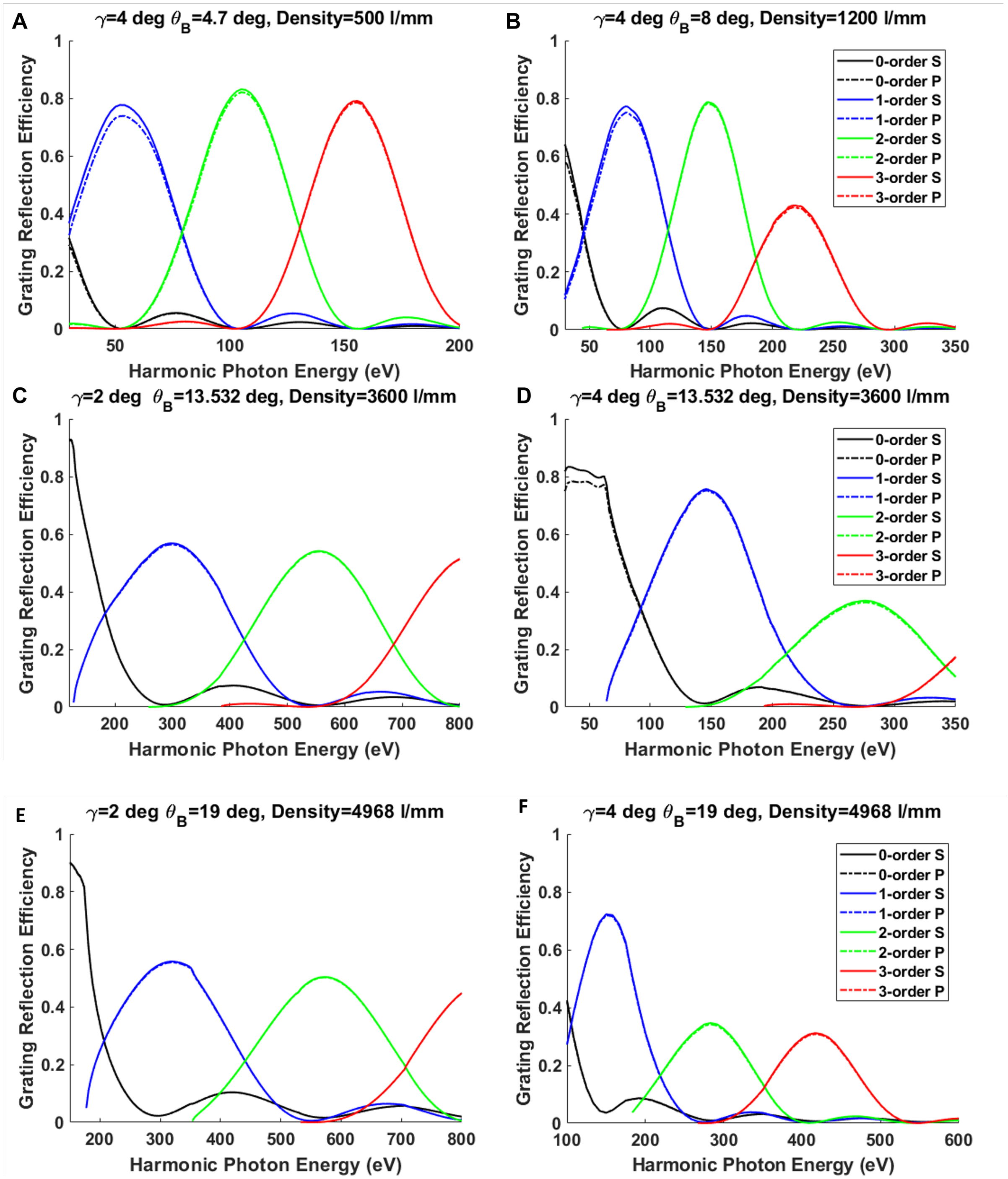

Figure C.1. A) 500 line/mm grating with 4 degrees of incident angle. B) 1200 line/mm grating with 4 degrees of incident angle. C) 3600 line/mm grating with 2 degrees of incident angle. D) 3600 line/mm grating with 4 degrees of incident angle. E) 4968 line/mm grating with 2 degrees of incident angle. F) 4968 line/mm grating with 4 degrees of incident angle.

Bibliography

[1] A. McPherson, G. Gibson, H. Jara, U. Johann, T. S. Luk, I. A. McIntyre, K. Boyer, and C. K. Rhodes. Studies of multiphoton production of vacuum-ultraviolet radiation in the rare gases. *J. Opt. Soc. Am. B*, 4(4):595–601, Apr 1987.

[2] M Ferray, A L'Huillier, X F Li, L A Lompre, G Mainfray, and C Manus. Multiple-harmonic conversion of 1064 nm radiation in rare gases. *Journal of Physics B: Atomic, Molecular and Optical Physics*, 21(3):L31, feb 1988.

[3] P. A. Franken, A. E. Hill, C. W. Peters, and G. Weinreich. Generation of optical harmonics. *Phys. Rev. Lett.*, 7:118–119, Aug 1961.

[4] J. A. Armstrong, N. Bloembergen, J. Ducuing, and P. S. Pershan. Interactions between light waves in a nonlinear dielectric. *Phys. Rev.*, 127:1918–1939, Sep 1962.

[5] X. F. Li, A. L'Huillier, M. Ferray, L. A. Lompré, and G. Mainfray. Multiple-harmonic generation in rare gases at high laser intensity. *Phys. Rev. A*, 39:5751–5761, Jun 1989.

[6] L. V. Keldysh. Ionization in the Field of a Strong Electromagnetic Wave. *J. Exp. Theor. Phys.*, 20(5):1307–1314, 1965.

[7] S L Chin, F Yergeau, and P Lavigne. Tunnel ionisation of xe in an ultra-intense co2 laser field (1014 w cm-2) with multiple charge creation. *Journal of Physics B: Atomic and Molecular Physics*, 18(8):L213, apr 1985.

[8] P. B. Corkum. Plasma perspective on strong field multiphoton ionization. *Phys. Rev. Lett.*, 71:1994–1997, Sep 1993.

[9] Jeffrey L. Krause, Kenneth J. Schafer, and Kenneth C. Kulander. High-order harmonic generation from atoms and ions in the high intensity regime. *Phys. Rev. Lett.*, 68:3535–3538, Jun 1992.

[10] M. Yu. Kuchiev. Atomic antenna. *Soviet Journal of Experimental and Theoretical Physics Letters*, 45:404, April 1987.

[11] T. F. Gallagher. Above-threshold ionization in low-frequency limit. *Phys. Rev. Lett.*, 61:2304–2307, Nov 1988.

[12] M. D. Rosen, P. L. Hagelstein, D. L. Matthews, E. M. Campbell, A. U. Hazi, B. L. Whitten, B. MacGowan, R. E. Turner, R. W. Lee, G. Charatis, Gar. E. Busch, C. L. Shepard, and P. D. Rockett. Exploding-foil technique for achieving a soft x-ray laser. *Phys. Rev. Lett.*, 54:106–109, Jan 1985.

[13] B. J. MacGowan, S. Maxon, P. L. Hagelstein, C. J. Keane, R. A. London, D. L. Matthews, M. D. Rosen, J. H. Scofield, and D. A. Whelan. Demonstration of soft x-ray amplification in nickel-like ions. *Phys. Rev. Lett.*, 59:2157–2160, Nov 1987.

[14] M. Bellini, C. Lyngå, A. Tozzi, M. B. Gaarde, T. W. Hänsch, A. L'Huillier, and C.-G. Wahlström. Temporal coherence of ultrashort high-order harmonic pulses. *Phys. Rev. Lett.*, 81:297–300, Jul 1998.

[15] Hiromichi Niikura, F Légaré, Rachel Nuter, Andre Bandrauk, Misha Ivanov, D Villeneuve, and P Corkum. Sub-laser-cycle electron pulses for probing molecular dynamics. *Nature*, 417:917–22, 07 2002.

[16] Hiromichi Niikura, F Légaré, Rachel Nuter, Misha Ivanov, D Villeneuve, and P Corkum. Probing molecular dynamics with attosecond resolution using correlated wave packet pairs. *Nature*, 421:826–9, 03 2003.

[17] S. Baker, J. S. Robinson, C. A. Haworth, H. Teng, R. A. Smith, C. C. Chirilă, M. Lein, J. W. G. Tisch, and J. P. Marangos. Probing proton dynamics in molecules on an attosecond time scale. *Science*, 312(5772):424–427, 2006.

[18] Eleftherios Goulielmakis, Zhi-Heng Loh, Adrian Wirth, Robin Santra, Nina Rohringer, Vladislav Yakovlev, Sergey Zherebtsov, Thomas Pfeifer, Abdallah Azzeer, Matthias Kling, Stephen Leone, and Ferenc Krausz. Real-time observation of valence electron motion. *Nature*, 466:739–43, 08 2010.

[19] Christian Ott, Andreas Kaldun, Luca Argenti, Philipp Raith, Kristina Meyer, Martin Laux, Yizhu Zhang, Alexander Blättermann, Steffen Hagstotz, Thomas Ding, Robert Heck, Javier Madroñero, Fernando Martín, and Thomas Pfeifer. Reconstruction and control of a time-dependent two-electron wave packet. *Nature*, 516:374–8, 12 2014.

[20] Yuki Kobayashi, Kristina F. Chang, Tao Zeng, Daniel M. Neumark, and Stephen R. Leone. Direct mapping of curve-crossing dynamics in ibr by attosecond transient absorption spectroscopy. *Science*, 365(6448):79–83, 2019.

[21] Romain Géneaux, Christopher J. Kaplan, Lun Yue, Andrew D. Ross, Jens E. Bækhøj, Peter M. Kraus, Hung-Tzu Chang, Alexander Guggenmos, Mi-Ying Huang, Michael Zürch, Kenneth J. Schafer, Daniel M. Neumark, Mette B. Gaarde, and Stephen R. Leone. Attosecond time-domain measurement of core-level-exciton decay in magnesium oxide. *Phys. Rev. Lett.*, 124:207401, May 2020.

[22] Martin Schultze, Krupa Ramasesha, C.D. Pemmaraju, S.A. Sato, D. Whitmore, A. Gandman, James S. Prell, L. J. Borja, D. Prendergast, K. Yabana, Daniel M. Neumark, and

Stephen R. Leone. Attosecond band-gap dynamics in silicon. *Science*, 346(6215):1348–1352, 2014.

[23] Fabian Schläpfer, Matteo Lucchini, Shunsuke Sato, Mikhail Volkov, Lamia Kasmi, Nadja Hartmann, Angel Rubio, L. Gallmann, and U. Keller. Attosecond optical-field-enhanced carrier injection into the gaas conduction band. *Nature Physics*, 14, 06 2018.

[24] Dennis Gardner, Michael Tanksalvala, Elisabeth Shanblatt, Xiaoshi Zhang, Benjamin Galloway, Christina Porter, Robert Karl, Charles Bevis, D. Adams, Henry Kapteyn, Margaret Murnane, and Giulia Mancini. Subwavelength coherent imaging of periodic samples using a 13.5 nm tabletop high-harmonic light source. *Nature Photonics*, 11:259–263, 2017-03 2017.

[25] Janos Kirz, Chris Jacobsen, and Malcolm Howells. Soft x-ray microscopes and their biological applications. *Quarterly Reviews of Biophysics*, 28(1):33–130, 1995.

[26] Jianwei Miao, Tetsuya Ishikawa, Ian K. Robinson, and Margaret M. Murnane. Beyond crystallography: Diffractive imaging using coherent x-ray light sources. *Science*, 348(6234):530–535, 2015.

[27] M. Odstrčil, P. Baksh, H. Kim, S. A. Boden, W. S. Brocklesby, and J. G. Frey. Ultra-broadband ptychography with self-consistent coherence estimation from a high harmonic source. In Annie Klisnick and Carmen S. Menoni, editors, *X-Ray Lasers and Coherent X-Ray Sources: Development and Applications XI*, volume 9589 of *Society of Photo-Optical Instrumentation Engineers (SPIE) Conference Series*, page 958912, September 2015.

[28] Alexey Gorlach, Ofer Neufeld, Nicholas Rivera, Oren Cohen, and Ido Kaminer. The quantum-optical nature of high harmonic generation. *Nature communications*, 11:4598, 09 2020.

[29] Sándor Varró. Quantum optical aspects of high-harmonic generation. *Photonics*, 8(7), 2021.

[30] T D G Walsh, F A Ilkov, J E Decker, and S L Chin. The tunnel ionization of atoms, diatomic and triatomic molecules using intense 10.6 mu m radiation. *Journal of Physics B: Atomic, Molecular and Optical Physics*, 27(16):3767, aug 1994.

[31] A. M. Perelomov, V. S. Popov, and M. V. Terent'ev. Ionization of Atoms in an Alternating Electric Field. *Soviet Journal of Experimental and Theoretical Physics*, 23:924, November 1966.

[32] Maxim V Ammosov, Nikolai B Delone, and Vladimir P Krainov. Tunnel Ionization Of Complex Atoms And Atomic Ions In Electromagnetic Field. 0664:138 – 141, 1986.

[33] Spielmann C., Kan C., Burnett N.H., Brabec T., Geissler M., Scrinzi A., Schnurer M., and Krausz F. Near-kev coherent x-ray generation with sub-10-fs lasers. *IEEE Journal of Selected Topics in Quantum Electronics*, 4(2):249–265, 1998.

[34] M. Lewenstein, Ph. Balcou, M. Yu. Ivanov, Anne L'Huillier, and P. B. Corkum. Theory of high-harmonic generation by low-frequency laser fields. *Phys. Rev. A*, 49:2117–2132, Mar 1994.

[35] W. Becker, A. Lohr, M. Kleber, and M. Lewenstein. A unified theory of high-harmonic generation: Application to polarization properties of the harmonics. *Phys. Rev. A*, 56:645–656, Jul 1997.

[36] J. A. Pérez-Hernández, L. Roso, and L. Plaja. Harmonic generation beyond the strong-field approximation: the physics behind the short-wave-infrared scaling laws. *Opt. Express*, 17(12):9891–9903, Jun 2009.

[37] Jose Pérez-Hernández, Luis Roso, and Luis Plaja. S-matrix theory for the high-order harmonic generation beyond the strong-field approximation. *Laser Physics*, 19:1581–1585, 08 2009.

[38] J. Tate, T. Auguste, H. G. Muller, P. Salières, P. Agostini, and L. F. DiMauro. Scaling of wave-packet dynamics in an intense midinfrared field. *Phys. Rev. Lett.*, 98:013901, Jan 2007.

[39] K. Schiessl, Kenichi Ishikawa, E. Persson, and J. Burgdorfer. Wavelength dependence of high-harmonic generation from ultrashort pulses. *Journal of Modern Optics - J MOD OPTIC*, 55:2617–2630, 09 2008.

[40] M. V. Frolov, N. L. Manakov, and Anthony F. Starace. Wavelength scaling of high-harmonic yield: Threshold phenomena and bound state symmetry dependence. *Phys. Rev. Lett.*, 100:173001, May 2008.

[41] Andy Rundquist, Charles Durfee, Zenghu Chang, Catherine Herne, Sterling Backus, and Margaret Murnane. Phase-matched generation of coherent soft x-rays. *Science (New York, N.Y.)*, 280:1412–5, 06 1998.

[42] Tenio Popmintchev, Ming-Chang Chen, Alon Bahabad, Michael Gerrity, Pavel Sidorenko, Oren Cohen, Ivan Christov, and Margaret Murnane. Phase matching of high harmonic generation in the soft and hard x-ray regions of the spectrum. *Proceedings of the National Academy of Sciences of the United States of America*, 106:10516–21, 07 2009.

[43] Yusuke Tamaki, Jiro Itatani, Yutaka Nagata, Minoru Obara, and Katsumi Midorikawa. Highly efficient, phase-matched high-harmonic generation by a self-guided laser beam. *Phys. Rev. Lett.*, 82:1422–1425, Feb 1999.

[44] Zenghu Chang, Andy Rundquist, Haiwen Wang, Margaret M. Murnane, and Henry C. Kapteyn. Generation of coherent soft x rays at 2.7 nm using high harmonics. *Phys. Rev. Lett.*, 79:2967–2970, Oct 1997.

[45] E. Constant, D. Garzella, P. Breger, E. Mével, Ch. Dorrer, C. Le Blanc, F. Salin, and P. Agostini. Optimizing high harmonic generation in absorbing gases: Model and experiment. *Phys. Rev. Lett.*, 82:1668–1671, Feb 1999.

[46] MultiMedia LLC. The center for x-ray optics(cxro).

[47] E. A. J. Marcatili and R. A. Schmeltzer. Hollow metallic and dielectric waveguides for long distance optical transmission and lasers. *Bell System Technical Journal*, 43(4):1783–1809, 1964.

[48] Oren Cohen, Xiaoshi Zhang, Amy L. Lytle, Tenio Popmintchev, Margaret M. Murnane, and Henry C. Kapteyn. Grating-assisted phase matching in extreme nonlinear optics. *Phys. Rev. Lett.*, 99:053902, Jul 2007.

[49] A Paul, Randy Bartels, R Tobey, H Green, S Weiman, Ivan Christov, M Murnane, Henry Kapteyn, and S Backus. Quasi-phase-matched generation of coherent extreme-ultraviolet light. *Nature*, 421:51–4, 02 2003.

[50] Emily Gibson, Ariel Paul, Nick Wagner, Ra'anan Tobey, David Gaudiosi, Sterling Backus, Ivan Christov, Andy Aquila, Eric Gullikson, David Attwood, and Margaret Murnane. Coherent soft x-ray generation in the water window with quasi-phase matching. *Science (New York, N.Y.)*, 302:95–8, 11 2003.

[51] J. Seres, V. Yakovlev, E. Seres, Christina Streli, P. Wobrauschek, Christian Spielmann, and F. Krausz. Coherent superposition of laser-driven soft-x-ray harmonics from successive sources. *Nature Physics*, 3:878–883, 11 2007.

[52] Xiaoshi Zhang, Amy Lytle, Tenio Popmintchev, Xibin Zhou, Margaret Murnane, and Oren Cohen. Quasi phase matching and quantum path control of high harmonic generation using counterpropagating light. *Nature Physics*, 3:270–275, 02 2007.

[53] Dimitar Popmintchev, Carlos Hernández-García, Franklin Dollar, Christopher Mancuso, Jose A. Pérez-Hernández, Ming-Chang Chen, Amelia Hankla, Xiaohui Gao, Bonggu Shim, Alexander L. Gaeta, Maryam Tarazkar, Dmitri A. Romanov, Robert J. Levis, Jim A. Gaffney, Mark Foord, Stephen B. Libby, Agnieszka Jaron-Becker, Andreas Becker, Luis Plaja, Margaret M. Murnane, Henry C. Kapteyn, and Tenio Popmintchev. Ultraviolet surprise: Efficient soft x-ray high-harmonic generation in multiply ionized plasmas. *Science*, 350(6265):1225–1231, 2015.

[54] Young-Gyun Jeong, Riccardo Piccoli, Denis Ferachou, Vincent Cardin, Michael Chini, Steffen Hädrich, Jens Limpert, Roberto Morandotti, Francois Legare, Bruno Schmidt, and Luca Razzari. Direct compression of 170-fs 50-cycle pulses down to 1.5 cycles with 70% transmission. *Scientific Reports*, 8, 08 2018.

[55] Matthias Zeisberger, Alexander Hartung, and Markus A. Schmidt. Understanding dispersion of revolver-type anti-resonant hollow core fibers. *Fibers*, 6(4), 2018.

[56] Andrey Pryamikov, A. Biriukov, Alexey Kosolapov, Victor Plotnichenko, Sergey Semjonov, and Evgeny Dianov. Demonstration of a waveguide regime for a silica hollow - core microstructured optical fiber with a negative curvature of the core boundary in the spectral region ¿ 3.5 m. *Optics express*, 19:1441–8, 01 2011.

[57] Jun Liu, Yuichiro Kida, Takahiro Teramoto, and Takayoshi Kobayashi. Generation of stable sub-10 fs pulses at 400 nm in a hollow fiber for uv pump-probe experiment. *Opt. Express*, 18(5):4664–4672, Mar 2010.

[58] Gaia Barbiero, Haochuan Wang, Martin Graßl, Sebastian Gröbmeyer, Džiugas Kimbaras, Marcel Neuhaus, Vladimir Pervak, Thomas Nubbemeyer, Hanieh Fattahi, and Matthias F. Kling. Efficient nonlinear compression of a thin-disk oscillator to 8.5fs at 55w average power. *Opt. Lett.*, 46(21):5304–5307, Nov 2021.

[59] Louis Daniault, Zhao Cheng, Jaismeen Kaur, Jean-François Hergott, Fabrice Réau, Olivier Tcherbakoff, Nour Daher, Xavier Délen, Marc Hanna, and Rodrigo Lopez-Martens. Single-stage few-cycle nonlinear compression of millijoule energy ti:sa femtosecond pulses in a multipass cell. *Opt. Lett.*, 46(20):5264–5267, Oct 2021.

[60] Dimitar Popmintchev, Siyang Wang, Xiaoshi Zhang, Ventzislav Stoev, and Tenio Popmintchev. Analytical lah-laguerre optical formalism for perturbative chromatic dispersion. *Opt. Express*, 30(22):40779–40808, Oct 2022.

[61] Ivan Buchvarov, Anton Trifonov, and Torsten Fiebig. Toward an understanding of white-light generation in cubic media—polarization properties across the entire spectral range. *Opt. Lett.*, 32(11):1539–1541, Jun 2007.

[62] Dimitar Popmintchev, Carlos Hernández-García, Bonggu Shim, Ming-Chang Chen, Franklin Dollar, Christopher Mancuso, Jose A. Pérez-Hernández, Xiaohui Gao, Amelia Hankla, Alexander Gaeta, Maryam Tarazkar, Dmitri Romanov, Robert Levis, Agnieszka Jaron-Becker, Andreas Becker, Luis Plaja, Margaret M. Murnane, Henry C. Kapteyn, and Tenio Popmintchev. Bright high order harmonic generation in a multiply ionized plasma up to the water window. In *CLEO: 2014 Postdeadline Paper Digest*, page FTh5A.9. Optica Publishing Group, 2014.

[63] Tenio Popmintchev, Ming-Chang Chen, Oren Cohen, Michael E. Grisham, Jorge J. Rocca, Margaret M. Murnane, and Henry C. Kapteyn. Extended phase matching of high harmonics driven by mid-infrared light. *Opt. Lett.*, 33(18):2128–2130, Sep 2008.

[64] K. Midorikawa, Y. Tamaki, J. Itatani, Y. Nagata, and M. Obara. Phase-matched high-order harmonic generation by guided intense femtosecond pulses. *IEEE Journal of Selected Topics in Quantum Electronics*, 5(6):1475–1485, 1999.

[65] Hermann Uchtmann, Chao He, and Arnold Gillner. High precision and high aspect ratio laser drilling: challenges and solutions. *Proc. SPIE*, 9741:974106–974106–12.

[66] Colin Moorhouse. Advantages of picosecond laser machining for cutting-edge technologies. *Physics Procedia*, 41:381–388, 12 2013.

[67] Eric Audouard, Amelie Letan, Eric Mottay, Mathieu Dijoux, Paul-Etienne Martin, Kevin Gaudfrin, and John Lopez. Ultrafast laser trepanning process and modeling. page M902, 01 2016.

[68] Webster Cash. Echelle spectrographs at grazing incidence. *Appl. Opt.*, 21(4):710–717, Feb 1982.

[69] Kui Li, Dimitar Popmintchev, Ruixuan Li, Guangyin Zhang, Yongjun Ma, Changjun Ke, Yunfeng Ma, Zhinan Zeng, Chenxia Yun, Chenyu Tao, Tenio Popmintchev, Zhongwei Fan, Jie Li, and Xiaoshi Zhang. Globally optimized euv monochromator for ultrafast spectroscopy and coherent diffractive imaging. In *Conference on Lasers and Electro-Optics*, page JW3B.52. Optica Publishing Group, 2022.

[70] Muharrem Bayraktar, Hubertus M.J. Bastiaens, Caspar Bruineman, Boris Vratzov, and Frederik Bijkerk. Broadband transmission grating spectrometer for measuring the emission spectrum of euv sources. *NEVAC blad*, 54(1):14–19, 2016.

[71] A. B. Fedotov, E. E. Serebryannikov, and A. M. Zheltikov. Ionization-induced blueshift of high-peak-power guided-wave ultrashort laser pulses in hollow-core photonic-crystal fibers. *Phys. Rev. A*, 76:053811, Nov 2007.

[72] S. P. Le Blanc and R. Sauerbrey. Spectral, temporal, and spatial characteristics of plasma-induced spectral blue shifting and its application to femtosecond pulse measurement. *J. Opt. Soc. Am. B*, 13(1):72–88, Jan 1996.

[73] Hyun Joon Shin, Dong Gun Lee, Yong Ho Cha, Jung-Hoon Kim, Kyung Han Hong, and Chang Hee Nam. Nonadiabatic blueshift of high-order harmonics from ar and ne atoms in an intense femtosecond laser field. *Phys. Rev. A*, 63:053407, Apr 2001.

[74] P. A. Carpeggiani, G. Coccia, G. Fan, E. Kaksis, A. Pugžlys, A. Baltuška, R. Piccoli, Y.-G. Jeong, A. Rovere, R. Morandotti, L. Razzari, B. E. Schmidt, A. A. Voronin, and A. M. Zheltikov. Extreme raman red shift: ultrafast multimode nonlinear space-time dynamics, pulse compression, and broadly tunable frequency conversion. *Optica*, 7(10):1349–1354, Oct 2020.

[75] Tenio Popmintchev, Ming-Chang Chen, Dimitar Popmintchev, Paul Arpin, Susannah Brown, Skirmantas Ališauskas, Giedrius Andriukaitis, Tadas Balčiunas, Oliver D. Mücke, Audrius Pugzlys, Andrius Baltuška, Bonggu Shim, Samuel E. Schrauth, Alexander Gaeta, Carlos Hernández-García, Luis Plaja, Andreas Becker, Agnieszka Jaron-Becker, Margaret M. Murnane, and Henry C. Kapteyn. Bright coherent ultrahigh harmonics in the kev x-ray regime from mid-infrared femtosecond lasers. *Science*, 336(6086):1287–1291, 2012.

[76] Y. Tamaki, K. Midorikawa, and M. Obara. Phase-matched third-harmonic generation in a gas-filled hollow waveguide. In *Conference Proceedings. LEOS '97. 10th Annual Meeting IEEE Lasers and Electro-Optics Society 1997 Annual Meeting*, volume 2, pages 518–519 vol.2, 1997.

[77] Tenio Popmintchev, Michael E. Grisham, David M. Gaudiosi, Brendan A. Reagan, Oren Cohen, Mark A. Berrill, Margaret M. Murnane, Henry C. Kapteyn, and Jorge J. Rocca. Enhanced high harmonic generation in xe, kr and ar using a capillary discharge. In *Conference on Lasers and Electro-Optics/Quantum Electronics and Laser Science Conference*

and Photonic Applications Systems Technologies, page JFA3. Optica Publishing Group, 2007.

[78] Igor Žutić, Jaroslav Fabian, and S. Das Sarma. Spintronics: Fundamentals and applications. *Rev. Mod. Phys.*, 76:323–410, Apr 2004.

[79] Bosheng Zhang, Dennis Gardner, Matthew Seaberg, Elisabeth Shanblatt, Henry Kapteyn, Margaret Murnane, and Daniel Adams. High contrast 3d imaging of surfaces near the wavelength limit using tabletop euv ptychography. *Ultramicroscopy*, 158:98 – 104, 07 2015.

[80] Daniel E. Adams, Leigh S. Martin, Matthew D. Seaberg, Dennis F. Gardner, Henry C. Kapteyn, and Margaret M. Murnane. A generalization for optimized phase retrieval algorithms. *Opt. Express*, 20(22):24778–24790, Oct 2012.

[81] Dimitar Popmintchev, Benjamin R. Galloway, Ming-Chang Chen, Franklin Dollar, Christopher A. Mancuso, Amelia Hankla, Luis Miaja-Avila, Galen O'Neil, Justin M. Shaw, Guangyu Fan, Skirmantas Ališauskas, Giedrius Andriukaitis, Tadas Balčiunas, Oliver D. Mücke, Audrius Pugzlys, Andrius Baltuška, Henry C. Kapteyn, Tenio Popmintchev, and Margaret M. Murnane. Near- and extended-edge x-ray-absorption fine-structure spectroscopy using ultrafast coherent high-order harmonic supercontinua. *Phys. Rev. Lett.*, 120:093002, Mar 2018.

[82] E. Kaksis, G. Andriukaitis, T. Flöry, A. Pugžlys, and A. Baltuška. 30-mj 200-fs cw-pumped yb:caf2 regenerative amplifier. In *Conference on Lasers and Electro-Optics*, page STh4J.6. Optica Publishing Group, 2016.

[83] Carlos Hernández-García, Tenio Popmintchev, M Murnane, Henry Kapteyn, L Plaja, Andreas Becker, and Agnieszka Jaron-Becker. Group velocity matching in high-order harmonic generation driven by mid-infrared lasers. *New Journal of Physics*, 18:073031, 07 2016.

[84] Alba de las Heras, Carlos Hernández-García, Javier Serrano, Tenio Popmintchev, and Luis Plaja. Attosecond rabi oscillations in bright high harmonic emission in the x-ray regime driven by xuv pulses. In *Frontiers in Optics + Laser Science 2022 (FIO, LS)*, page FTu1C.3. Optica Publishing Group, 2022.

[85] Ali Sadollah, Hassan Sayyaadi, and Anupam Yadav. A dynamic metaheuristic optimization model inspired by biological nervous systems: Neural network algorithm. *Applied Soft Computing*, 71:747–782, 2018.

[86] Alba de las Heras, Carlos Hernández-García, and Luis Plaja. Spectral signature of back reaction in correlated electron dynamics in intense electromagnetic fields. *Phys. Rev. Research*, 2:033047, Jul 2020.

[87] Thomas Hansen, Simon Vendelbo Bylling Jensen, and Lars Bojer Madsen. Correlation effects in high-order harmonic generation from finite systems. *Phys. Rev. A*, 105:053118, May 2022.

[88] P. Koval, F. Wilken, D. Bauer, and C. H. Keitel. Nonsequential double recombination in intense laser fields. *Phys. Rev. Lett.*, 98:043904, Jan 2007.

[89] Alexis Chacón, Marcelo F. Ciappina, and Maciej Lewenstein. Double-electron recombination in high-order-harmonic generation driven by spatially inhomogeneous fields. *Phys. Rev. A*, 94:043407, Oct 2016.

[90] B. Walker, B. Sheehy, L. F. DiMauro, P. Agostini, K. J. Schafer, and K. C. Kulander. Precision measurement of strong field double ionization of helium. *Phys. Rev. Lett.*, 73:1227–1230, Aug 1994.

[91] Kenneth K. Hansen and Lars Bojer Madsen. Same-period emission and recombination in nonsequential double-recombination high-order-harmonic generation. *Phys. Rev. A*, 93:053427, May 2016.

[92] Physical Meas Laboratory. National institute of standard and technology.